Flexible Hybrid Nanostructures for Applications as Ultraviolet Radiation Protection Optical Filters

José Raúl Castro Smirnov

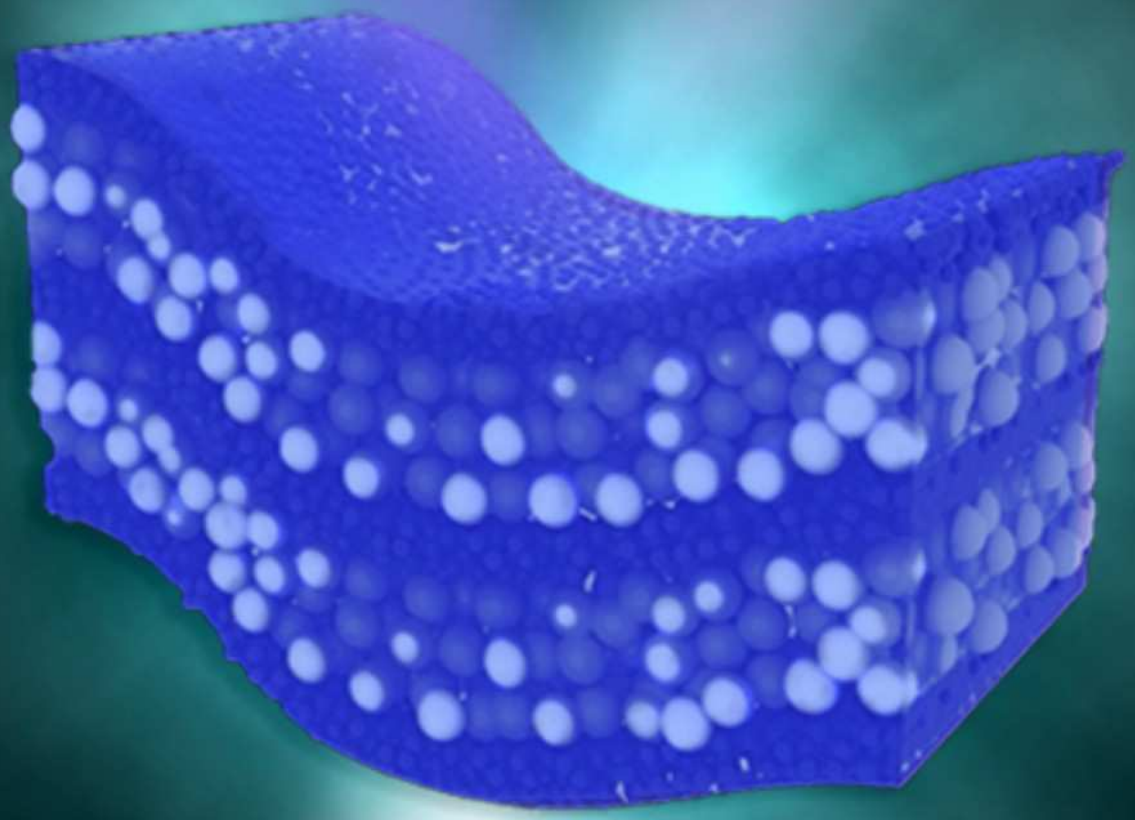

Sevilla, 2014

Flexible Hybrid Nanostructures for Applications as Ultraviolet Radiation Protection Optical Filters

Report presented to apply for PhD degree by:

José Raúl Castro Smirnov

PhD Advisors:

Mauricio Ernesto Calvo Roggiani
Hernán Ruy Míguez García

Department of Physics of Condensed Matter
University of Seville
Institute of Materials Science of Seville
Spanish National Research Council
Seville 2014

Contents

Chapter 1

Flexible visible transparent hybrid films for ultraviolet protection

Introduction

Ultraviolet (UV) radiation is defined as the segment of the electromagnetic spectrum comprised between X-rays and visible light, i.e., between 40 and 400 nm. The UV spectrum is divided into Vacuum UV (40-190 nm), Far UV (190-220 nm), UVC (220-290 nm), UVB (290-320), and UVA (320-400 nm). The escalating applications of ultraviolet light, specifically in the UVA and UVB part of the spectrum, in medicine,[1] cosmetics,[2] or for industrial and commercial purposes in general[3,4] demand deeper studies of the hazards involved in the use of this type of electromagnetic radiation as well as further research in the development of new materials for selectively protecting against it. It is well-known that UV radiation causes damage to organic materials like plastics, woods, or polymers, among others. In general, the formation of free radicals, due to light absorption induced chemical reactions, results in subsequent polymer photodegradation.[5,6]

Common polymers undergo losses in mechanical strength and impact resistance when exposed to UV light.[7] Regarding the effect on human tissue, there is a vast and growing literature regarding the harmful effects of ultraviolet radiation on the skin, as more epidemiologic and basic research continues to illustrate the impact of sun exposure and other sources of UV radiation upon the appearance of cutaneous neoplasm and a variety of photosensitive

dermatoses[8] or skin cancer.[9] In this context, the development of polymer films that act as shields against ultraviolet (UV) radiation constitutes nowadays an active and interesting field of research,[10-15] since they could be used as adaptable coatings for a wide variety of UV sensitive environments.

Different synthetic approaches that are currently being explored to obtain spectrally selective UV protecting flexible films are examined in the light of applications for which versatile materials are needed. Special emphasis is put in those that allow the spectral properties of UV shielding to be tailored-to-measure to target well-defined frequency ranges. Films used for UV blocking can be classified according to the physical mechanism responsible for the protection effect, namely, optical absorption or reflection. This fundamental difference determines that a completely diverse materials design will have to be used to achieve control over spectral selectivity. Compounds or materials whose absorption is employed to eliminate UV wavelengths from the incoming light are either organic molecules or metal oxide nanoparticles. When organic UV absorbing molecules are used, they must be incorporated to polymeric or vitreous matrices, only the former one yielding flexible films. On the other hand, when metal oxide nanoparticles are used, they are hosted by a polymeric matrix and thus hybrid organic-inorganic nanostructures are attained. From a different perspective, when reflection, rather than absorption, of UV wavelengths is sought after, more complex multilayered architectures must be employed, so that interference effects can give rise to the desired blocking effect.[16] In all these approaches, the function of polymers is providing flexibility, toughness, and fracture resistance,[17] as well other significant added values such as bio-compatibility, or chemical or biological functionality.

State of the art of UV radiation protection

In general, the more widely spread approach to UV protection, be it in sunscreen lotions or in any materials whose degradation is to be prevented, is based in the use of organic UV absorbers,[18-20] which transform the incoming radiation in low energy thermal dissipation by means of photophysical reactions. It is out of the reach of this thesis to provide an exhaustive list and detailed description of the compounds currently employed for this purpose, for which we refer the reader to the comprehensive review published by D. Levy et al. on the subject.[21] Suffice it to say here that organic compounds containing phenolic groups with intramolecular hydrogen bonds are among the most widely employed. Examples include xantones, salicylates, benzotriazoles, benzophenones, etc... These organic coatings with intramolecular hydrogen bonds have the advantages of a highly efficient deactivation process,[22] which is radiationless and provides a good mechanism of energy dissipation through excited state intramolecular proton transfer. In brief, the molecules in the first excited state experience an intramolecular

proton transfer to form other tautomeric species, also in its first excited singlet state. This excited proton–transferred species dissipates its energy by a non-radiative decay process in the form of thermal energy.

In general, polymer films containing organic UV absorbers are transparent, colourless and of high optical quality. In order to use them to attain a UV protective film, such compounds must be either applied as a capping onto the UV sensitive material or integrated in an organic or inorganic polymeric matrix (Figure 1). When used as a capping, photostability problems are found. On the other hand, when the UV absorber is mixed with the polymer, some inconvenient may arise after long-lasting exposure because of migration and extraction processes. The first method used to embed the organic molecules in the polymers made use of polymerizable stabilizers.[23] The intramolecular hydrogen bond, which is distinctive for this type of UV absorber, must remain unaltered after the polymerization reaction. Nevertheless, the use of organic polymeric matrices has decreased because of the low stability shown after receiving UV radiation for extended periods of time. Free radicals, generated in the photodecomposition of the organic matrix, can destroy the active form of the stabilizer, reducing the effectiveness of the protective coating. Recently, a solution was proposed to avoid the mentioned handicap by means of using a transparent inorganic matrix to insert the UV absorber, improving the stability of the film and, simultaneously, keeping the highly efficient UV-absorption.[20] The matrix is now an amorphous, highly porous and mechanically stable silica network, prepared by a series of hydrolysis and condensation reactions of silicon alkoxides that occur at low temperature and that can eventually be shaped as a film.

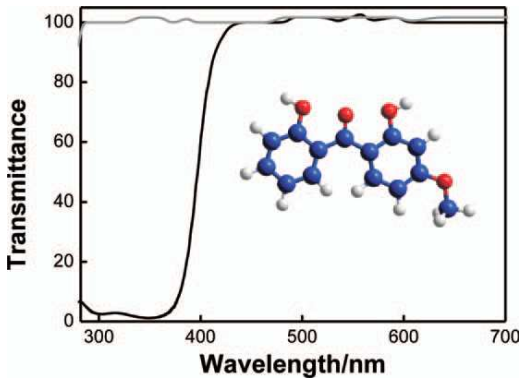

Figure 1: Transmittance spectrum of a sol-gel based UV protecting inorganic film of 1-m width, with (black line) and without (gray line) the UV-absorber molecule (2,2-dihydroxy, 4-methoxybenzophenone) drawn in the inset. (Data extracted from ref. 21).

Although this sol-gel approach solves many of the stability issues observed before and gives rise to matrices capable of incorporating large quantities of organic molecules by adsorption onto the pore walls, it cannot be used to create flexible films. The intrinsic absorption of the sol-

gel based coating caused by inter electronic band gap excitations has also been used to create rigid UV protective coatings.[24]

Hybrid organic-inorganic films

Following the definition given by Kickelbick, a hybrid material is a material that includes two moieties blended on the molecular scale.[25]Within the scope of this thesis, I will consider hybrid materials those formed by a combination of inorganic compounds and organic or partially organic polymers. The use of inorganic materials for UV protection is typically based on optical scattering and/or absorption. The former effect is significant when the wavelength of the incident light is approximately of the same order than the inorganic particle size[26], which gives rise to resonant coupling that can be described, for well-dispersed particles, by Mie scattering theory. Absorption of light results in promotion of electrons from the valence to the conduction band, caused by harvesting of photons with energies above the electronic band gap.

Among a wide spectrum of possibilities to block radiation, metal oxides are preferred due to their good stability. Particularly ZnO and TiO_2 are the most important wide band-gap semiconductors used to protect against UV radiation because of their low cost and toxicity.[2,27] The energy band gaps (E_{gap}) of ZnO and TiO_2 depends on the crystalline phase of the structure. Amorphous TiO_2 and crystalline anatase have an E_{gap} near 340nm and 400nm respectively [28] whereas the E_{gap} of ZnO is near 360nm. Other metal oxide with potential application to block UV protection is CeO_2, but its yellowish coloration diminishes its potential use in visible transparent applications. However, some recent efforts with this metal oxide are made in order to solve this drawback.[29] As we will show later, ZrO_2 is a convenient option if protection is desired at UVC range (lower wavelengths) due to its large band gap value (near 220nm). On the other hand, polymers that are integrated in hybrid UV protecting films in which visible transparency is required must absorb as less light as possible in the visible region and they must allow being processed as flexible slabs. Also, ultraviolet absorption of the polymer should be prevented to avoid photochemical reactions that could lead to a loss of elasticity or to a yellowing of the film. From that point of view, it is better to use polymers whose optical absorption is negligible for $\lambda > 300$ nm.

These requisites limit the range of usable polymers to those that belong to poly(alkyl)siloxane, poly(alkyl)acrylate or polystyrene families. The potential interaction of the components of a hybrid material must also be considered in order to prevent that undesired features arise as a consequence: TiO_2 and ZnO particles embedded into an organic matrix can photo-catalyze the degradation of polymer,[6] in which case the photo-stabilization of the hybrid structure is an additional requirement that must be kept into account. In Figure 2 we represent the different synthetic process that lead to a hybrid self-standing film.

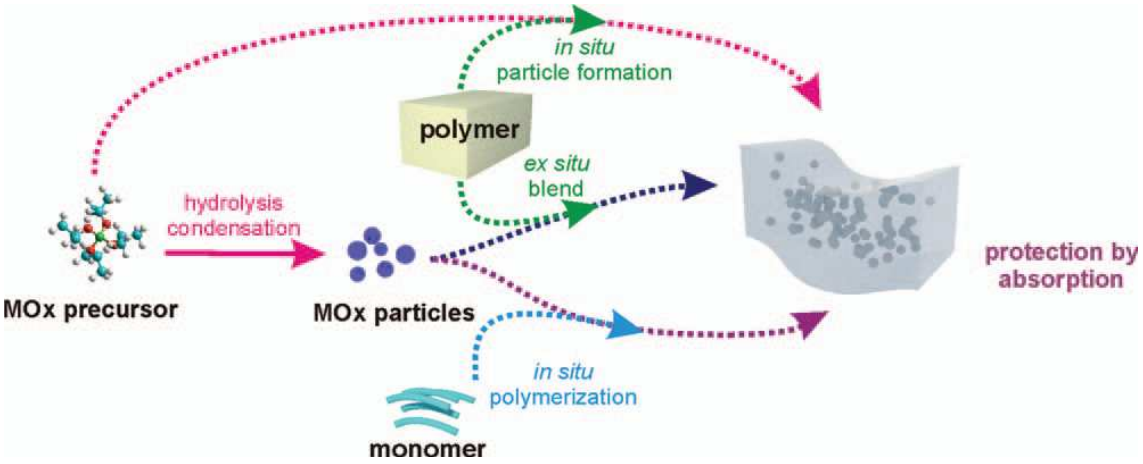

Figure 2: Different synthetic pathways of the synthesis of flexible polymer nanoparticle films based on *in situ* and *ex situ* methods.

Monomers, polymers and metal oxides compounds can be combined by different pathways. Commonly, two synthetic approaches are applied to integrate metal oxide particles in polymers. These strategies are commonly named *in situ*, which is based either on the synthesis of inorganic compounds within the polymer matrix or the polymerization of an organic monomer around the inorganic phase [30,31] and *ex situ*, which consists in the direct incorporation of nanoparticles with polymers by mechanical blend, polymer melt intercalation, or through the use of solvents.[32] Both processes take advantage of the synthesis of polymer-nanoparticle mixes in liquid media. The solution processed materials so obtained are highly reproducible and easy to deposit onto a wide variety of substrates employing low cost techniques (spin coating, dip coating, roller blade, liquid casting, etc...). In general, regardless of the method employed, once the inorganic phase is dispersed in the organic matrix, the mixture inherits the mechanical properties of the polymer, being as a result mouldable with the desired form, as well as foldable and adaptable to a diversity of substrates. So, flexible self-standing films for UV protection can be devised by these approaches. We have to mention here that these two approaches are not exclusive to the synthesis of hybrid nanocomposites to protect against ultraviolet radiation, but also can be used to control the refractive index of the ensemble which has technological importance.[33,34]In what follows, we describe in more detail the *in situ* and *ex situ* approaches to flexible self-standing films.

In situ methods

In situ methods include the processes of synthesis or growth of inorganic particles in a polymer containing media (in situ particle generation, upper arrow pathway in Figure 2) or the polymerization of monomers in presence of metal oxide inorganic particles (*in situ*

polymerization, lower arrow pathway in Figure 2). Thereby, *in situ* methods provide an inherent homogeneity of the structures synthesized, overcoming the problem of agglomeration even at high concentration (20% m/m) of metal oxide particles. However, some requisites must be fulfilled to achieve transparent films.

When nanoparticles are synthesized in a polymer matrix, a careful control of the interaction of the inorganic building blocks with the polymers at molecular level is required. In addition, the particle synthesis media must be compatible with the solvent where the polymer is dissolved to avoid precipitation of the assembly. One of the most widely employed routes to prepare organic-inorganic hybrid materials by *in situ* particle generation is the sol-gel method carried out within a polymeric matrix. The synthesis of metal oxide three-dimensional networks via sol-gel is mainly based on a two-step reaction: hydrolysis and condensation of liquid soluble inorganic precursors. The compatibility of this process with polymerization reactions and with polymers is the key to integrate both systems.[35]

A large amount of literature addressing this point can be found for SiO_2 precursors; however, SiO_2 and their related partially hydrolyzed compounds cannot be use to block light in the UV region due to the large value of their electronic band-gap (> 6.1 eV). The change of SiO_2 for compounds of other transition metal oxides, such as ZnO, TiO_2, ZrO_2, etc…, as mentioned above, involves an increase in the reactivity of the metallic centre, forcing to change the chemistry of the polymer to prevent flocculation or aggregation. The most commonly used strategy lies in modifications of the polymer chain to coordinate the reactive metal species. For example, Liou et al. designed and synthesized a polyimide from their monomers[11,36] to include functional groups that can coordinate oxidized species of titanium. These titanium oxo-species were originated by the hydrolysis of titanium butoxide. Depending on the ratio of the starting reactive species, final polyimide films can contain between 5 and 70% wt. of TiO_2 maintaining flexibility. Scandola et al. synthesized and characterized polymer-titania hybrids in an organic phase constituted by polycarbonate[37] or polyesters such as poly(-caprolactone) and poly(D,L-lactic acid).[13,38] Mono- and bi- dentate complexes can be formed between titanium oxo groups and carboxylic acid groups of lactate providing additional stability to the final material.

This approach was also integrated in fabrics by fibre coating to build textiles with UV protection. In other interesting approach, Ogawa et al.[39] prepared hybrid films of TiO_2 by co-hydrolysis and co-condensation of a titanium alcoxide in polyalkyl siloxane previously functionalized with methoxy groups. The functionalized starting oligomer is important to avoid particle segregation and to ensure good homogeneity in the final transparent product. Mechanical (principally elastomeric) characteristics of polydimethylsiloxane (PDMS) make this hybrid material a good candidate to block light in different configurations. In addition, PDMS is fully biocompatible and environmentally friendly. It is also chemically inert, thermally stable, permeable to gases, simple to handle and manipulate, and exhibits isotropic and homogeneous

properties.[40] On the other hand, when monomers polymerize in the presence of previously synthesized metal oxide nanoparticles, is the surface functionalization of the latter what plays the main role in the integration with the polymerizing media. Primary thiols and amines can be used for chemical functionalization of the particles, acting as phase transfer and hydrophobization agents. The so obtained nanocomposites are normally formed with acceptable separation, homogenous distribution, and strong bonds.

When polymerization is carried out with untreated nanoparticles, aggregates can show up, thus provoking a loss of transparency in the resulting polymeric phase, and hence in the hybrid film, owing to scattering of light. This kind of *in situ* process was used to integrate ZnO nanoparticles in a polymer matrix in a pioneering work of Wegner et al.[41] These nanocomposite films were obtained polymerizing methyl methacrylate in presence of ZnO nanoparticles previously synthesized. Particles were functionalized with an alkyl-phosphonic acid to make them compatible with the polymerizing media. The resulting films block UV light for $\lambda < 350$nm maintaining transparency in the visible.[10] In a different approach, epoxy resins were used to host ZnO particles prior to the curing of the former.[42] After that, the initiators were added and the mixture was subjected to a thermal treatment to polymerize the particle containing resin. ZrO_2 nanoparticles can be integrated in flexible films of polyacrylate using a similar approach.[43] Since ZrO_2 energy band-gap is higher than 5.0 eV, this metal oxide hybrid films can be useful to protect against high energy UV radiation ($\lambda < 250$nm), maintaining transparency at higher UV wavelengths. ZrO_2 metal oxide particles have to be functionalized previously to make them compatible with the acrylate monomer solution or with the polymerization media. The polymerization of the composite starts after the addition of the chemical initiator combined in this case with ultraviolet irradiation.

The disadvantages of *in situ* method are related to the fact that unreacted substances may stay trapped in the final hybrid material, affecting of its optical and mechanical features and endangering its stability. Besides, the reaction phase and solution viscosity cannot be accurately controlled all the way through the sol–gel process. On the other hand, the coexistence of particle synthesis by sol-gel with polymers or vice versa restricts the applicability of this method to a limited number of systems.

Ex situ methods

Other successful approach to the preparation of flexible, visibly transparent, self-standing UV protective films is based on the combination of pre-synthesized nanoparticles with bulk polymers. This approach resembles that widely employed in sunscreen lotions, which typically incorporates ZnO or TiO_2 particles. *Ex-situ* synthesis (Figure 2, middle arrow pathway) can be described as a physical mixing of the inorganic and organic components, allowing direct incorporation of the inorganic nanoparticles in the polymeric matrix by means of a standard

solvent. Such nanoparticles are prepared individually, isolated, and purified. Afterwards, they are dispersed into the solution or bulk polymer to form the composites by simple blending. This method presents large flexibility and versatility from the point of view of the large number of organic and inorganic constituents that can be arranged with defined functionalities, improving their relevant characteristics for UV protection and mechanical stability before their integration.

This approach offers the possibility of having synthetic control over the particle size distribution and its surface properties. It also provides control over the concentration, reaction stages, and solution viscosity. All these features make, in general, *ex situ* synthesis more appropriate for industrial purposes. Unlike the i*n situ* method, in *ex situ* pathways the encounter between inorganic and polymer phases is direct, therefore the only requirement to control this process being an appropriate and exhaustive mixing of the two moieties. In general, when *ex-situ* methods are employed, one of the main tasks is the development of new functionalization pathways that make both systems compatible. It is important to remark that the degree of functionalization must be controlled to prevent alteration or degradation of the optical properties of the system. Simple blending of inorganic nanoparticles with a polymer often leads to lack of homogeneity and low transparency materials resulting from agglomeration and phase separation.

There are some synthetic approaches to prevent this situation. For example, the work of Seetapan & Panyathammaporn includes TiO_2 particles in a silicone elastomer base with curing agent by compression at 140ºC in order to obtain films of 0.8 mm of thickness with less than 4% of transmittance at 320nm.[44]ZnO particles were also integrated within different polymer matrixes. Gao et al., for instance, modified the surface of ZnO nanoparticles with octylamine or oleic acid.[12] These treatments made the surface of the particles more hydrophobic, allowing their dissolution in the same media that polystyrene is dissolved and thus allowing them to be mixed. For instance, Ge et al.[45] combined ZnO particles with a diblock PS-PMMA copolymer to achieve films with particle contents up to 20% with a strong blocking of UV from 350nm. The use of this copolymer is justified by its improved mechanical and thermal properties with respect to pure PMMA or PS films.

Commercial UV protecting products based on hybrid films prepared by *ex situ* methods found direct application in diverse fields. C*roda* International, the UK-based specialty chemical company, developed nanoparticle dispersions in designed polymers (Atmer®) to attain high quality UV protective coatings (Solasorb^{TM}). These films can reach particle concentrations as high as 50% wt. Narrow particle size distribution and lack of aggregates lead to films with a minimum loss of clarity and a high degree of protection over a broad UV frequency range.[46]

Variations of the *ex-situ* approach: polymer infiltration of pre-stacked films

In our group a new methodology was recently developed in order to obtain highly effective UV shielding films that preserve full transparency in the visible range[47] It is based on the deposition of a porous film whose void lattice is later infiltrated with a polymer. [48] In Figure 3, I represent this variation approach (upper arrow pathway). The advantage of this method is the versatility to make flexible films almost independently of the nature of the metal oxide nanoparticle used. The film becomes thinner, nevertheless, until the solvent has evaporated exhaustively and a solid film of the suspended material is deposited. In a spin coating standard course, at the beginning a solution is deposited on the substratewe represent this variation approach.

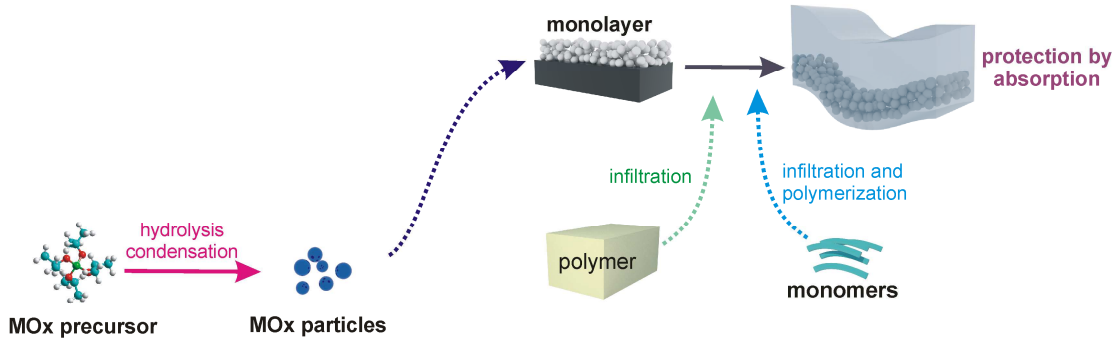

Figure 3: Synthetic pathways of the synthesis of flexible polymer nanoparticle monolayer films based on preformed porous layer method.

It has been mentioned above that traditional *ex situ* as *in situ* methods depend on the control of the surface and the functionalization of the metal oxide particles in order to prevent their aggregation as much as to control the chemistry of the particles, so they are made compatible either with the polymer or the polymerization process. The pre-stacking of a nanoparticle-based film overcomes the obstacles imposed by the particle stabilization and surface functionalization steps. The only requirements for the inorganic films are now the control over particle size in the range of the tens of nanometers, so diffuse scattering in the visible is prevented, and over pore interconnection. This last requisite arises from the need to attain mass continuity of the infiltrated polymer to ensure the mechanical stability of the final ensemble, which must eventually be lifted off the flat substrate onto which the full film preparation occurs. The cut-off UV wavelengths are determined by the electronic gap of the metal oxide nanoparticles.

In our case, among all available compositions, TiO_2, ZnO, SiO_2, and SnO_2 were selected to attain different cut-off frequencies. Once uniform nanoparticle films are deposited, the polymer chosen, PDMS in our case, was embedded by infiltration of its olygomers and subsequent thermally assisted polymerization in the interstitial voids. Then, the structure is cooled down to the PDMS glass transition temperature (approximately 150K), which eases the process of

removal from the substrate. Once it has been lifted off and warmed up to room temperature, the self standing samples present high flexibility and transparency. In Figure 4a we present Field Emission Scanning Electron Microscopy (FESEM) images of the cross section of a self standing hybrid film. In this example we show a film made by a 500 nm thick TiO_2 nanoparticle layer infiltrated with PDMS.

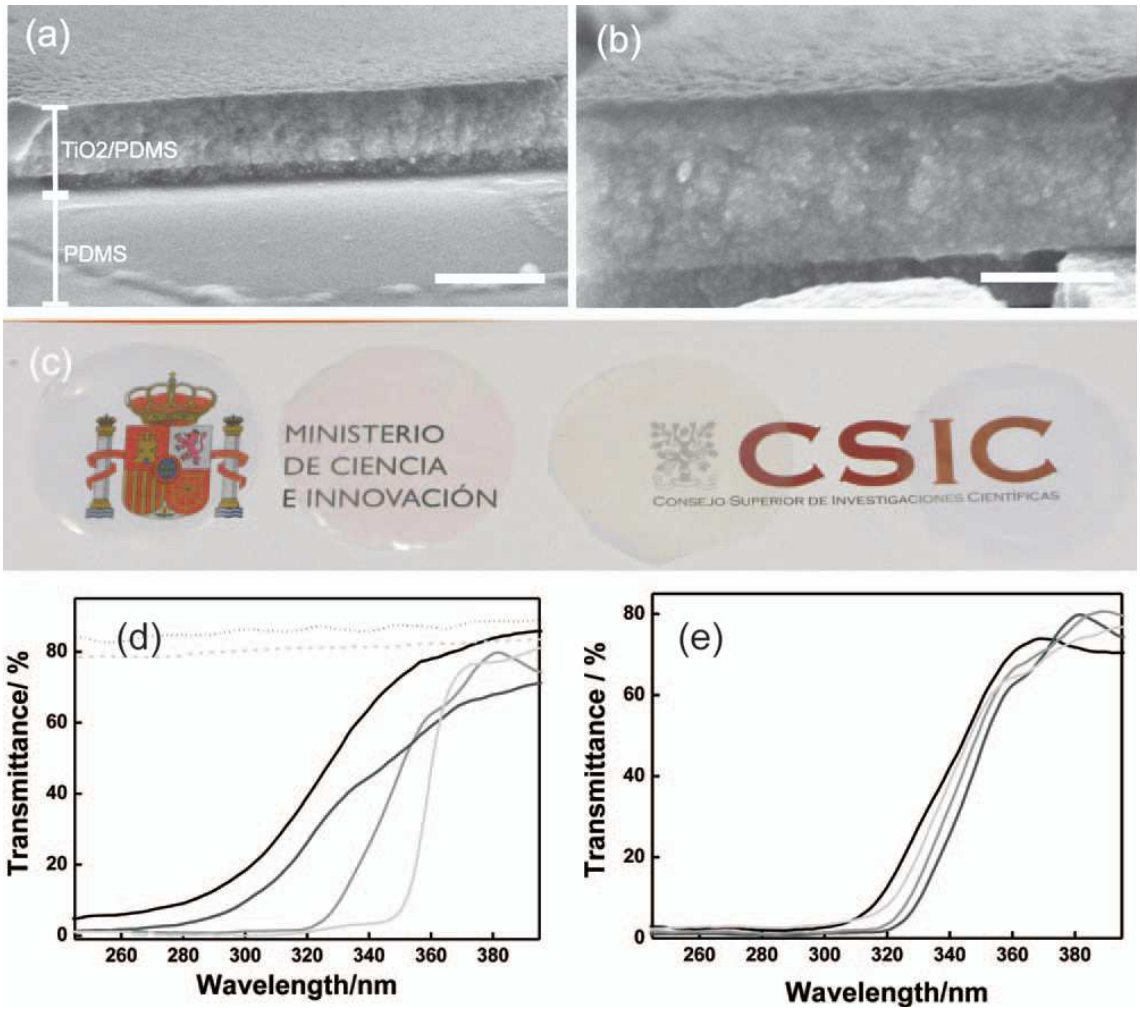

Figure 4: (a) Cross section SEM image of a flexible hybrid TiO_2-PDMS film; (b) Detail of the TiO_2 embedded layer; (c) Image of different flexible films obtained from pre-stacking layers of nanoparticles. Films are made with particles of (from left to right) TiO_2, SiO_2, ZnO, and SnO_2; (d) Total transmittance spectra obtained using different MOx-np layers: SiO_2 on top of a layer of TiO_2 (black line), SnO_2 (dark gray line), TiO_2 (gray line), ZnO (light gray line), pure SiO_2 (short dash), bare PDMS (short dot); and (e) Total transmittance spectra obtained using TiO_2 layers with different thickness (in nm): 300 (black), 430 (dark gray), 560 (gray), and 700 (light gray).

The images reveal uniformity in layer thickness and in composition with no agglomerations or inhomogeneities. No diffuse scattering was detected by optical reflectance or transmittance, while fluctuations of light intensity characteristic of think film interference phenomena were

observed. This reveals that high optical quality films can be attained by this method. These facts put in evidence that neither the thermal treatments nor the presence of PDMS affect the mechanical stability of the previously deposited MOx film, since the appearance of cracks would have resulted in diffuse scattering. Continuity and connectivity of the pore structure favors high filling fractions of PDMS, as it can be observed in the FESEM images. A homogeneous over-layer of PDMS deposited on top can also be seen in Figure 6b. Its thickness is typically on the order of hundreds of microns and endows the film with larger mechanical stability, which facilitates its handling. It is important to mention that these flexible protective films have two different surfaces exposed to the medium, one of pure PDMS and the other made of a mixture of PDMS and the metal oxide colloids. This could allow tailoring the surface chemistry of the film, which may be important in order to design a multifunctional film or in the selective derivatization of each surface.[49]

Figure 4c shows an image of four selective UV shielding films obtained through PDMS infiltration of (from left to right) SiO_2, SnO_2, TiO_2 and ZnO nanoparticle films. The transparency observed in all of them is consequence of the nanometer size of the particles (between 5nm and 30 nm) used to build the MOx layer and the absence of aggregates. Besides, the replacement of the air, present in the mesopores of the starting porous metal oxide layers, by PDMS (refractive index n=1.43) diminishes the dielectric contrast between the inorganic particles and the surrounding medium, improving even further the transparency of the hybrid film. The pale coloration observed in some of the protective films is due to the above mentioned phenomenon of interference of light beams reflected at the top and bottom surfaces of the thin hybrid film.

In figure 4d we show the total transmittance (scattered and ballistic) spectra of some of the flexible UV protective films made using the procedure herein described. Figure 4d shows the spectra attained from self-standing films built using different types of MOx-np, namely a layer of SiO_2-np deposited onto a layer of TiO_2–np (black line), SnO_2-np (dark grey), TiO_2-np (grey), ZnO-np (light grey). The transmittance of pure SiO_2-np (short dash) and bare PDMS (short dot) are also shown. Variations in the wavelength cut-off measured for each film is due to the different values of the energy inter-band transitions of the MOx-np used. This method yields tuning of the cut-off wavelength from 280 nm to 360 nm, covering the entire UVB (280nm-315nm) spectrum, as well as part of the UVA (315 nm-400 nm). In addition, we can also vary the amount of transmitted radiation by means of the thickness of the MOx nanoparticle layers.

This is demonstrated in Figure 4d where the spectral position of the cut-off wavelength is shifted to the visible region as the thickness of TiO_2 increases (similar effect is obtained with SnO_2 and ZnO layers). In this case the wavelength below which transmittance is less than 5% can be tuned along approximately 20 nm in the UVB region of the spectrum. This method opens the possibility of stacking different types of nanoparticle films to attain either the desired

spectral response or a synergic combination of the properties of each layer. In fact, this idea can be extended to build UV protective films based on interference phenomena, which gives rise to an even more precise control of the shielding properties, as shown in what follows.

Blocking by interference

It is well known that radiation of arbitrary wavelength can be blocked by means of the use of the so called interference filters, dielectric mirrors, distributed feedback mirrors or Bragg stacks. These kinds of mirrors are prepared by alternating layers of different refractive index.[50] They have recently become more popular as one dimensional photonic crystals (1DPC), following a more strict classification of periodic optical lattices.[51]

The term of Photonic Crystal has its origin in two articles by Yablonovitch[52] and Sajeev John[53] published roughly at the same time in 1987, although PCs have been studied since the late 19th century. The concept was confirmed in 1990 by K.M Ho et al[54]. The fundamental idea is based in the design of materials that can modify the properties of photons in almost the same approach that common semiconductors affect the properties of electrons. Photonic crystals are structures whose refractive index varies periodically in one or more spatial directions. They were based on electronic materials. In single crystal solids, the periodic arrangement of atoms and molecules introduced a periodic potential for electrons through the crystal. In particular, the network can introduce a forbidden energy gap so that the electrons are not allowed to propagate with certain energies and directions.

Comparable to the periodic potential of electrons in semiconductors, the alternated variation of the dielectric constant influences the electromagnetic properties. As a consequence the transmission of light is prohibited for certain directions and wavelengths, usually called photonic bandgaps. The photonic band gap is likely to be the true optical analogue of the fundamental band-gap of a semiconductor.

Several parameters characterize a photonic crystal:

- Dimensionality

A photonic crystal may be periodic in one, two or three dimensions as shown by the examples of Figure 5. Based in this, they can be called 1D, 2D or 3D photonic crystals.

- Topology

The architecture and the compactness rate of a PC is part of the topology. For a given system, the elementary bricks can be in contact, interpenetrating or isolated.

- The lattice parameter

This is the distance that separated two elementary bricks of a PC.

- Effective refractive index

The effective refractive index of a photonic crystal can be calculated according to Eq. 1:

Eq. 1 $$n_{eff}^2 = n_1^2 f_1 + n_2^2 f_2$$

were n_1 , f_1 , n_2 and f_2 are the refractive indexes and volume fractions of the two different layers.

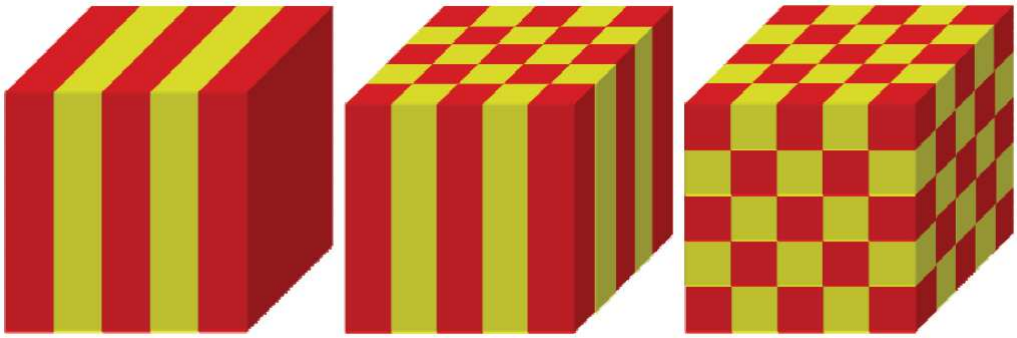

Figure 5: Schematic representations of 1D, 2D and 3D photonic crystals.

One dimensional photonic crystals

Lord Rayleigh was the first to show the existence of photonic bandgaps in one dimensional periodic structures.[55] This was achieved in 1887, a century before the discovery of photonic crystals. It is the simplest photonic crystal structure, in which the dielectric constant is periodic in one dimension of space. 1DPCs display a strong multilayer interference, which caused by the alternating layers of high and low refractive index materials with smooth interfaces between each pair of layers. Up to date, numerous types of materials have been used to build 1DPCs which show excellent optical properties and tunable structural color. 1DPCs made up of inorganic materials are stable and their optical properties can be tuned by filling the interspace with gases or solvents.The applications of the dielectric multilayer structures are widespread (e.g. as stop-band filters[56], high-reflection mirrors[57], antireflection coatings[58], cavities for distributed feedback lasers[59], etc.).

The spectral position of the Bragg peak of 1DPCs can be calculated by using the following formulas:

Eq. 2 $$m\lambda_{Bragg} = 2D\sqrt{n_{eff}^2 - \sin^2\theta}$$

where m is the diffraction order, D is the unit cell, λ_{Bragg} is the spectral position of the Bragg peak, θ is the incident angle and n_{eff} is the effective refractive index, which can be also calculated according to Eq. 3:

Eq. 3 $$n_{eff} = \frac{n_1 d_1 + n_2 d_2}{d_1 + d_2}$$

where, $$D = d_1 + d_2$$

In these formulas, d_1 and d_2 are the thicknesses of the layers with refractive indexes n_1 and n_2 respectively. The stop-band width position W can be determined with the following equation:

Eq. 4 $$W = \frac{4}{\pi} \lambda_{Bragg} \left| \frac{n_2 - n_1}{n_2 + n_1} \right|$$

From the given expressions, we can say that the optical properties of 1DPCs can be tuned by varying the incident angle, the unit cell, and the refractive index. In harmony with the Bragg equation for 1DPCs in Eq 2, the precise spectral localization of the fundamental Bragg peaks can be tuned by varying the optical thicknesses of the 1DPC constituting layers. Dense layers of two visible transparent metal oxides, namely SiO_2 and TiO_2, are some of the most used compounds to prepare rigid Bragg mirrors since they present very different dielectric constant (n_{SiO2}=1.45; n_{TiO2}=2.44). However, dense layers of these two materials do not allow to further process these multilayers to prepare flexible interference filters.

On the other side, all-polymeric based 1DPC stands as a solution to this inconvenience, but they are not appropriate to be used for broad band radiation shielding due to the low contrast between layers, which results in narrow spectral blocking. In addition, and because of the same reason, the stacking of 50-100 layers is required to achieve high reflectance values.[60,61] A few years ago, a new kind of porous 1DPC made of metal oxide nanoparticles as building blocks were developed by our group,[62] but rapidly spread as their applications in different fields were explored.

Porosity offers a new multifunctional dimension in the field of photonic crystals that capitalized in new applications from diverse fields such as sensing, lasing and photovoltaics.[63-66] TiO_2 and SiO_2 nanoparticles are today widely employed to obtain a porous 1DPC by spin or dip coating from size distribution controlled colloidal suspensions. The pore connection between layers is a distinguished feature in these structures to make them suitable to be infiltrated with different kinds of compounds: semiconductors, liquids, vapors, dyes, etc. Our group proved that these optical structures can be infiltrated with polymers to obtain a hybrid 1DPC that can be lifted off from the substrate. The first example was based on the infiltration of poly(bisphenol-A-Carbonate) (commonly named polycarbonate).[48] All the process was made by liquid processing by spin coating, because porous multilayer were infiltrated with a methylene chloride solution

of polycarbonate. This new hybrid material has the optical properties of the inorganic backbone and the mechanical properties of the polymer infiltrated. The possibility to lift-off the photonic crystal from the substrate put in evidence the pore connectivity all throughout the structure. The scheme of this process is shown in Figure 6.

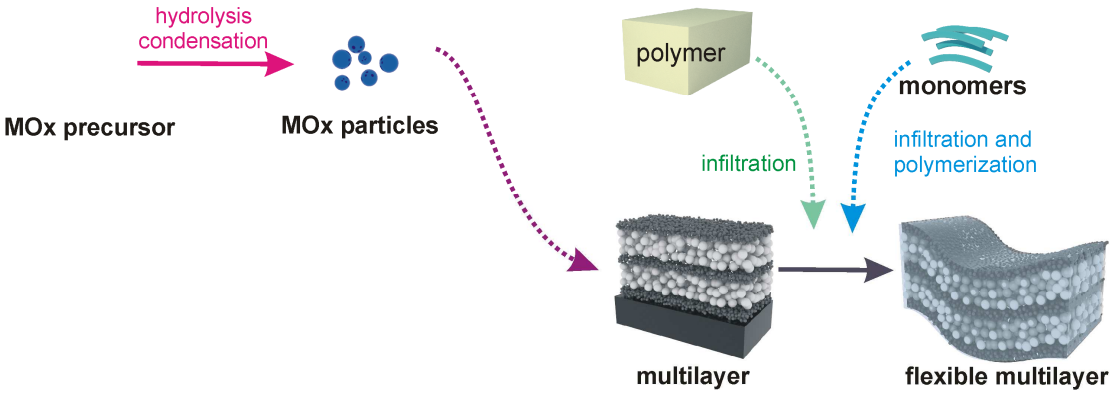

Figure 6: Synthetic pathways of the synthesis of flexible polymer nanoparticle multilayer films based on preformed porous layer method.

In another example, we demonstrated that polymerization can be done within the pores of the structure.[16,67] Just like it is done for the case of layers made of a single type of particle, a porous photonic crystal is infiltrated with PDMS that after thermal treatment it converts to a flexible 1DPC. It is worth mentioning that 20 layers are enough to block 99% of the incident light at any desired spectral position comprised in the visible region. Some pictures of this kind of blocking system are shown in Figure 7a and 7b. Flexibility and bright colours result from the mechanical properties of the PDMS and the optical properties of the embedded nanoparticle photonic crystals respectively.

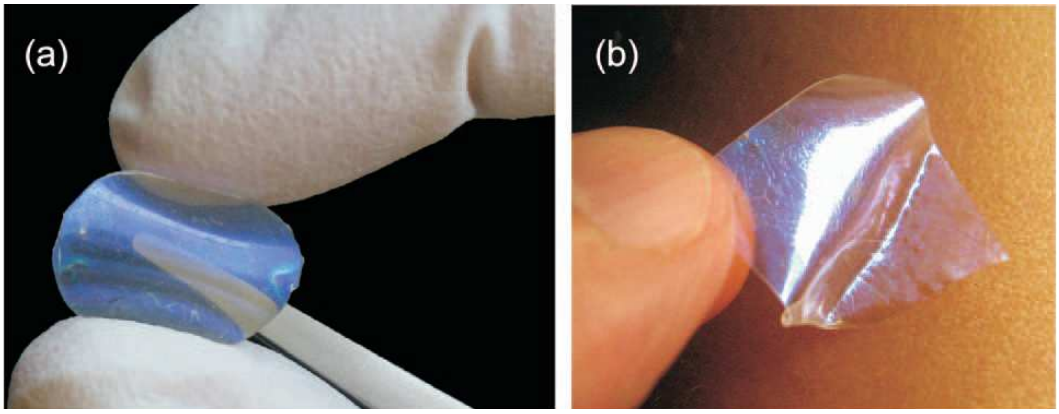

FIGURE 7: (a) Flexible one-dimensional photonic crystal based on TiO_2 and SiO_2 nanoparticles infiltrated with PDMS; (b) Similar film described in (a) but made it adhesive to human skin.

As long as TiO_2 is used to build the photonic crystal that shields against UVA and UVB radiation by absorption, the design of the multilayer must account for the mechanism of interference and for that of absorption, since TiO_2 presents an electronic band gap near 3.64eV.

Thus, a photonic crystal based on alternated SiO_2 and TiO_2 layers can be designed to overlap the photonic band-gap with the **absorption** of TiO_2 to extend the blocking to UVA regions. In Figure 7b we show one of these 1DPC designed to be adhesive to human skin, feature achieved by changing the curing agent quantity.

Objectives and Motivation of this thesis

The main objective of this thesis is the development of nanoparticle based flexible structures with photonic crystal properties that shield against UV radiation through optical reflection phenomena. The suggested approach will allow to accurately select the range of wavelengths blocked. This represents a much more efficient alternative to UV absorbing compounds, whose protection mechanism gives rise to secondary undesirable chemical reactions with the consequent photodegradation of these materials. Most of the mentioned drawbacks could be overcome with the use of the sheets whose evaluation in a real system, protecting epithelial cells from UV radiation, will be provided here. The versatility of the proposed photonic structures, due to their flexibility, transferability and adaptability to all kinds of substrates, enables them for interesting applications as UV optical filters. Furthermore, an explanation to the formation process of an all polymeric photonic crystal, with intense reflections in the UV range and compatible to flexible substrates will be presented

This thesis is structured as follows:

In **chapter 2**, it will be presented a full description of the routes followed for the synthesis of the ZrO_2, Nb_2O_5 and TiO_2 metal oxide nanoparticles used as building blocks as well as de the deposition methods used to create the photonic structures.

In **chapter 3**, Ii is shown the design and the build of a new type of nanostructured selective UV reflecting mirror: a periodical porous multilayer with photonic crystal properties deposited from colloidal suspensions of of ZrO_2, Nb_2O_5 and SiO_2 nanoparticles, with the purpose of shielding well-defined wavelength ranges of the UVA, UVB, and UVC regions of the electromagnetic spectrum while preserving transparency in the visible.

Given the versatility of these flexible nanoparticle-based Bragg mirrors as transparent UV protectors that shield selected wavelength ranges and that they can be placed over random surfaces, they will have very interesting applications. One example of this can be found in **chapter 4**, in which I designed and prepared optical structures to shield a specific UV range that it was recently demonstrated to produce carcinogenesis in skin cells. Also, an analysis of the UV protection efficiency, measured as the degree of damage caused on the DNA of different epithelial cells exposed to a broad band UV source while being protected by the flexible Bragg stacks will be made.

In **chapter 5** I will analyze the mechanism behind the formation of porous polystyrene based one dimensional photonic crystal that operates in the UV. In this case I present a study about a physical phenomena observed in polymers which leads to the creation of bi-continuous polymeric templates. This resulting polymer multilayer presents a unit cell made of two layers of different porosity as a consequence of the standing electromagnetic wave generated by thin film interference phenomenon during the irradiation stage.

This new type of materials could have many applications. For example, there are many skin problems that can be treated and cured by controlled exposure to ultraviolet and visible radiation of different types. We found two clear examples of this in the therapeutic effects of UV light on psoriasis[68], caused by the suppression of the immune system whose abnormal function in the origin of the observed inflammation , or violet light on acne vulgaris[69], through the activation of a porphyrin which finally kills bacteria (Propionibacterium acnes) responsible for the observed injuries. Phototherapy also finds utility in the treatment of eczema, skin aging[70,71], mycosis[72] or vitiligo.[73] In each case, the cure is activated by a different spectral window included within the ultraviolet range, visible or near infrared. For instance, patients of psoriasis are exposed to UV narrowband light of wavelengths between 310 nm and 315 nm, while the common acne is treated with wavelengths between 405 nm and 420 nm. In the near future, patients would benefit greatly from the existence of flexible sheets that could fit your damaged skin while blocking harmful UV radiation, and at the same time allowing transmittance windows in therapeutic ranges.

References

[1] Ren, Q.; Gailitis, R.P.; Thompson, K.P.; Lin, J.T. *Journal of Quantum Electronics*, **1990**, *26*, 2284-2288.

[2] Serpone, N.; Dondi, D.; Albini, A. Inorganica Chimica Acta 360 (2007) 794–802.

[3] Bintsis, T.; Litopoulou-Tzanetaki, E.; Robinson, R.K. *J. Sci. Food. Agric.*,**2000**, 22, 5142.

[4] Lopez Cisneros, R.; Gutarra Espinoza, A.; Litter, M.I. *Chemosphere* 48 (2002) 393–399.

[5] Nowick, M.; Richter, A.; Wolf, B.; Kaczmarek, H. *Polymer* **2003**, *44* 6599–6606.

[6] Rui Yang, P.A; Christensen, T.A.; Egerton, J.R. *Polymer Degradation and Stability* **2010**, 95, 1533.

[7] Singh, R.P.; Tomer, N.S.; Bhadraiah, V. *Polymer Degradation and Stability* **2001**, *73*, 443–446.

[8] Ting, W. *International Journal of Dermatology* **2003**, *42*, 505-513.

[9] Brash, D. *Trends in genetics* **1997**, *13*, 410-414.

[10] Demir, M.M.; Koynov, K.; Akbey, U.; Bubeck, C.; Park, I. Lieberwirth, I.; Wegner G. *Macromolecules.* **2007,** *40*, 1089-1100.

[11] Liou, G.S.; Lin, P.H.; Yen, H.J.; Yu, Y.Y.; Tsai, T.W.; Chen, W.C. *J. Mater. Chem.* **2010**, *20*, 531-536.

[12] Tu, Y.; Zhou, L.; Jin, Y.Z.; Gao, C.; Ye, Z.Z.; Yang, Y.F.; Wang, Q.L. *J. Mater. Chem.* **2010**, *20*, 1594-1599.

[13] Mazzocchetti, L.; Cortecchia, E.; Scandola M.; *ACS Appl Mater Interfaces* **2009**, *1*, 726-734.

[14] Koziej, D.; Fischer, F.; Kränzlin, N.; Caseri, W.R.; Niederberger, M. *ACS Appl. Mater. Interfaces* **2009**, *1*, 1097-1104.

[15] Druffel, T.; Mandzy, N.; Sunkara, M.; Grulke, E. *Small* **2008**, *4*, 459-461.

[16] Calvo, M.E.; Mıguez, H.; *Chem. Mater.* **2010**, *22*, 3909–3915.

[17] DeCorby,R.G.; Ponnampalam,N.; Nguyen,H.T.; Clement,T.J. *Adv. Mater.* **2007**, *19*, 193–196.

[18] Keck, J.; Roessler, M.; Scroeder, C.; Stueber, G.J.; Waiblinger, F.; Stein, M.; Legourrierec, D.; Kramer, H.E.A.; Hoier, H.; Henkel, S.; Fischer, P.; Port, H.; Hirsxh, T.; Rytz, G. Hayoz, P. *J. Phys. Chem. B* **1998**, *102*, 6975-6985.

[19] Mahltig,B.; Bottcher,H.; Rauch, K.; Dieckmann, U.; Nitsche, R.; Fritz, T. *Thin Solid Films* **2005**, *485*, 108 –114.

[20] Zayat, M.; Garcia-Parejo, P.; Levy, D. *Chem. Soc. Rev.* **2007**, *36*, 1270–1281.

[21] Parejo, P.; Zayat, M.; Levy, D. *J. Mater. Chem.* **2006**, *16*, 2165-2169.

[22] Sakai, K.; Takahashi, S.; Kobayashi, A.; Akutagawa, T.; Nakamura, T.; Dosen, M.; Kato, M.; Nagashima, U. *Dalton Trans.* **2010**, *39*, 1989–1995.

[23] Konstantinova, T**.,** Bogdanova,A.; Stanimirov,S.; Konstantinov, H. *Polymer Degradation and Stability* **1994**, *43*, 187-193.

[24] Kundu, D.; Mukherjee, R. *J. Mater. Sci. Lett*. **2003**, *22*, 1647.

[25] Hybrid Materials, 2007 WILEY-VCH Verlag GmbH & Co. KGaA, Weinheim.

[26] H. C. van de Hulst, *Dover Publications*: New York, **1981**.

[27] Henrich, V.E.; Cox, P.A. in *The Surface Science of Metal Oxides*, Cambridge University Press, New York, **1996.**

[28] Cui,H.; Zayat,M.; García Parejo,P.; Levy,D. *Adv. Mater.* **2008**, *20*, 65-68.

[29] Parlak, O.; Demir, M.M. *ACS Appl. Mater. Interfaces* **2011**, *3*, 4306-4314.

[30] Mendoza,C.; Gindy,N.; Gutmann,J.S.; Fromsdorf,A.; Forster,S.; Fahmi,A. *Langmuir* **2009**, *25*, 9571–9578.

[31] Zeng, C.;Lee. L.J**.** *Macromolecules* **2001,** *34*, 4098-4103.

[32] Ntwaeaborwa, O.M.; Kroon, O.M.; Kumar,V.; Dubroca, T.; Ahn, J.P.; Park, J.P, Swart, H.C. *Journal of Physics and Chemistry of Solids* **2009**, *70*, 1438–1442.

[33] Ellim, H.I.; Cai, B.; Kurata, Y.; Sugihara, O.; Kaino, T.; Adschiri, T.; Chu, A.L.; Kambe, N. *J. Phys. Chem. B* **2009**, *113*, 10143–10148.

[34] Lu, C.; Yang, B.; *J. Mater. Chem.* **2009**, *19*, 2884–2901.

[35] Kickelbick, G. *J. Sol-Gel Sci. Technol.* **2008**, *46*, 281-290.

[36] Liou, G. S.; Lin, P. H.; Yen, H. J.; Yu, Y. Y.; Chen, W. C. *J. Polym. Sci. Part A: Polym. Chem.* **2010**, *48*, 1433–1440.

[37] Cortecchia, E.; Mazzocchetti, L.; Scandola, M. Macromol. Chem. Phys. 2009, *210*, 1834–1843.

[38] Mazzocchetti, L.; Scandola, M.; Pollicino, A. Polymer **2008**, *49*, 5215-5224.

[39] Nakade,M.; Ichihashi, K.; Ogawa, M. *J. Sol-Gel Sci. Technol.* **2005**, *36*, 257-264.

[40]. Xia, Y.N.; Whitesides, G.M. *Angew. Chem. Int. Ed.* **1998**, *3*, 551-575.

[41]. Demir,M.; Memesa,M.; Castignolles,P.; Wegner, G. *Macromol. Rapid Commun.* **2006**, *27*, 763–770.

[42] Li, Y.Q.; Fu, S.Y.; Mai. Y.W. *Polymer* **2006**, *47*, 2127-2132.

[43] Scholz, S.; Kaskel, S. *J. Colloid Interface Sci.* **2008**, *323*, 84-91.

[44] Seeatapan, N.; Panyathammaporn, T. *Macromol. Symp.* **2008**, *264*, 50–53.

[45] Ge, J.; Zeng, X.; Tao, X.; Li, X.; Shen, Z.; Yun, J.; Chen, J. *Journal of Applied Polymer Science* **2010**, *118*, 1507–1512.

[46] (a) Tooley, I. R.; Gibson, R.R. patent number WO2007144577 (A1); (b) Tooley, I. R.; Gibson, R.R. patent number WO2007144576 (A2).

[47] Míguez, H.; Calvo, M.E. Spanish patent number P201130472.

[48] Calvo, M.E.; Sánchez-Sobrado, O.; Lozano, G.; Míguez, H. *J. Mater. Chem.* **2009**, *19*, 3144-3148.

[49] Sanchez Sobrado,O.; Calvo,M.E.; Miguez,H. *J. Mater. Chem.*, **2010**, *20*, 8240.

[50] Macleod, A. in *Thin film optical filters*, Institute of Physics Publishing, London, 3rd ed., **2001**.

[51] Joannopoulos, J.D. et al. in Photonic crystals:molding the flow of light, Princeton University Press, Princeton, 2nd ed., 2008.

[52] Yablonovitch, E. Phys. Rev. Lett. 58, (1987), 2059.

[53] John, S. Phys. Rev. Lett. 58, (1987), 2486.

[54] Ho, K.M.; Chan, C.T.; Soukoulis, C.M. Phys. Rev. Lett. 65, (1990), 3152.

[55] Rayleigh, L. *Phil. Mag*, **1887**, 24(147):145-159.

[56] Matthew M. Hawkeye and Michael J. Brett. *J. Appl. Phys.*, **2006**, 100, 044322.

[57] Langer, R.; Barski, A.; Simon, J.; Pelekanos, N.T.; Konovalov, O.; André, R.; Dang L.S. *Appl. Phys. Lett.*, **1999**, Vol. 74, No. 24.

[58] Hiller, J.A.; Mendelsohn, J.D.; Rubner, M.F. *Nature Materials*, **2002**, 1, 59 – 63.

[59] Mahnkopf, S.; Kamp, M.; Forchel, A.; März, R. *Appl. Phys. Lett.*, 2003, 82, 2942.

[60]. Urbas, A.; Sharp,R.; Fink,Y.; Thomas,E.L.; Xenidou,M.; Fetters,L.J. *Adv. Mater.* **2000**, *12*, 812-814.

[61] Bailey, J.; Sharp, J.S. *J. Polym. Sci., Part B: Polym. Phys.*, **2011**, *49*, 732–739.

[62]. Colodrero,S.; Ocaña, M.;Míguez,H. *Langmuir*, **2008**, *24*, 4430-4435.

[63] Calvo, M.E.; Colodrero,S.; Hidalgo,N.; Lozano, G.; López López, C.; Sánchez-Sobrado, O.; Míguez, H. *Energy & Envirom. Sci*. **2011**, *4*, 4800-4812.

[64] Bonifacio, L. D.; Lotsch, B. V.; Puzzo, D.P.; Scotognella, F.; Ozin, G.A. *Adv. Mater.*, **2009**, *21*, 1641.

[65] Colodrero, S.; Mihi, A.; Häggman, L.; Ocaña, M.; Boschloo, G.; Hagfeldt, A.; Míguez, H. *Adv. Mater.*, **2009**, *21*, 764-770.

[66] Bonifacio, L.D.; Puzzo, D.P.; Breslav, S.; Willey, B.M.; McGeer, A.; Ozin, G.A. *Adv. Mater.*, **2010**, *22*, 1351-1354.

[67] Míguez, H.; Calvo, M.E. Patent number WO2010/086483 A1.

[68] Parrish, J.A.; Jaenecke, K.F. *J. Investigat . Dermat . ,* **1981** , 76, 359.

[69] Sigurdsson V , AC Knulst , H. van Weelden , *Dermatology*, **1997** , 194 , 256.

[70] Reynolds, N.J.; Franklin, V.; Gray, J.C.; Diffey, B.L.; Farr, P.M. *Lancet*, **2001**, 357, pp. 2012–2016.

[71] Fournier N, Fritz K, Mordon S, *Dermatol Surg*, **2006**,32:1140-1146.

[72] Gathers RC, Scherschun L, Malick F, Fivenson DP, Lim HW, *J Am Acad Dermatol*, **2002**, 47: 191–197.

[73] Schershum L, Kim J, and Lim HW, *J Am Acad Dermatol*, **2001**, 44: 999-1003.

Chapter 2

Nanoparticle synthesis and multilayer preparation methods

Introduction

In this section, the synthesis routes followed in this thesis to achieve stable nanoparticle suspensions of ZrO_2, Nb_2O_5 and TiO_2, as well as the deposition methods employed to form the multilayer system without the need of heat treatment will be explained. The obtained nanoparticles, which give the possibility to extend the range in the UV without the presence of absorption, are monodisperse and present sizes in the 5-30 nm range to avoid diffuse scattering in the system. These requirements are necessary to obtain uniform optical quality thin films. In this sense, the sol-gel method is a versatile method that gives the possibility to control the size of the nanoparticles and the degree of aggregation. Both parameters allow us to control the porosity of the multilayer system, a key feature that will make possible polymer infiltration in the structure to create flexible films, whose preparation details are provided also.

Nanoparticle synthesis

The Sol-Gel process[1-3] is one of the most used synthetic routes to prepare several inorganic compounds or organic-inorganic hybrids in a wide variety of structures such as thin films[4],

nano-sized powders[5], nanoparticles[6], among others. In this thesis, this method is chosen, since it gives the possibility to control the final microstructure of the nanoparticles synthesized. The sol-gel path involves a liquid solution (sol) containing a chemical precursor: a metal atom surrounded by organic or inorganic ligands. Depending on the chemical nature of the ligands, precursors may be classified into two different categories:

- Inorganic precursors, many inorganic salts such as nitrates, chlorides or acetates. The inorganic route involves the formation of condensed species from aqueous solutions of the inorganic salts by adjusting the pH.

- Metal-organic precursors, usually metal alkoxides M-$(OR)_x$, with the bonds alkoxy (OR), optionally in combination with alkyl chains (R'), linked to the metal atom (M).

Sol-gel processing of metal alcoxides occurs through a mechanism of inorganic polymerisation based on two reactions: the hydrolysis and condensation. The metal alkoxides, which are generally highly hydrolyzable compounds, react with the added water. Therefore, a hydroxyl group binds to the atom metal via Equation 1 below:

Eq. 1: $\text{M-(OR)}_4 + \text{H}_2\text{O} \rightarrow \text{HO-M-(OR)}_3 + \text{ROH}$

Depending on the amount of water added in the presence of acidic or basic catalysts, the hydrolysis may be complete, that is to say that all the OR groups are replaced by hydroxyl groups (equation 2):

Eq. 2: $\text{M-(OR)}_4 + 2\ \text{H}_2\text{O} \rightarrow \text{M-(OH)}_4 + 4\ \text{ROH}$

However, the hydrolysis is generally stopped before the reaction was completed, giving place the presence of species $(HO)_n$-M-$(OR)_{4-n}$. Two molecules (partially) hydrolysed can then be linked by a condensation reaction, and removal of protonated species occurs in the form of alcohol (alkoxylation) or water (oxolation) from equations 3 or 4:

Eq. 3: $(\text{OR})_3\text{-M-OR} + \text{HO-M-(OR)}_3 \rightarrow (\text{OR})_3\text{-MOM-(OR)}_3 + \text{ROH}$

Eq. 4 : $(\text{OR})_3\text{-M-OH} + \text{HO-M-(OR)}_3 \rightarrow (\text{OR})_3\text{-MOM-(OR)}_3 + \text{H}_2\text{O}$

Reactions described by Eqs. 1 to 4 are based on nucleophilic attack mechanisms. These mechanisms can be activated by the use of acid-base catalysts, which allow a separation of the

hydrolysis-condensation reactions and selective activation mechanisms reaction. Conventionally, acid catalysts (eg, HCl or HNO_3) increase the rate of hydrolysis, while basic catalysts promote the condensation. In addition, the complete liquid-solid transformation in some of the sol-gel routes (Eg, ZrO_2 synthesis explained in this chapter), is carried out at ambient temperature.

By controlling the synthesis conditions carefully, these reactions may lead to a variety of structures, and to different final states for the materials, showing the great flexibility of this technique to adapt to different system requirements.

After a stable solution of nanoparticles is achieved, the remaining point is to convert these separated materials into a solid layer with the aim of using the physical or chemical properties as a porous film on a substrate. The liquid processing approach, based on dip- or spin coating of different types of suspensions is a well stablished method to deposit thin layers of , metal oxides nanoparticles. The stacking of layers of nanoparticles of different type can be also made. In my group, a detailed analysis of the effect of the spin-coating protocol over the structural and optical properties of nanoparticle based one-dimensional photonic crystals was demonstrated in the past.[7]

Spin-Coating

Spin coating of diluted suspensions is a widespread technique used to produce thin, uniform films on a planar substrate. It has been one of the preferred methods to deposit polymer thin films or nanoparticle layers out of colloidal suspensions, both of them studied in this thesis.

Meyerhofer[8] was the first to explain the dependence of the final thickness of a spin coated film on the processing and some important key parameters like angular velocity, viscosity and solvent evaporation rate by the semi-empirical formula shown in equation 5.

Eq. 5:
$$h = \left(1 - \frac{\rho_A}{\rho_{Ao}}\right)\left(\frac{3\eta m}{2\rho_{A_0} w^2}\right)^{\frac{1}{3}}$$

Were ρ_A is the mass of volatile solvent per unit volume, ρ_{Ao} is the initial value of ρ_A, η is the viscosity , w is the angular speed and m is the evaporation rate of the solvent.

In a spin coating standard course, at the beginning, a solution is deposited on a substrate (Figure 1a), that is subsequently accelerated until it reaches the preselected rotation rate. Liquid flows following a radial geometry, as a result of the action of centrifugal force, and the overload is cast out off the edges of the substrate (Figure 1b). The film will thin gradually in a continuous process until disjoining pressure effects provokes the film to arrive at an equilibrium thickness in viscosity from solvent evaporation.(Figure 1c) The last thinning of the film is next owed

exclusively to solvent evaporation.(Figure 1d) A complete description of the basic principles of this process is given in Bornside et al.

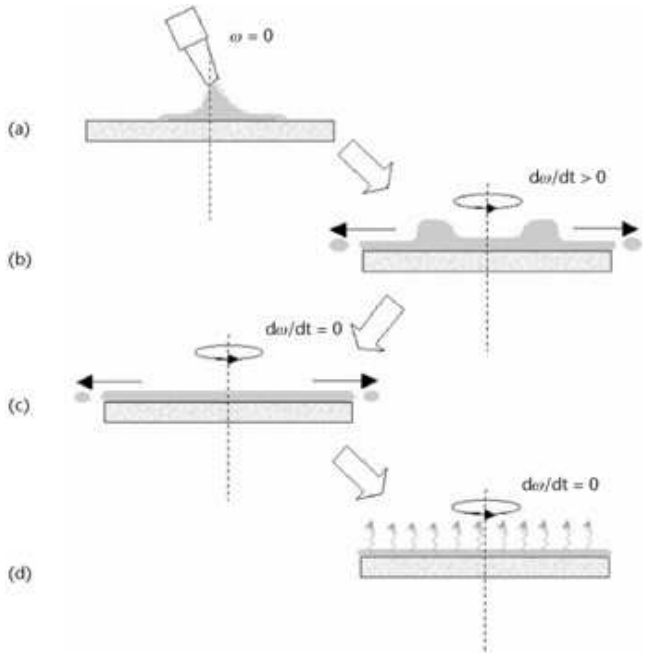

Figure 1: Four stages of spin coating (a) solution dispersion, (b) acceleration, (c) viscous force influence during steady spinning, and (d) solvent evaporation process during steady spinning.

This method is particularly interesting because the delay in obtaining a multilayer material is very short (a few minutes). In the specific case of the deposition of nanoparticles, in a work perfomed by our group[7], it was shown that the spin coating protocol can be used to study the optical properties of the photonic crystals and therefore, the same equations mentioned so far can be applied to a porous multilayer system. The thickness of the materials can be controlled by varying the concentration of particles in the suspension or on the rotational speed. On the other hand material thickness is uniform over the entire substrate surface.

Dip-Coating

The simplest scheme of sol-gel dip coating consists in the immersion and withdrawal of a substrate into and from a solution: gravitational dripping and solvent evaporation, added to further condensation effect, causes the formation of a thin solid film. The structure of films deposited depends on such factors as size and structure of the precursors, different parameters of condensation and evaporation, capillary force, and substrate withdrawal speed. The dip coating process can be divided into three steps (Figure 2): Immersion of the substrate after surface

preparation, removing the substrate at a controlled rate, thereby forming a wet film and, gelling of the layer by solvent evaporation.

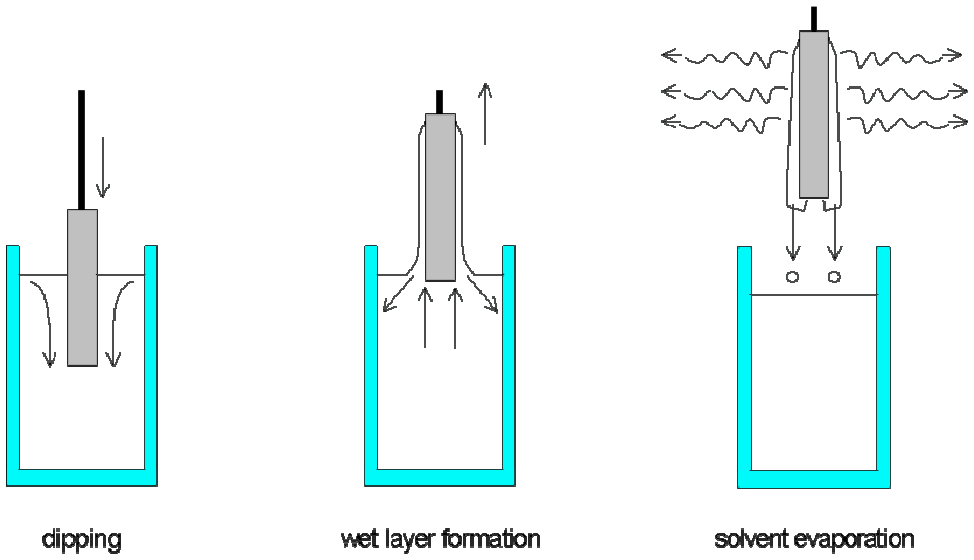

Figure 2: Stages of the dip coating process: dipping of the substrate into the coating solution, wet layer formation by withdrawing the substrate and gelation of the layer by solvent evaporation.

During the extraction process, a layer of liquid is entrained on the surface the substrate, generating a combination of viscous and gravitational forces that determine the thickness of the liquid film *h* formed on the substrate surface[9], according to equation 6 for a Newtonian fluid:

Eq. 6:
$$h = 0.94 \frac{(\eta v)^{\frac{2}{3}}}{\gamma_{LV}^{1/6} (\rho g)^{\frac{1}{2}}}$$

In this equation, v is the withdrawal speed, η is the viscosity of the solution sol-gel, ρ is the density of the sol-gel solution, g is the universal gravitational constant, and γ_{LV} is the liquid–vapour surface tension. The dip coating technique has the advantage of being used to cover large symmetrical areas or substrates with complex geometries, and not only used to generate the coating via sol-gel route. This method generates an homogeneous coating thickness across the surface area the substrate to be coated, except for the edges where the thickness of coating is usually higher.

Titanium oxide nanoparticle suspensions

The synthesis and the characterization of different types of metal oxide nanoparticles that allowed me to build flexible multilayer structures will be shown in what follows.

The sizes of the nanoparticleswere obtained by dynamic light scattering (DLS, Malvern, Zetamaster) using water dispersions. All nanoparticles used in this thesis were diluted in methanol in concentrations ranging from 1 to 4wt%. This alcohol is chosen since no coagulation is produced in the suspension has been prepared in this way[10] and at the same time, the medium is volatile enough to obtain liquid-free films in a few seconds.

TiO_2 nanocrystals were synthesized following a route based on the hydrolysis of titanium isopropoxide (TTIP 97%, Aldrich), continued with the growth under hydrothermal conditions. Titanium isopropoxide (IV) (20 mL)[11] were added to 36 mL of Milli-Q water and stirred for 1 h. The resulting white solid was filtered by employing 1.2 mm RTTP Millipore sieves and then was washed numerous times with distilled water and put in a Teflon reactor containing 3.9 mL of 0.6 M tetramethylammonium hydroxide (TMAOH 25%, Fluka). Peptization occurs by heat treatment in a furnace at 120 °C for 3 h. Afterwards, a colloidal suspension of anatase crystallites is achieved. Next, centrifugation at 14 000 rpm for 10 min makes possible the removal of outsized aggregates out of the dispersion. In figure 3, a simple schematic representation of the synthesis route is shown.

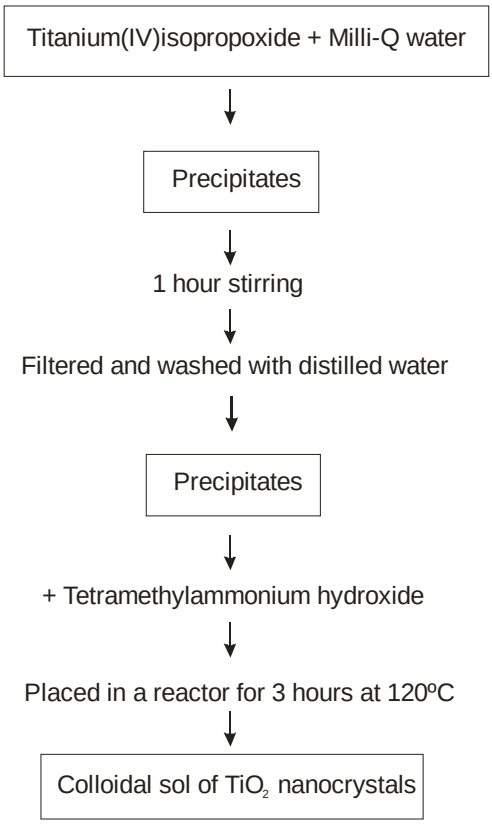

Figure 3: Schematic representation of the synthesis route of TiO2 sols.

The obtained size for TiO_2 nanoparticles is around 30nm, as can be appreciated in Figure 4a. The high transmittance shown for a layer made only with this nanoparticles (Figure 4b),

corresponding to 500 nm, indicates that this size does not cause diffuse scattering, that would negatively affect the transparency of the coating. TiO_2 presents the electronic bandgap (EBG) edge at λ= 340 nm (Egap = 3,64 eV), as can be noted also in Figure 4b. The EBG is a consequence of direct electronic transitions in the anatase nanoparticles.

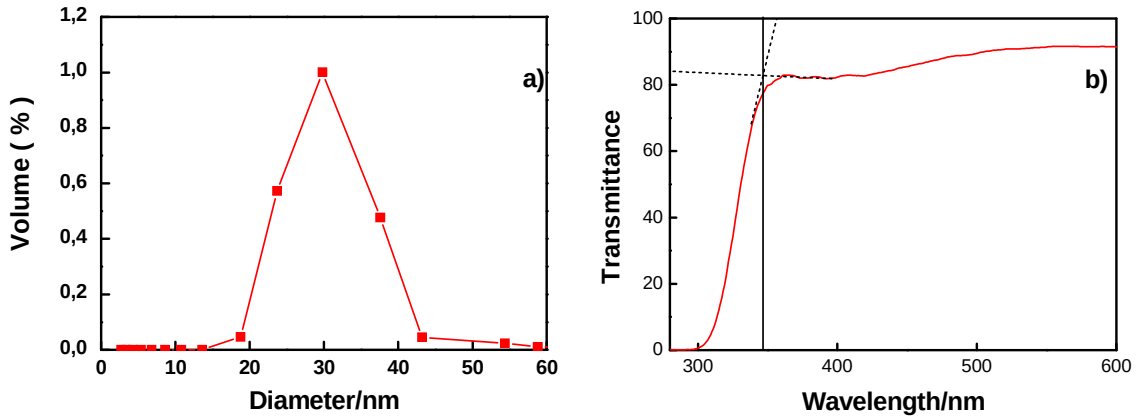

Figure 4: a) Volumetric particle distribution size of colloidal nanoparticles made of SiO_2 (red squares). b)Transmittance spectrum of a 500nm layer coating of TiO_2 deposited over quartz by means of a spin coater.

The latter is obtained extrapolating the rising parts of the absorption edge and the Fabry-Perot oscillations, taken from of TiO_2 monolayer transmittance spectrum, as shown in Figure 5b.

Preparation of Nb_2O_5 nanoparticles

The suspension of Nb_2O_5 nanoparticles was prepared using niobium pentachloride[12] (Figure 5) (99%, Alfa Aesar) as precursor in the synthesis route as can be seen in Figure 6. The initial step consisted in the addition of 2 g of $NbCl_5$ in 18.5 ml of absolute ethanol. Then, 0.847ml of glacial acetic acid was added to the mixture and left in sonication for 5 min. Afterwards, the solution was hydrolyzed with 4.9 ml of distilled water, enough to obtain a H_2O:Nb ratio equal to 35. This ratio was optimized to obtain particles with 18-20 nm of diameter, without gelification. High hydrolysis ratios lead to niobium oxide nanoparticles with larger diameters, as described elsewhere.[12]

A high content of water ends up in a high degree of hydrolysis that additionally causes the condensing polymerisation. The final concentration of the sol was approximately 6%. Stable transparent Nb_2O_5 solutions were obtained. The sols are stable for a long period of time at room temperature when kept in a hermetic glass flask.

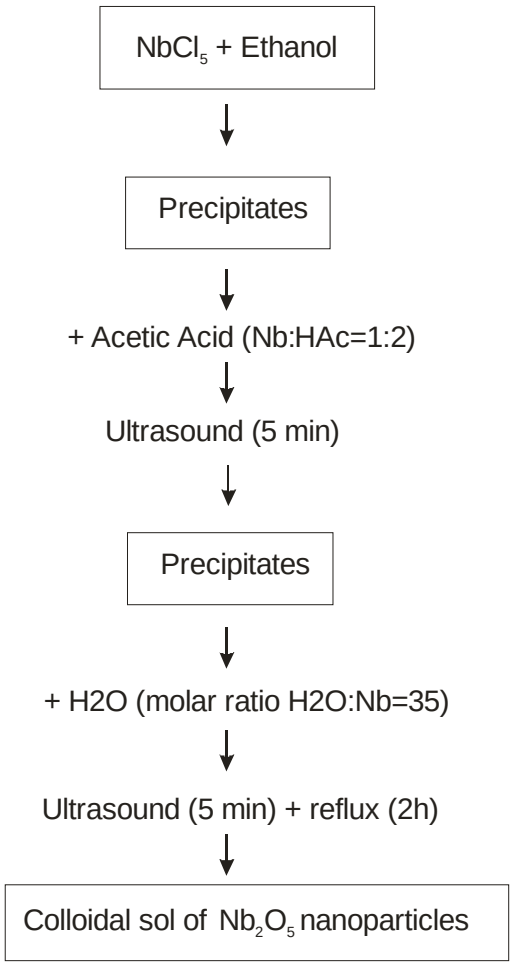

Figure 5: Basic flow chart showing the sol-gel process used to obtain a suspension of Nb_2O_5 nanoparticles.

The obtained nanoparticles present a diameter around 18nm as shown in Figure 6a. Nb_2O_5 nanoparticles present the absorption edge in approximately 315 nm ((Egap = 4 eV), as can be seen in Figure 6b.

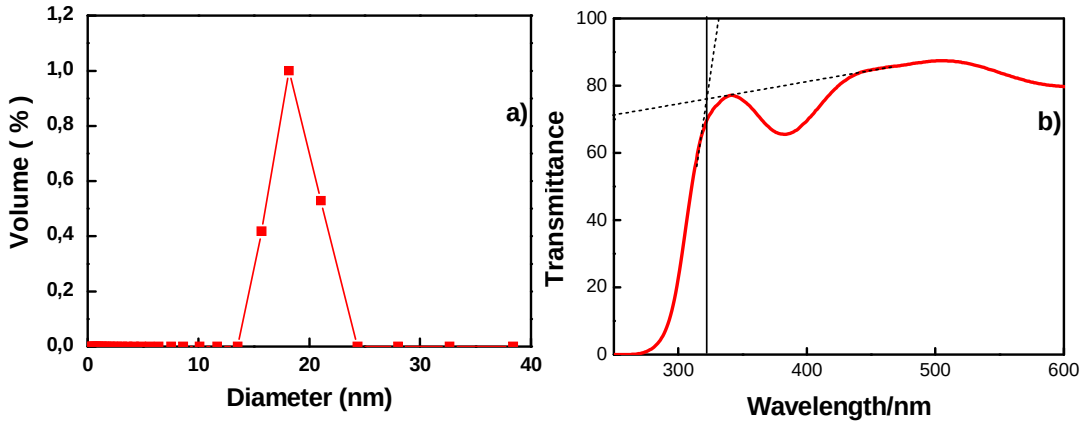

Figure 6: a) Volumetric particle distribution size of colloidal nanoparticles made of Nb_2O_5 (red squares). b)Transmittance spectrum of a 400nm layer coating of Nb_2O_5 deposited over quartz by means of a spin coater.

Zirconium oxide nanoparticle suspensions

ZrO_2 nanoparticles were synthesized using a procedure based on the hydrolysis of zirconium n-propoxide.[13] A stable ZrO_2 nanoparticle suspension is achieved by the slow addition of 3.7 ml of zirconium n-propoxide (70%, Alfa Aesar) in 50 ml of Milli-Q water acidified with 1ml of HNO_3 (65%, Prolabo) under strong stirring, as shown in Figure 7. Immediately after the addition of the zirconium alkoxide a white precipitate is formed. Peptization in acid medium allows controlling particle size in the desired range, while dialysis provides the necessary surface charge to realize the layer by layer assembly of ZrO_2 particles from methanol/water suspension. The complete peptization of the solid took place under room temperature for approximately 72 h. Next, the colloidal suspension was dialyzed against pure Milli-Q water in a membrane (MWCO=10000, Spectra/Por) until pH=3. Finally, water was removed by distillation at reduced pressure and particles were re-suspended in methanol, in concentrations ranging from 3% to 4% wt.

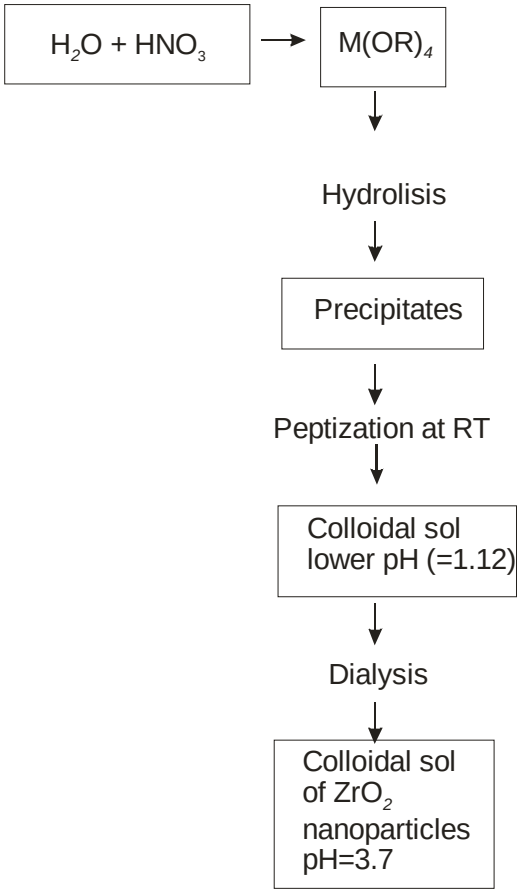

Figure 7: Diagram with the hydrolysis and condensation process to achieve ZrO_2 nanoparticles.

The obtained nanoparticles had a diameter of approximately 6 nm as can be seen in Figure 8a. As can be appreciated in Figure 8b, ZrO_2 nanoparticles present an absorption edge at λ=220nm (Egap = 5,63 eV).

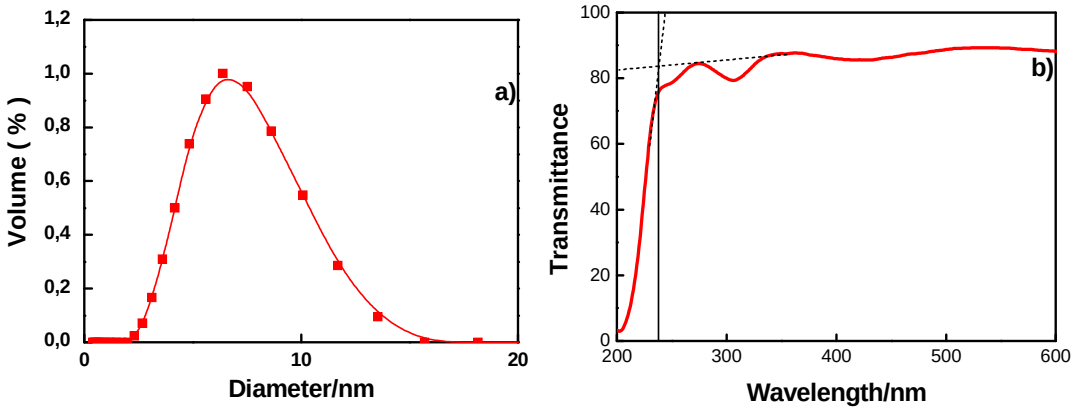

Figure 8: a) Volumetric particle distribution size of colloidal nanoparticles made of ZrO_2 (red squares). b)Transmittance spectrum of a 400nm layer coating of ZrO_2 deposited over quartz by means of a spin coater.

It should be mentioned that particles obtained by other ZrO_2 sol-gel synthesis tested were proven to yield bad optical quality multilayers due to imperfections introduced at different stages of the construction of the Bragg stack.

As can be seen in numerous, the SiO_2 spherical nanocolloids are widely used as refractive index partner to other high refractive index nanoparticles when it comes to build a photonic crystal.[14-16] In our particular case, the SiO_2 dispersions were purchased from Dupont (Ludox TMA, Aldrich). The suspension is highly stable and monodisperse, as can be seen in Figure 9a.

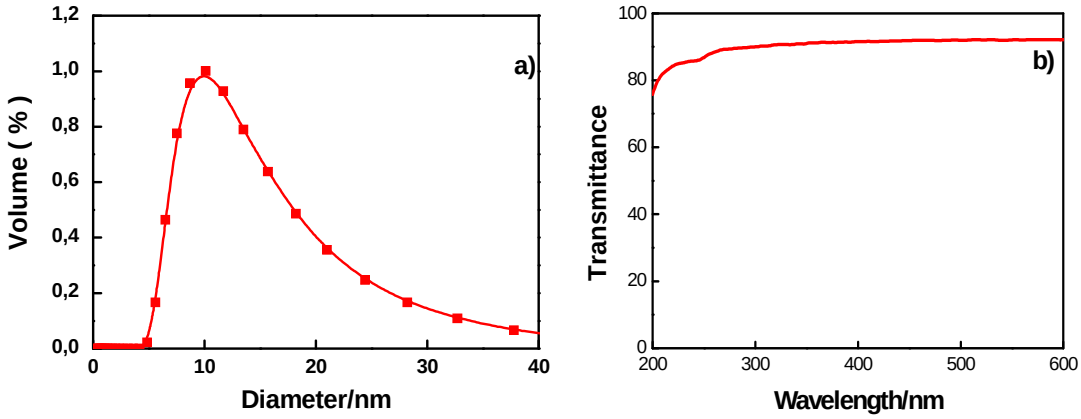

Figure 9: a) Volumetric particle distribution size of colloidal nanoparticles made of SiO_2 (red squares). b) Transmittance spectrum of a 500nm layer coating of SiO_2 deposited over quartz by means of a spin coater.

Moreover, SiO_2 nanocolloids do not present absorption in the UVA, UVB and the less energetic part of UVC, as it can be appreciated in Figure 9b.

Procedure to obtain flexible films

The first step is to make a liquid mixture with the elastomer precursor (EP) and the curing agent (CA) (Sylgard 184 elastomer kit, Dow Corning). The mass ratio EP:CA of these two compounds was kept fixed at 10 to 1, in order to guarantee an optimized polymerization. Subsequently, the infiltration of the blend can be prepared by dropping a defined quantity onto the inorganic backbone by means of spin coating (45 s, 700 rpm). Then, samples were cured at 110 ºC in a stove during 30min. Next, we made square incisions in the PDMS layer with a blade, and we immersed the infiltrated multilayer supported onto the glass in liquid nitrogen (77K).We then allowed samples to get to room temperature, and after that, the films were lifted from the substrate.

References

[1] Livage, J; Sanchez, C. *Journal of Non-Crystalline Solids*, **1992**, 145, 11-19.

[2] Robert, J.; Corriu, P.; Leclercq, D. *Angew.. Chem. Int. Ed.*, **1996**, 35, 1420-1436.

[3] Brinker, C.J.; Sherrer, G.W. *Sol-Gel Science*, **1990**, Academic Press Inc, San Diego.

[4] Lu, Y.; Ganguli, R.; Drewien, C.A; Anderson, M. T.; Brinker, C. J.; Gong, W.; Guo, Y.; Soyez, H.; Dunn, B; Huang, H.; Zink, J.I. *Nature*, **1997**, 389, 364-368.

[5] Chang, Y.S.; Hwei, Y.; Chen, I.; Chen, G.J.; Chai, Y.L. *Journal of Crystal Growth*, **2002**,243 319–326.

[6] Lu, Y.; Yin, Y.; Mayers, B.T.;Xia, Y. *Nano Lett.*, **2002**, Vol. 2, No. 3.

[7] Calvo, M.E.; Sanchez-Sobrado, O.; Colodrero, S.; Mıguez, H. *Langmuir* **2009,** *25*, 2443-2448.

[8] Meyerhofer, D. *J. Appl. Phys.*, **1978**, 49, 3993-3997.

[9] Scriven, L.E. *Materials Research Society*, **1998**, 717.

[10] Thomas, I.M., *Appl. Opt.*, **1987**, 26, 4688.

[11] Burnside, S.D.; Shklover, V.; Barbe, C.; Comte, P.; Arendse, F.; Brooks, K.; Gratzel, M. *Chem. Mater.*, **1998**, 10, 2419.

[12] Guo, Y; PhD Thesis, "Nanocrystalline sol-gel Nb2O5 coatings
Preparation, characterisation and application to photovoltaic cell, lithium battery and electrochromic device", 2002, Saarbrucken.

[13] Xu, Q.; Anderson, M.A. *J. Mater. Res.*, **1991**, *6*, 1073.

[14] Velikov, K.P.; Dillen, T.; Polman, A.; Blaaderen. A. *Appl. Phys. Lett.*, **2002,** 81, No. 5.

[15] O'Brien, P.G.; Yang, Y.; Chutinan, A.; Mahtani, P.; Leong, K.; Puzzo, D.P.; Bonifacio, L.D.; Lin, C.W.; Ozin, G.A.; Kheran, N.P. *Solar Energy Materials & Solar Cells*, **2012,** 102 173–183.

[16] Sanchez-Sobrado, O.; Calvo, M.E; Mıguez, H. *J. Mater. Chem.*, **2010**, 20, 8240–8246.

Chapter 3

Flexible nanoparticle one dimensional photonic crystals for UV radiation protection purposes

Introduction

In this chapter, a detailed procedure is explained on how to build and design porous nanoparticle one dimensional photonic crystals in order to create flexible films to protect against ultraviolet radiation by optical reflection. The system is based on a periodical porous multilayer structure made by the alternating deposition layers of ZrO_2 or Nb_2O_5 and SiO_2 nanoparticles through spin coating route. For this purpose, SiO_2, ZrO_2 and Nb_2O_5 nanoparticles whose detailed synthesis was given in chapter 2, are used. For UVA protection, I propose a Nb_2O_5/SiO_2 nanoparticle one dimensional photonic crystal, while for efficiently blocking different UV wavelength ranges comprised between λ=200nm and λ=400 nm, I present a series of ZrO_2/SiO_2 photonic crystal films. I will describe the method[1,2] used for the creation of a flexible nanoparticle based one dimensional photonic crystal, that is able to block effectively the UV wavelengths through reflection, while keeping a high transparency in the visible. I will show optical characterization evidence of how the high refractive index contrast between the different types of nanoparticle layers gives rise to intense Bragg reflections at the targeted wavelengths. The main results of the built flexible material as effective UV radiation filters, and

a comparison to other state-of-the-art materials in this field of thin film transparent UV protective coatings will be evaluated.

Nb_2O_5/SiO_2 one dimensional photonic crystals: rigid phase.

Porous 1DPCs were made following the alternated deposition of two different nanoparticulated layers of SiO_2 and $Nb2O_5$, prepared by spin coating. In order to ensure pore connectivity between the resulting layers and avoid diffuse scattering, it is indispensable to use solutions of colloidal particles of nanometer size as mentioned in the previous chapter.[3] Particles with sizes close or above to 100nm, affect the optical quality, with light scattering induced. Also, for narrow distributions, pore size will increase with the average particle size, and hence, the existence of large pores stimulates the interconnectivity and accessibility of the system.[4]

In order to deposit the layers of SiO_2 and Nb_2O_5 nanoparticle the precursor suspensions were spun cast over clean glass substrates using a spin coater equipment in which both the acceleration ramp and the final rotation speed could be precisely determined. Rotation speed was selected between the values of 2000 and 6000 rpm and acceleration ramp was kept constant at 7150 rpm s-1. The complete spin-coating progression (ramping-up and final speed) is concluded in 60 s. The procedure is reiterated until all layers have been deposited.

With the aim of analyzing important parameters of the resulting Bragg peak such as its intensity and spectral width, a fit of the reflectance spectra was made by a code based on a transfer matrix formalism developed in our group.[5] The output of the simulations gives the values of the refractive indexes and the thickness of the forming layers. From this procedure, we estimate $n(Nb_2O_5)$=1.76 and $n(SiO_2)$=1.31, corresponding to pore volume fractions of 40% and 28% respectively. Values of 2.26 and 1.43 are taken for the refractive indexes of bulk Nb_2O_5 and SiO_2 in the visible. Microstructural features of these porous 1DPC, spin coated onto cristal substrates, can be explored by FESEM images taken from a microscope Hitachi 5200 working at 5 kV. A FESEM cross section image of a SiO_2/Nb_2O_5 nanoparticle multilayer discloses a homogeneous layer thickness with flat interfaces flanked by them (Figure 2a).

In figure 2b we can see a backscattered electron picture of the same geometrical region, revealing visibly uninterrupted and even interfaces connecting successive layers, with more intense lines belonging to Nb_2O_5 layers. Being able to differentiate both layers so clearly and that the bright fringes fom the backscattered electrons corresponding to Nb_2O_5 layers present a similar thickness from what we can distinguish in the secondary electron image, tells us that there is no considerable interpenetration that could affect the refractive index contrast and therefore the intensity of Bragg peaks. Calculated thicknesses from FESEM images were 35nm and 65nm for Nb_2O_5 and SiO_2 layers respectively. Also, the thickness of the layers was estimated from Field Emission Scanning Electron Microscopy (FESEM) images, which is going

to be used as an input value in the simulations. FESEM analysis puts in evidence that up to 20 layers can be stacked by spin coated assisted layer by layer deposition without an intermediate thermal treatment, as it usually occurs for other combinations of metal oxides.[6] Above this layer number, samples started to collapse due to tensile stress. It should be mentioned that nanoparticle films are stable against disassembly in the same dispersion medium from which they were deposited.[7]

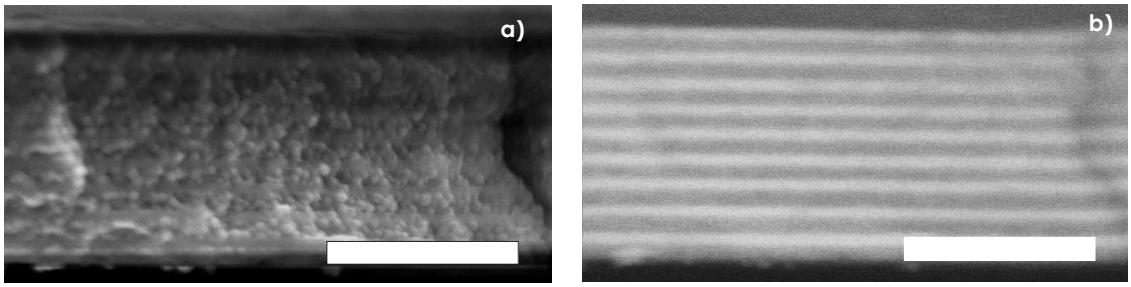

Figure 2: FESEM images of the cross sections of a 20 layer 1D photonic crystal made of SiO_2 (spherical colloids) and Nb_2O_5 nanoparticles respectively, obtained using (a) secondary and (b) backscattered electron detection. Scale bar is 1 µm in both figures.

The deposition technique employed and the control of the nanoparticle solution concentration permits having a precise location of the Bragg peaks at different spectral positions. In Figures 3a, 3b and 3c we present sets of total reflectance, total transmittance and calculated absorptance spectra, obtained from Nb_2O_5 1DPCs deposited at different rotation speeds and concentrations. Optical characterization was performed using a UV-Visible scanning spectrophotometer (SHIMADZU UV-2101PC) with an integrating sphere attached, working in both total reflection and total transmission modes. The absorptance of samples were calculated using the expression $A = 1 - T_T - R_T$, in which T_T and R_T are the total transmittance and the total reflectance respectively. The measurements cover the wavelength region from 200 to 800 nm.

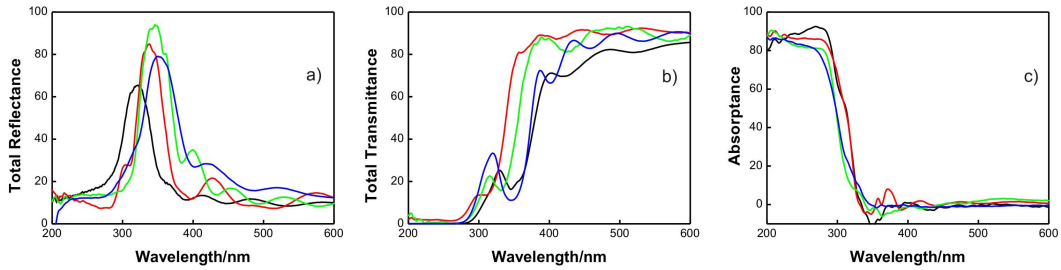

Figure 3: a) Total reflectance, b) total transmittance, and c) absorptance from SiO_2/Nb_2O_5 bragg stacks. Final rotation speeds were 3000 rpm (blue), 4000 rpm (green), 5000 rpm (red) and 7000 rpm (black). Concentrations of SiO_2 and Nb_2O_5 nanoparticles were kept at 2.5 % in all cases. Acceleration ramp (γ = 11500 rpm/s) was kept constant.

It can be seen that high intensity reflectance peaks that shield against UV radiation from 300 to 400 nm through reflection were obtained, avoiding absorption as can be appreciated in fig 3c.

Also, the transparency of the samples in the visible region (390–750 nm), estimated according to standard methods commonly employed to determine light transmittance of solar radiation for glazing in buildings (ISO 9050:2003), which takes into account the photopic response of the eye, is around 90%. In these periodic multilayer systems, it is feasible to introduce an "optical defect" disrupting the periodicity of these symmetric systems to create allowed states in the photonic band gap. In Fig. 4 we show a total transmittance spectra of a porous SiO_2/Nb_2O_5 1DPC in which a thicker SiO_2 layer was inserted in the middle of the multilayer structure. The result of the existence of these optical cavities is the opening of a narrow transmission peak within the prohibited wavelength range, as shown. The position of this maximum will be determined by the optical thickness of the middle layer. These optical resonators present many applications[8,9], for instance, these relatively sharp transmission windows can be designed to control slight changes of refractive index in the pores of the cavity, permitting to sense the presence of vapors inside the pore walls of the structure with great accuracy.[10]

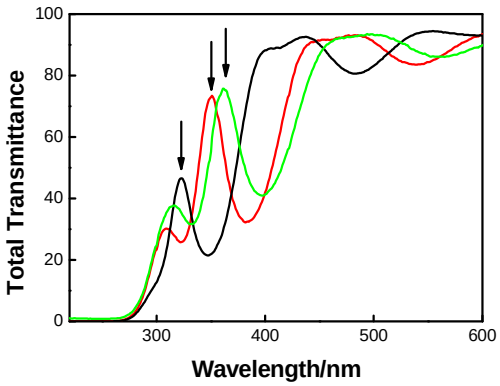

Figure 4: Total Transmittance spectra of a set of porous optical resonator made of SiO_2/Nb_2O_5 nanoparticles. Final rotation speeds were 6500 rpm (Black), 5000 rpm (Red) and 4000 rpm (Green). Concentrations of SiO_2 and Nb_2O_5 nanoparticles were kept at 2.25 % in all cases.

Nb_2O_5/SiO_2 one dimensional photonic crystals: infiltrated phase.

In order to study the structural behavior of the sample by analyzing its optical properties two experiments were made: Two identical couples of rigid 10 (SiO_2/Nb_2O_5) 1DPC were built at 6000rpm. One of them was infiltrated and left to polymerize at room temperature for 72 hours, while the other one was polymerized at 110ºC for 30 minutes, following the standard procedure described previously in this work. The initial position of the Bragg peak of the sample was located at 346nm. As expected, the Bragg peak intensities of both infiltrated samples was slightly attenuated, since the refractive index contrast is reduced after filling the pores with PDMS as can be seen in Figure 5. The Bragg peak corresponding to the sample heated shifted 6 nm to the red side of the spectrum. We believe it is due to evaporation of remaining solvent in the system, thus reducing the thickness of the sample. On the other hand, without heat

treatment, the thickness remains constant, but after infiltration, the average refractive index increases in both layers, the peak red shifting 6 nm.

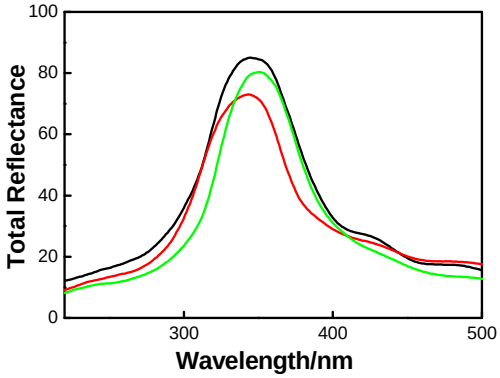

Figure 5: Total Reflectance spectra of: (Black) Rigid porous SiO_2/Nb_2O_5 10 unit cell 1DPC spin coated at 6000rpm. (Red) polymerized after after heat treatment. (Green) and at room temperature. The SiO_2 and Nb_2O_5 concentrations were left at 2% and 3% respectively.

Nb_2O_5/SiO_2 one dimensional photonic crystals: flexible phase.

These 1DPCs present a porosity that offers the possibility to build self-standing versatile mirrors, following a standard procedure explained in Chapter 2. In figure 6, an optical characterization of all three stages of the sample, rigid, infiltrated and flexible phase are shown.

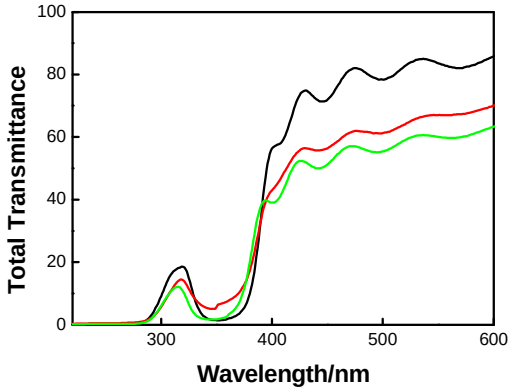

Figure 6: UV-Vis characterization of all the stages of the sample: pre-infiltrated (Black), infiltrated (Red) and flexible film (Green).

The total transmittance spectra reveals a Bragg peak with a maximum of intensity in all three stages of the sample, i.e before, after infiltration, and flexible phase. In figure 7 we can see a digital image of a SiO_2/Nb_2O_5 flexible 1DPC, lifted off from the crystal substrate, were it was originally deposited.

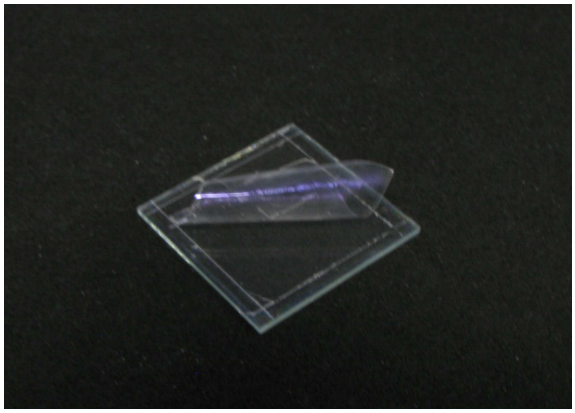

Figure 7: Image of a flexible one dimensional photonic crystal made of SiO_2 and Nb_2O_5 nanoparticles.

ZrO_2/SiO_2 one dimensional photonic crystals: rigid phase.

1DPCs made with SiO2 and ZrO2 nanoparticles as building blocks were made following the same route used for SiO_2/Nb_2O_5 1DPCs. Important parameters of the resulting Bragg peak were obtained after fitting the reflectance spectra with a code based on a transfer matrix formalism as explained previously in this chapter. An example of the performed simulations can be seen in Figure 8, from which we extract n_{ZrO2}=1.70 and n_{SiO2}=1.32, values that imply a pore volume fraction of 50% and 25% respectively. Values of 2.25 and 1.43 are taken for the refractive indexes of bulk ZrO_2 and SiO_2.

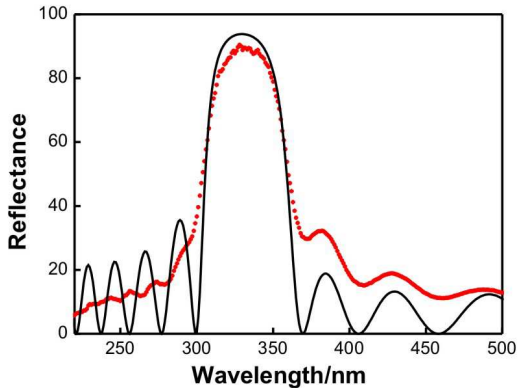

Figure 8: Experimental (Red circle points) and theoretical (Black solid line) reflectance spectra of a 10 (SiO_2/ZrO_2) multilayer system.

FESEM images of the cross sections of a SiO_2/ZrO_2 multilayer, obtained with secondary and backscattered electrons, are shown in Figure 9a and Figure 9b, respectively. Secondary electron image reveals a periodic structure in which the spherical morphology of the bigger SiO_2 particles can be recognized, while the layers made of the smaller ZrO_2 particles appears as an almost continuous layer. Backscattered electron images taken from the same sample region disclose clearly the continuous and smooth interfaces between consecutive layers, brighter fringes corresponding to denser ZrO_2 layers.

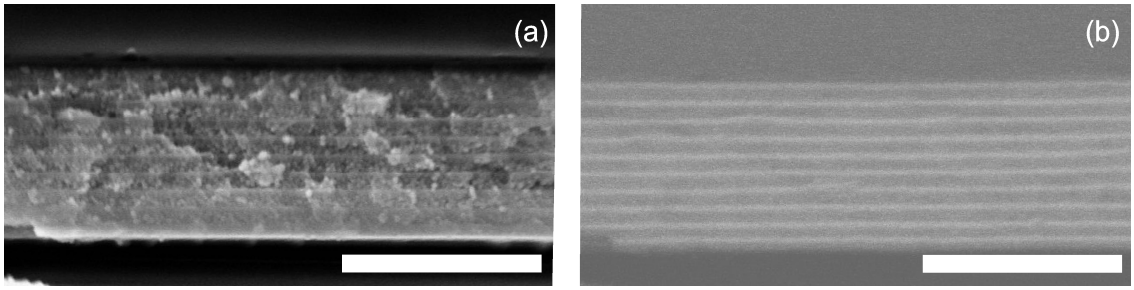

Figure 9: FESEM images of the same region of the cross section of a 20 layer SiO2/ZrO2 1DPC deposited onto a silicon substrate, obtained using (a) secondary and (b) backscattered electron detection. Scale bar is 1 µm in both figures.

The particular surface interaction between SiO_2 particles and dialyzed ZrO_2 ones seem to favor the formation of thicker film piles at room temperature, which is turn convenient for the preparation of flexible films from them (vide infra). Detailed studies on the mechanical stability of colloidal assemblies propose that particles are likely to be held together by bridges of water hydrogen bonded to the surface, which act as a cement for the structure.[11]This image reveals also the presence of interpenetration in the layers, that negatively influences the refractive index contrast and hence the intensity of Bragg reflections from the structure. However, these Bragg stacks are able to reach intensities close to 100% at 300nm, given its high structural quality and also the high number of layers stacked, in our case, 26 layers were piled up without heat treatment in the process, to reach close to 100% reflectance in the as deposited sample, as can be seen in figure 10.

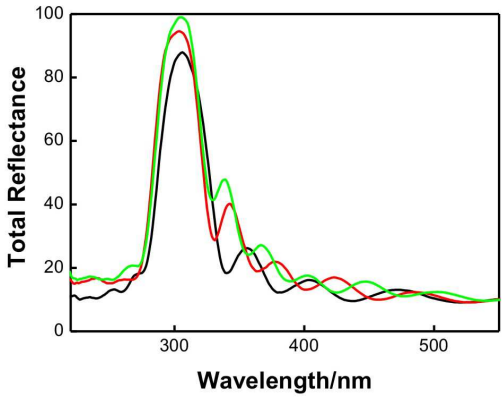

Figure 10: Total reflectance spectra obtained from ZrO_2/SiO_2 multilayers. Spectra were recorded after the deposition of 20 (Black), 22 (Red) and 26 (Green) layers, as indicated in the graph.

The method herein proposed allows locating this maximum at different UV wavelength ranges, as illustrated by the series of total reflectance (R_T) spectra plotted in Figure 11a. These have been measured from a set of porous ZrO_2/SiO_2 1DPC deposited on a quartz substrate at different final rotation speeds or using different particle concentrations in the precursor suspensions. Complementarily, we measure the total transmittance (T_T) spectra of the coatings, which are

shown in Figure 11b. It is clearly observed that samples can be designed to reflect well-defined spectral ranges in different sub-regions of the ultraviolet spectrum, namely, UVA, UVB and the less energetic part of UVC (from 280nm to 220nm). Significant peak intensity (80%) and width ($\Delta\lambda$=50 nm, 0.68eV) are attained for the number of unit cells (N=12, a unit cell being defined as a SiO_2 /ZrO_2 bilayer) herein stacked as a consequence of the high refractive index contrast between the SiO_2 and ZrO_2 layers. An estimation of these values is obtained from the fitting of the optical response, as shown below. Most of the samples absorbs near 50% of incident light at λ =220nm (5.63 eV), as a consequence of interband absorption in ZrO_2 layers, shown in Figure 11c.

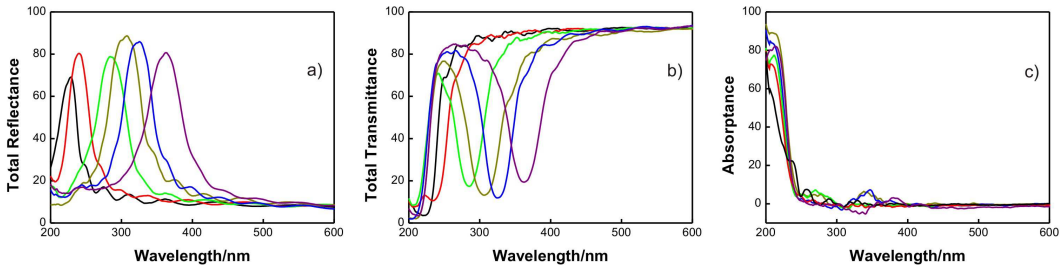

Figure 11: (a) Total reflectance, (b) total transmittance and (c) absorptance from ZrO_2/SiO_2 interference films. All films were deposited using the same spin coating protocol (ω=6000 rpm and γ = 11500 rpm/s) but different nanoparticle concentrations (expressed as [SiO_2 % wt., ZrO_2 % wt.]): [1.0, 2.5] (Black); [1.5, 2.5] (Red); [2.0, 2.5] (Green); [2.25, 2.5] (Dark Yellow); [2.25, 3.0] (Blue), [2.5, 3.0] (Purple). Unit cell thicknesses are 75 nm, 80 nm, 95 nm, 105 nm, 110 nm and 125 nm, respectively.

It can be observed also that, as the position of the Bragg peak shifts to lower wavelength, some overlap with the absorption starts to be significant, which distorts the reflectance and the transmittance spectra for λ<220 nm. The detected fluctuations in absorptance under 3% at longer wavelengths are due to geometrical restrictions to full solid angle light detection in the integrating sphere.[12] This analysis reveals that the UV shield effect, plotted as transmittance in Figure 11b, is totally due to reflection by the film. In addition, the transparency of the samples in the visible region (390 nm-750 nm), estimated using standard procedures (ISO 9050:2003), is around 90% in all cases. In line or ballistic transmission measurements were also performed and compared to total transmission ones in order to evaluate the amount of light deflected from the incident beam by effect of imperfections in the sample. Results are presented in Figure 12. From them we can conclude that the density of optical defects has an almost imperceptible effect on the optical quality of the coating.

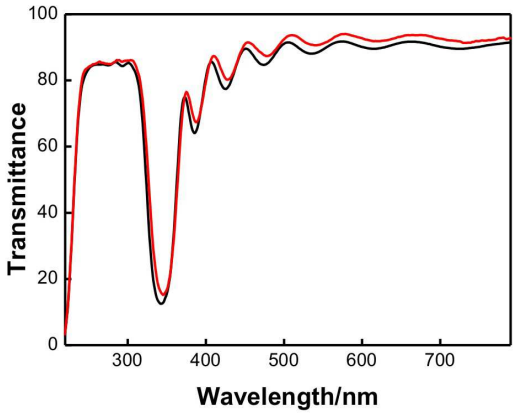

Figure 12: Ballistic (Red) and total (Black) transmittance spectra obtained from a ZrO_2/SiO_2 multilayer system made of 11 unit cells.

In order to obtain an optical porous resonator, like in the case of the SiO_2/Nb_2O_5 multilayer system, an insertion of a thicker mid-layer of SiO_2 beads was realized. The optical properties of this structure can be visualized in Figures 13a and 13b. In this sample, the transmission window is designed to be near λ=310nm. This type of systems are capable of blocking a wide region of the UV while still transmitting a narrow range of selected wavelengths and can be useful, for instance, to perform a selective photochemical reaction or polymerization of monomers.

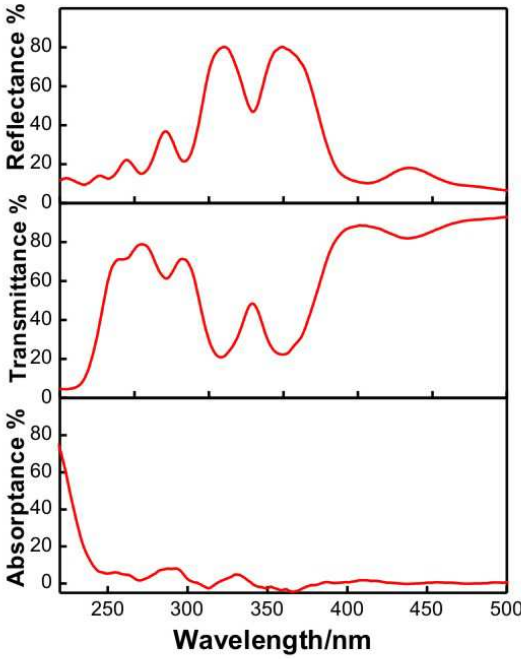

Figure 13: (a) Total reflectance, (b) total transmittance and (c) absorptance from optical resonator built with ZrO_2/SiO_2 nanoparticles.

As shown in the previous section, the absorptance of the resonator shows that all observed optical characteristics in the 250-400nm range are purely due to interference effects.

ZrO_2/SiO_2 one dimensional photonic crystals: infiltrated phase.

Since the SiO_2/ZrO_2 multilayer systems present a porous nature similar to that of Nb_2O_5 and related to the nanoparticulated layers they are also susceptible to be infiltrated with polymeric compounds to attain a hybrid coating that can eventually be lifted off and behave as a self-standing selective UV protecting film. The effect of the polymerization temperature of PDMS in the infiltrated samples on their optical performance is illustrated in Figures 14a and 14b. At first sight, we see that when this process occurs at room temperature, it results in a red shift. However, in the SiO_2/ZrO_2 system, due to a different arrangement in the packaging of the nanoparticles, it has less mobility of the infiltrating agent in the structure. This can cause solvent retention, and after a thermal treatment is performed, the evaporation of the solvent can cause a slight reduction in the thickness of the sample and thus, a blue shift in the Bragg peak position. This hypothesis is supported by the fact that at higher PDMS polymerization temperatures (from 110ºC to temperatures close to 300ºC) the Bragg peak shifts to lower wavelengths. This hybrid system is thermally stable until 300ºC, above that temperature, the PDMS starts to decompose.

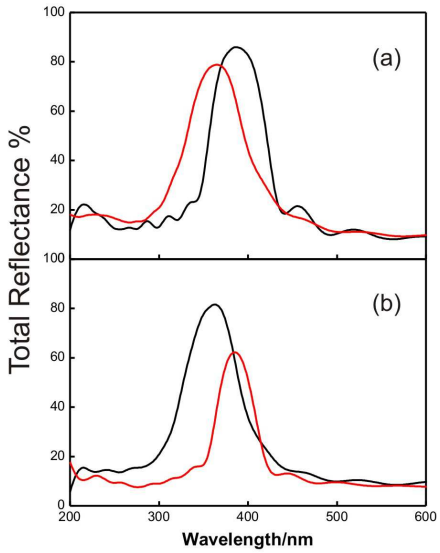

Figure 14: (a) Total reflectance spectra of a 16 layer SiO_2/ZrO_2 1DPC in rigid phase (Black) and infiltrated and polymerized at 110ºC (Red). (b) Total reflectance spectra of a 16 layer SiO_2/ZrO_2 1DPC in rigid phase (Black) and infiltrated and polymerized at room temperature (Red).

ZrO_2/SiO_2 one dimensional photonic crystals: flexible phase.

A challenge to successfully achieve our goal was the very small average pore size present in ZrO_2 layers due to the small particle size of the zro2 particles. That feature could inhibit the diffusion of the oligomers to the deepest layers of the photonic structure. To overcome this obstacle, we infiltrated the structure by spin coating, which forces the deposited liquid phase to enter the voids of the porous multilayer now used as substrate. Later on, the sample was left for one day before starting the thermal polymerization, in order to allow the whole structure to be

infiltrated with the polymer. Once the sample is polymerized, the rest of the process to obtain a flexible film is carried out following the procedure explained in chapter 2.

In Figure 15a we show reflectance spectra for seven flexible ZrO_2/SiO_2 photonic crystals of different lattice constant. These data were obtained with 13 unit cells samples , to reach the maximum of intensity at different spectral positions. The Bragg peak intensity decreases after PDMS infiltration and lifting off, being comprised in the range between 60% and 80% in all cases. The decrease in reflectance is due to the lowering of the refractive index contrast between SiO_2 and ZrO_2 layers upon filling of the polymer. These new hybrid polymer/metal oxide samples are very transparent, mechanically stable and highly flexible, as the images displayed in Figure 15b demonstrate.

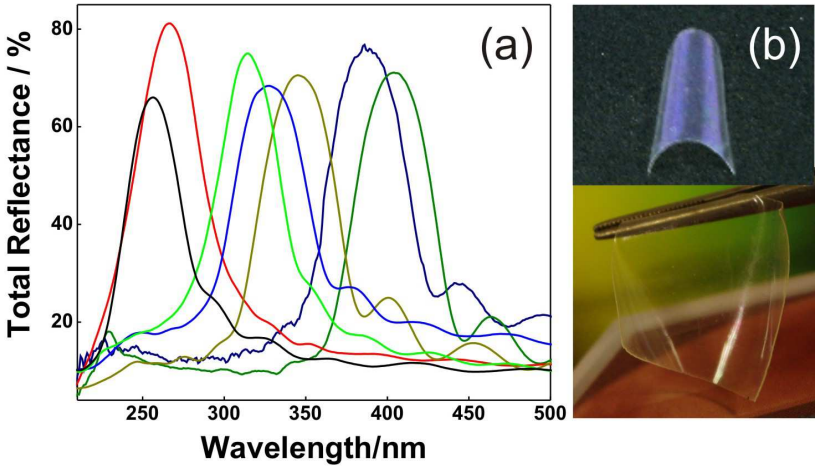

Figure 15: (a) Total reflectance spectra of individual flexible hybrid ZrO_2/SiO_2 photonic crystals. (b) Photographs of hybrid self-standing PDMS/ZrO_2/SiO_2 multilayer film.

Stacks of hybrid flexible SiO_2/ZrO_2 films

The mechanical stability and flexibility of films of different lattice constant that shield against well-defined wavelength regions along the 200 nm-400 nm range, as shown in Figure 15, open the way to block selectively wide spectral regions by piling them up. In Figure 16 we show the reflectance spectra of a series of flexible stacks made of an increasing number of multilayers, each one displaying its characteristic Bragg peak at different UV spectral range. Total reflectance, total transmittance and absorptance for stacks containing 1, 2, 3, 5 and 7 films are shown in Figure 16. Films were attached sequentially, starting from the one that reflects the shortest wavelengths up to the one reflecting closer to the blue region. As the number of flexible films increases, a wider spectral range is reflected, the entire UVC-UVB-UVA range is efficiently reflected, maintaining a transparency of 60% in the visible region.

This lowering in transparency is due to the scattering by irregularities in the interfaces between the films put in contact. Since multilayers are embedded in a thick PDMS matrix, interference effects between the different films are not detected in the optical properties of the multilayer

pile. From the point of view of radiation protection, this simple method can be used to selectively shield against a spectral region of interest, as well as to mimic or surpass the effect of a conventional UV absorbing material, as shown in the next section.

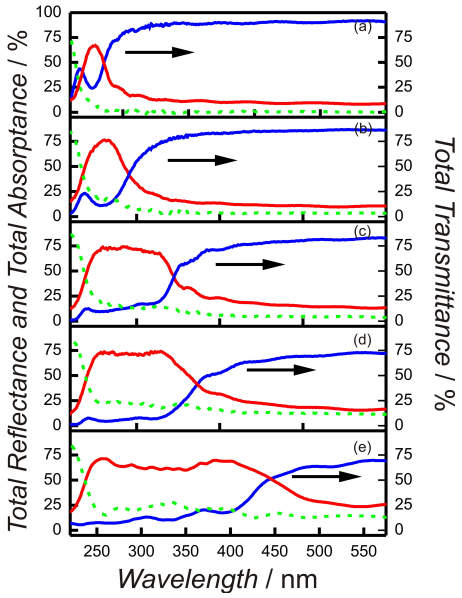

Figure 16: Total reflectance (red line), total transmittance (blue line) and absorptance (estimated as $1\text{-}R_T\text{-}T_T$, red dotted line) spectra of different stacks of the flexible multilayer containing films shown in figure 4a. The number of samples piled up is: (a) 1, (b) 2, (c) 3, (d) 5, and (e) 7.

Also, it was necessary to test the optical response of these systems composed of flexible films when facing angular radiation. UV shielding systems based in organic or inorganic compounds whose protection mechanism is relies in absorption, are independent of the angle of incident light. It is known from introduction that a variation of the angle causes a blue shift in the Bragg peak position. However, we can see from Figure 17 that the variation of the Bragg peak from 0º to 50º is less than 30nm. The measure was carried out with the sample placed on a rotating stage in a ballistic transmittance set up. This result indicates us that the UV protecting efficiency of a tandem similar to the ones shown in Figure 16 is not affected by a drastic change in the angle of incidence.

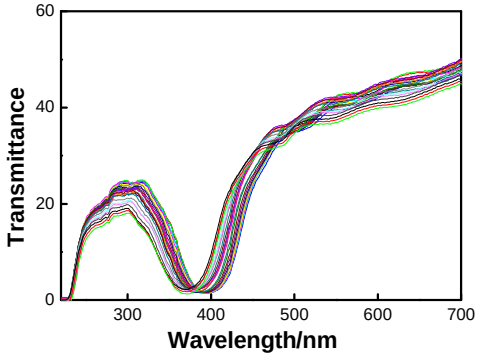

Figure 17: Transmittance measured for a series of flexible films with the Bragg peak in the UVA spectral region. Measures were taken from 0º to 50º, varying 2º from one spectrum to the next one.

Radiation Protection

The ability of the SiO_2/ZrO_2 flexible photonic crystal films and stacks of them to protect from UV light was tested by exposing commercial UV sensitive strips (*Control Cure, UV FastCheck Strips, UV process supply Inc.*) to the collimated and uniform radiation beam coming out from a solar simulator, employing different combinations of PDMS embedded multilayers to shield them against it. Detailed analysis of the color changes induced in the strips by effect of the exposure to UV light allows us quantifying the amount of energy they have received from the solar simulator. Both naked strips or PDMS film covered ones were used to determine the relationship between energy density received at the strip surface and the color change observed (see Figure 18).

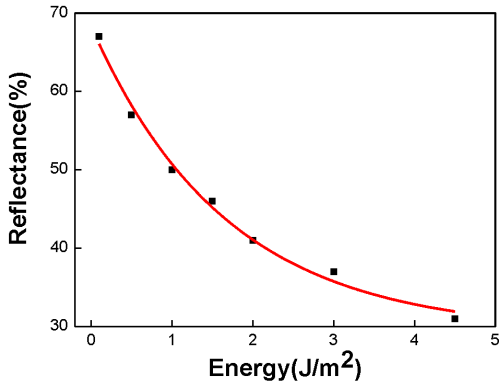

Figure 18: Reflectance of a UV sensitive strip film as function of the energy received per unit area under 1 sun illumination intensity from a solar simulator.

The energy received per unit area was quantified by measuring the total reflectance of the strips in an integrating sphere. In order to ensure the reproducibility of the protection effect, irradiation experiments were repeated three times and the results averaged. The performance of the ZrO_2/SiO_2 interference mirrors as UV shields was compared to that of PDMS flexible films, in one case embedding TiO_2 nanoparticles, and, in the other, supporting a thin film of benzophenone-3, an organic molecule that is included as UV protecting agent in sun screen lotions.[13] In both cases, UV light blocking occurs only as a consequence of absorption, since the TiO_2 particles employed are too small to give rise to diffuse scattering.

UV sensitive strips were placed below different types of UV protecting films and then illuminated at 1 sun light intensity (AM1.5, 1000W/m^2) during the same time. Films tested were: 1) A stack of multilayers that blocks the full UV region (sample ML_A); 2) another Bragg mirror pile that mimics the absorption profile of TiO_2 (sample ML_B); 3) A PDMS film containing a layer of TiO_2 nanoparticles with the same thickness than the photonic cystal (approximately 1 µm); 4) A PDMS film onto which a thin layer of benzophenone-3 was deposited; 5) a PDMS film, to quantify the effect of receiving this amount of radiation without

protection. In Figure 19a we show the energy per unit area received by the strips in each case. The corresponding transmittance spectra are plotted in Figure 19b.

Remarkably the ability of the flexible interference mirror tandem ML_B to shield against UV rays is as good as that of a similar film of highly absorbing TiO_2 particles, while the performance of ML_A surpasses that of the film onto which benzophenone-3 was deposited. This shows that flexible photonic materials are suitable substitutes of inorganic or organic UV absorbers traditionally employed to dope polymers to the same end. Please notice that the expected downshift of the spectral position of the reflectance peak for oblique angles of light incidence on multilayers, which follows a combination of Bragg and Snell laws, is in our case easily compensated by designing a stack of multilayers for which the longer cut-off wavelength is approximately 30 nm above the lower energy edge of the range to be blocked, since that is the peak shift measured at 45º.

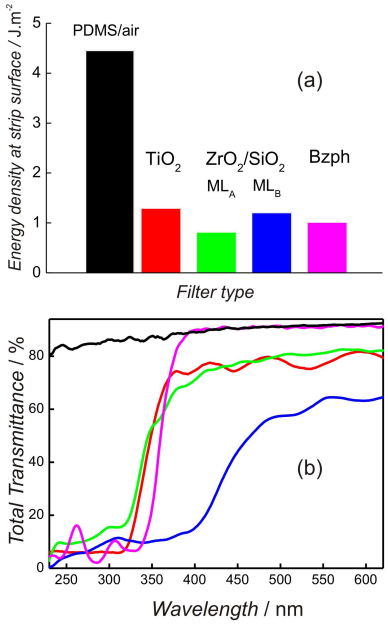

Figure 19: (a) Energy density received at the surface of UV sensitive strips covered with different flexible UV protective films and exposed to a solar simulator (AM 1.5 spectrum, 100 mW/cm^2). Height of the bar represents the average value and the black line represents the standard deviation. ML_A and ML_B stands for different ZrO_2/SiO_2 film stacks. (b) Total transmittance spectra of the protecting films used in Figure 6a: pure PDMS or naked strip (black line), TiO_2 nanoparticle film embedded in PDMS (red line), benzophenone-3 deposited (violet line) onto PDMS, ML_A (green line), and ML_B (blue line).

Conclusions

I have shown a method to prepare both rigid coatings and flexible self-standing films capable of efficiently protecting against UV radiation in desired and preselected wavelength ranges. The UV blocking effect arises exclusively from optical interference phenomena and depends only on the number of stacked layers and the refractive index contrast between them. I demonstrate that these films may equal or outperform layers of similar thickness made of purely absorbing

materials in terms of the degree of radiation protection achieved. These new materials offer a degree of protection comparable to that of traditional ones, but without any foreseeable unwanted secondary effects, such as photodegradation, increase of local temperature or, as it is the case for organic absorbers, generation of free radicals, all of them caused by light absorption.

References

[1] Calvo, M.E.; Míguez, H. *Chem. Mater.*, **2010**, 22, 3909–3915.

[2] Castro Smirnov, J.R.; Calvo, M.E.; Míguez, H. *Adv. Funct. Mater.*, **2013**, 23, 2805–2811.

[3] Hulst, H.C.v.d., *Light Scattering by Small Particles*, **1981**, New York: Dover.

[4] Calvo, M.E.; Colodrero, S.; Hidalgo, N.; Lozano, G.; Lopez-Lopez, C.; Sanchez-Sobrado, O.; Mıguez, H. *Energy Environ. Sci.*, **2011**, 4, 4800.

[5] Lozano, G.; Colodrero, S.; Caulier, O.; Calvo, M.E.; Míguez, H. *J. Phys. Chem. C*, **2010** , *114* , 3681 .

[6] a)Wu, Z.; Lee, D.; Rubner, M.F.; Cohen, R.E. *Small* 2007, **3**, 1445-1451. (b) Bonifacio, L.D.; Lotsch, B.V.; Puzzo, D.P.; Scotognella, F.; Ozin, G.A. *Adv. Mater.* 2009, **21**, 1641-1646

[7] Prosser, J.H.; Brugarolas, T.; Lee, S.; Nolte, A.J.; Lee, D. *Nano Lett.* **2012** , *12* , 5287 .

[8] Lin, V.S.Y.; Motesharei, K.; Dancil, K.P.S.; Sailor, M.J.; Ghadiri, M.R. *Science*, **1997** , 278 , 840 .

[9] Steele, J.J.; Popta, A.C.; Hawkeye, M.M.; Sit, J.C.; Brett, M.J. *Sens. Actuators B,* **2006** , 120 , 213 .

[10] Hidalgo, N.; Calvo, M.E.; Bellino, M.G.; Soler-Illia, G.J.A.A.; Míguez, H. *Adv. Funct. Mater.*, **2011**, 21, 2534–2540.

[11] Gallego-Gómez, F.; Morales-Flórez, V.; Blanco, A.;de la Rosa-Fox, N.; López, C. *Nano Lett.* **2012** , *12* , 4920 .

[12] Sánchez-Sobrado, O.; Lozano, G.; Calvo, M.E.; Sánchez-Iglesias, A.; Liz-Marzán, L.M.; Míguez, H. *Adv. Mater*. **2011**, *23*, 2108

[13] Cole, C.A.; Vollhardt, J.; Mendrok, C. *Clinical Guide to Sunscreens and Photoprotection* , (Eds: H. W. Lim , Z. D. Draelos), Informa-Healthcare USA Inc., New York, **2009**, 39 – 51.

Chapter 4

Biocompatible films with tailored spectral response for DNA damage prevention of skin cells

Introduction

In the previous chapter, it was shown that flexible PDMS films embedding nanoparticle multilayer structures behave as strong reflectors in the UV range. This feature opened the possibility to develop novel adaptable materials for UV radiation applications. One of the functionalities we foresee to these materials, knowing that they are biocompatible and can be easily adapted to a random surface, is the protection of the skin.

Exposure to UV radiation, for instance solar UV radiation, presents a risk owing to its strong genotoxicity for the skin[1]. Solar UV radiation is one of the main causes for erythema, a disease that has been used as a standardized index to estimate the risk of UV radiation for human skin. UV radiation yields its genotoxicity by supplying the skin genome with the required photochemical energy to produce specific DNA damage[2] leading to genomic anomalies, for example mutations[3] that are able to induce skin cancer.[4]

Very recently, Ikehata et al,[5] demonstrated the wavelength dependence of the genotoxic and erythematic effects of UV radiation over the skin. They analyzed the induction kinetics of mutation and inflammation in mouse skin using lacZ transgenic mice with monochromatic UV radiation sources. The dose–response kinetics of mutation induction in the epidermis and dermis of mouse skin was examined in wavelength points in the range of 260–364 nm by irradiation

with high-intensity monochromatic UV radiation. The most significant finding is the fact that the response was wavelength dependent, showing a peak at around 310–320 nm. The wavelength dependence for plateau mutant frequency values, defined as the suppressed values by the mutation induction suppression (MIS) effect to a constant plateau level of 2 or 3 fold higher than the background mutant frequency, can be seen in Figure 1.

It is the purpose in this chapter, to build flexible stacks combining different periodicities whose reflectance maximum matched the mentioned *in vivo* action spectrum of the genotoxic and erythematic effect of UV on skin cells. This material, that prevents DNA damage when used as UV shields, was created with the objective of being used afterwards in skin UV protection related applications.

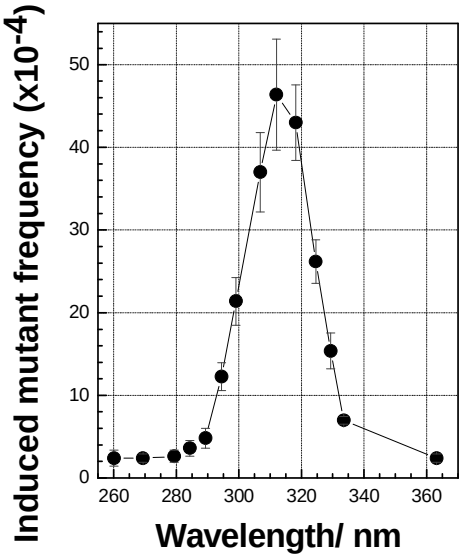

Figure 1: Wavelength dependent change of UV radiation genotoxicity in the skin for the plateau mutant frequency values(circles).

Also, an analysis of the degree of damage caused on DNA of different epithelial cells by a broad band UV source when protected by the flexible Bragg stack was realized, demonstrating that these films are capable of shielding as effectively as UV absorbing compounds embedded in similar polymer matrices. This constitutes, as far as I know, the first experimental evidence of protection of epithelial cells by a biocompatible flexible film, judiciously designed to shield specifically against a highly genotoxic UV range, in which no absorption occurs, hence discarding all secondary effects.

Nanostructured UV filters for preselected ranges

In chapter 3 it was shown that the combination of films can block UV light at different wavelengths. A total number of seven films were piled to cover a wide UV spectral region. In

the present chapter, I will show that it is possible to combine a less number of films to protect against a well-defined genotoxic action spectrum preserving the optical transparency. I will demonstrate that it is possible to block UVB light by reflection combining optical filters made of nanoparticles that absorb in the UVB region of the spectrum.

Experimental section

Cell Culture

The human SB2 cell line was isolated from a human primary cutaneous lesion[6] and kindly provided by Dr. Menashe Bar-Eli (M.D. Anderson Cancer Center, Houston, TX, USA).[7] Cells were maintained in a monolayer culture in 95% air/5% CO2 at 37ºC in Dulbecco's modified Eagle's medium (DMEM) supplemented with 10% FBS and 1 % (v/v) Penicillin–Streptomycin–Glutamine (10,000 units/mL penicillin G sodium, 10,000 µg/mL streptomycin sulphate and 200 mM L-glutamine) (Gibco). Cells were passaged at 80-90% confluency and cultured for less than 10 passages: The culture medium was aspirated and the cells were washed twice with sterile phosphate-buffered saline (PBS) and once with Trypsin–EDTA solution (Biocrom). Following this, cells were incubated with sterile Trypsin–EDTA solution until detachment and the trypsinised cells were used to seed the experiments the day before the UVB irradiation in a 96 MW-plate at 60% confluency.

UVB Irradiation

The procedure of Schwarz et al.[10] and Huynh et al.[11] was used to irradiate the SB2 cells. They were seeded the day before the irradiation as previously described. Medium was removed and monolayers were washed twice with PBS to avoid the photosensitization effect of components in culture medium and then they were overlayed with PBS. Cells were exposed at a distance of 23 cm to a radiation source using a UV lamp (450W OF Xenon Lamp, Dichroic Mirror Newport cat.#66226, Arc Lamp Housing, Newport cat.#66920, Oriel Instruments, USA). Neutral filters were used in order to adjust the resulting irradiance. The variation in the output (mW/cm^2) radiation of the UV lamp was measured using a relevant UV detector (UVA or UVB) attached to a photometer (Solar Light company Inc. USA). Cells were then placed, without the petri dish lid, under the light beam with or without the appropriate filters. For different doses of irradiation (200 and 1000 J/m^2), cells were exposed to different durations. After irradiation, complete medium was added to cells. Non-irradiated control cells (NI) were managed in the same manner, except that they were not exposed to UVB light.

Detection of CPD generation in DNA

Cyclobutane pyrimidine dimers (CPD) were evaluated with an OxiSelect™ Cellular UV-Induced DNA Damage Staining Kit (Cell Biolabs Inc, USA), according to the manufacturer's instructions. Briefly, after 15 hours of UVB radiation recovery, cells were fixed, denaturized, and incubated with an anti-CPD antibody, followed by a FITC conjugated secondary antibody. The unbound secondary antibody was removed during washing steps. Negative controls were performed with the FITC conjugated secondary antibody and with no antibodies to set up background fluorescence. After CPD staining, nuclei were stained with Hoechst 33342 as previously described. Images of cells were acquired with an automated microscope-based High Content Screening System (HCS), Operetta®. Data was analyzed by Harmony® High Content Imaging and Analysis Software (Perkin-Elmer Inc.).

Statistical analysis

Irradiation with and without filters was made by triplicate. Four wells of cells were irradiated each time to obtain data by quadruplicate in every irradiation. The statistical descriptive representation of data is presented as box-plots where the distribution of data is shown by the Q1 (25%), Q2 (50%), Q3 (75%) quartiles, atypical (bars) and outlier values (numbered white circles). Parametric or non parametric distribution of data was analyzed by the Shapiro-Wilk test and Mann-Whitney test for no parametric independent samples was applied to calculate the statistical significance of data. Statistical analysis was performed with R Software 3.0.

Materials preparation and characterization

For the potential applications in skin protection pursued, we prepare 1DPC by piling up alternately layers of SiO_2 and either ZrO_2 or TiO_2 nanoparticles, whose thicknesses are controlled to yield the desired UV reflecting properties. The flexible versions of these coatings are obtained following the technique explained in the previous chapters.[8] The method hereby employed allows us preparing films with homogeneous structure in relatively large areas (4cmx4cm). In Figure 2a I show a picture of a flexible SiO_2/ZrO_2 1DPC that will be used for the UVB filters as will be shown in this chapter. The microstructure of these films can be observed in the FESEM cross section image displayed in Figure 2.b, where uniformity and smooth interfaces between nanoparticle layers can be appreciated. Left and right pictures correspond to secondary and backscattered electron images respectively. In the former, some morphological features of the multilayer can be distinguished (i.e. the spherical shape of SiO_2 nanoparticles), while the latter reveals how defined the interfaces between layers.

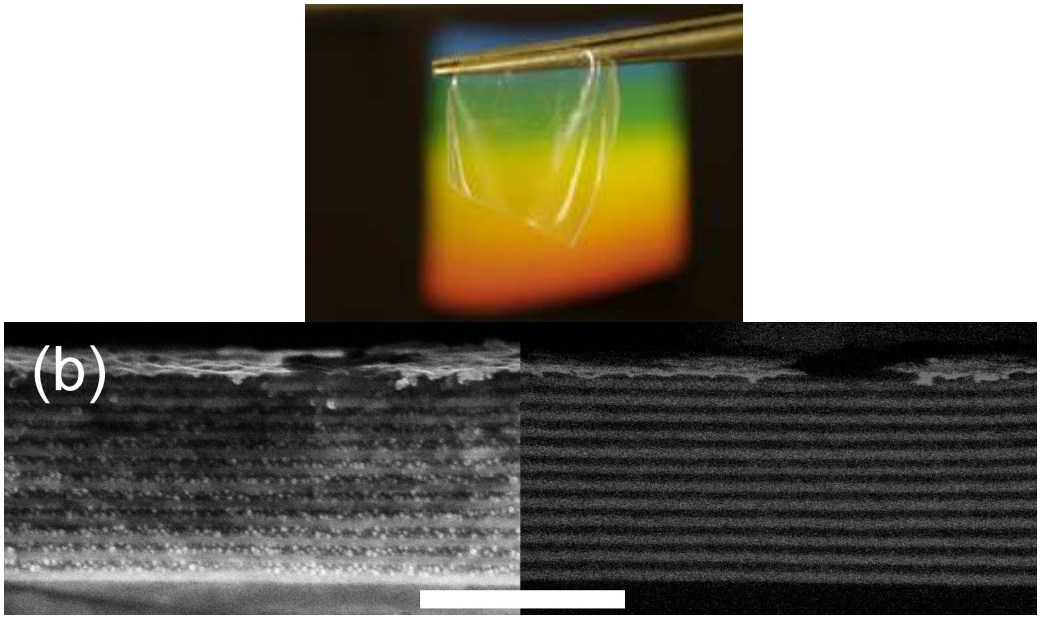

Figure 2: (a) Photograph of a 24 layer self-standing SiO_2/ZrO_2 1DPC. (b) FESEM cross section image of the same sample obtained using secondary (left) and backscattered electron detection (right). Scale bar is 1 μm.

A filter, labelled as ZST-3 and developed to block the targeted wavelength range, was made by stacking two ZrO_2/SiO_2 1DPCfilms on top of a TiO_2/SiO_2 1DPC film (See Figure 3).

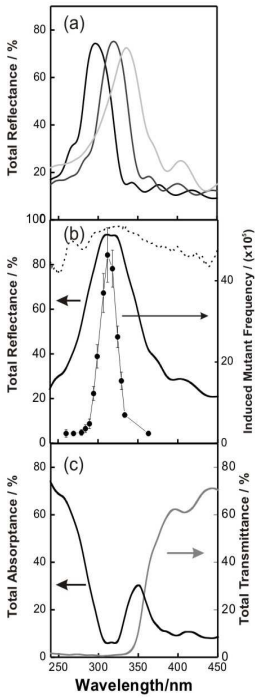

Figure 3: a) Total reflectance spectrum of each one of the three films that constitutes the ZST-3 film. (b) Total reflectance spectrum of the ZST-3 film (left y-axis). The action spectrum of the induced mutant frequency is also plotted (right y-axis) (adapted from ref. 4). Superimposed to both spectra, we plot the spectral irradiance of the lamp in arbitrary units (dashed line) (c) Total absorptance and total transmittance of the ZST-3 film.

A good match between the reflectance primary maximum and the targeted action spectrum, i.e., the skin cell genotoxic spectrum reported by Ikehata (plotted with a dashed line in Figure 3(b)), is observed. Please notice that even when the filter contains TiO_2 nanoparticles that absorb UVB radiation, as it the case of ZST-3, interference effects prevail over absorption as UVB blocking mechanism, as it can be seen in Figure 3b. In order to ensure that UVB blocking comes mainly from interference effects, the TiO_2/SiO_2 multilayer is placed below the ZrO_2/SiO_2 films in charge of reflecting intensely wavelengths lower than 330nm. A scheme of this configuration can be seen in Figure 4.

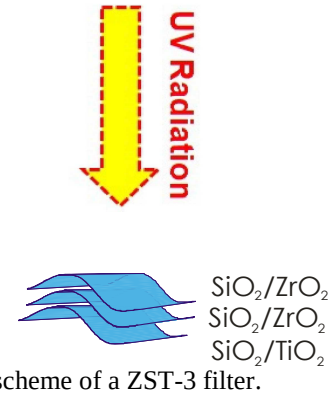

Figure 4: Protection configuration scheme of a ZST-3 filter.

For the sake of comparison, a flexible film of PDMS containing exclusively TiO_2 nanoparticles, labeled as T-1, was prepared, as can be seen in Figure 5.

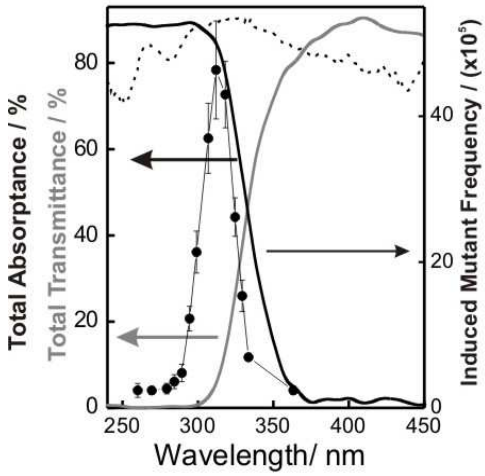

Figure 5: Total absorptance (black solid line) and total transmittance (grey solid line) of the T-1 film. The action spectrum of the induced mutant frequency is also plotted (right y-axis) (adapted from ref. 4). Superimposed the spectral irradiance of the lamp in arbitrary units (dashed line) is plotted

In the T-1 filter, UVB blocking takes place only due to absorption. On the other hand, the ZST-3 film present a much lower absorption in this spectral region but an equally efficient blocking effect, as the transmittance spectra reveal, as a consequence of the strong reflection of UVB wavelengths caused by the nanostructured multilayers embedded within the structure. In order

to take into account the angular dependence of the spectral position, the filter was designed with a wider spectrum than the action spectrum of the genotoxicity to ensure that the protection also works when the incident radiation is not perpendicular to the surface of the films.

Damage on the DNA in different types of epithelial cells covered with UV protecting films

The capability of these stacks to protect against the genotoxic effects of UV radiation was tested in the group of Guillermo de la Cueva in BIONAND, Malaga, by exposing a series of human skin cell cultures to a broad band UV light source. More specifically, UV induced cell damage of human SB2 melanoma cell line was analyzed at the molecular level by cyclobutane pyrimidine dimers (CPDs) detection in the cell DNA and at the phenotypic level by quantification of the cell death rate after UV exposure (by measuring the so called *apoptotic* rate[9]). CPDs are the most predominant pre-mutagenic DNA-lesions produced by UV radiation in human skin cells.[10-12] Therefore, we used this alteration to determine DNA damage in a first stage.

A well-established procedure, as described by Schwarz et al.[13] and Huynh et al.,[14] was used to irradiate the SB2 cells. Full details of the cultures preparation are provided in the experimental section. Cells were exposed to 200 J/m^2 by placing them at a distance of 23 cm from the UV radiation source. Non-irradiated cells were managed in the same manner, except that they were not exposed to UV light.

In Figure 6, images of the nuclei of irradiated cells are shown. CPD positive inmunostaining (green signal) was observed in the nuclei (blue signal) of irradiated cells when no filter (Figure 6a) or the control filter (Figure 6b, labeled as Ctrl) were used. A film made of PDMS without any content of nanoparticles was used as control filter. On the other hand, no CPD signal was detected in irradiated cells protected by highly absorbing T-1 films containing TiO_2 nanoparticles (Figure 6c), which we used as a reference, or by the absorption free and highly reflecting ZST-3 film containing nanoparticle multilayers.

CPD inmunostaining analysis demonstrated that the UV reflection mechanism of the flexible multilayered films efficiently prevented the appearance of DNA lesions. When these lesions appear, the cells arrest proliferation and activate the repair mechanism. If they succeed, the cell cycle will be restored and proliferation resumed. On the contrary, if they do not succeed, programmed cell death will be activated. There is a correlation between the UV dose and the ability of cells to repair their DNA. The highest the UV dose, the more difficult for the cells to repair so they activate programmed cell death. Thus, we next asked ourselves if the UV reflection mechanism was efficient to protect cells when the UV dose was high enough to activate programmed cell death after 15 hrs from irradiation.

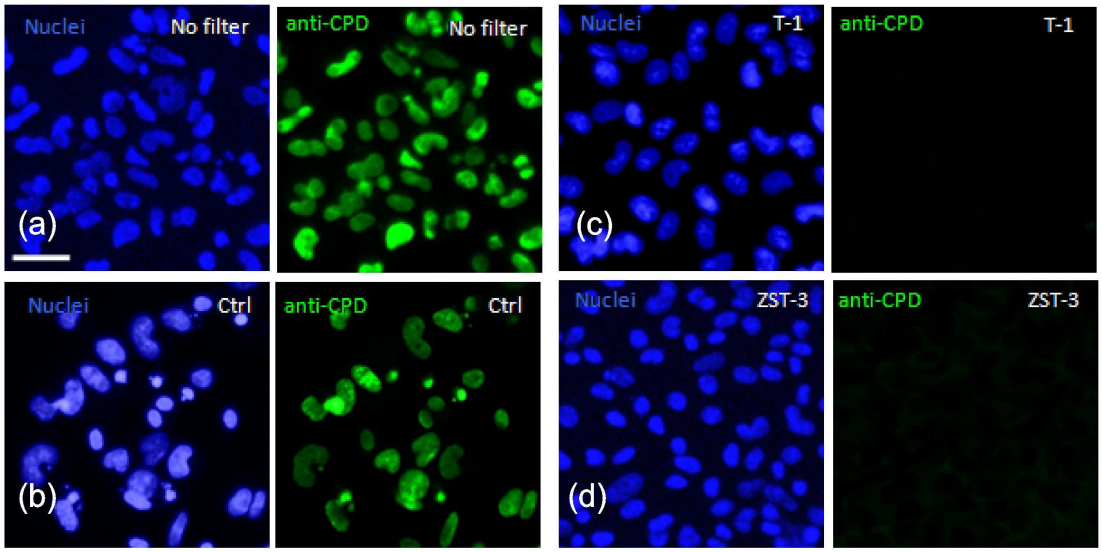

Figure 6: UV-induced DNA damage filter protection on SB2 cell line. CPD positive inmunostaining (green signal) was observed in the nuclei (blue signal) of irradiated cells when (a) no filter or (b) the control filter (Ctrl) was used. No CPD signal was detected in irradiated cells protected by (c) highly absorbing films containing TiO_2 nanoparticles (T-1) or (d) highly reflecting films containing photonic crystal reflectors (ZST-3).

To analyze this, we irradiated cells with 1000 J/m^2 of UV and quantified the number of nuclei that undergo a process known as picnosis (please see Figure 7a). Picnosis (from Greek *pyknono* meaning "to thicken up, to close or to condense"[15]) is a morphologic feature of a specific form of cell death known as apoptosis and is commonly used to evaluate the the damage caused by cell exposure to UV light. We showed that irradiation of SB2 cells lead to a 11,9 % (median value) of picnotic nuclei while this value decreased to 0.2 % or 0.7 % when cells are protected with the reference T-1 film and the multilayered ZST-3 filter, respectively (Figure 7b). These values were very close or similar to the control value of non-irradiated cells with 0.7 % picnotic nuclei. These results suggest that the UV reflection mechanism is efficient enough to protect cells from a UV dose high enough to activate cell death.

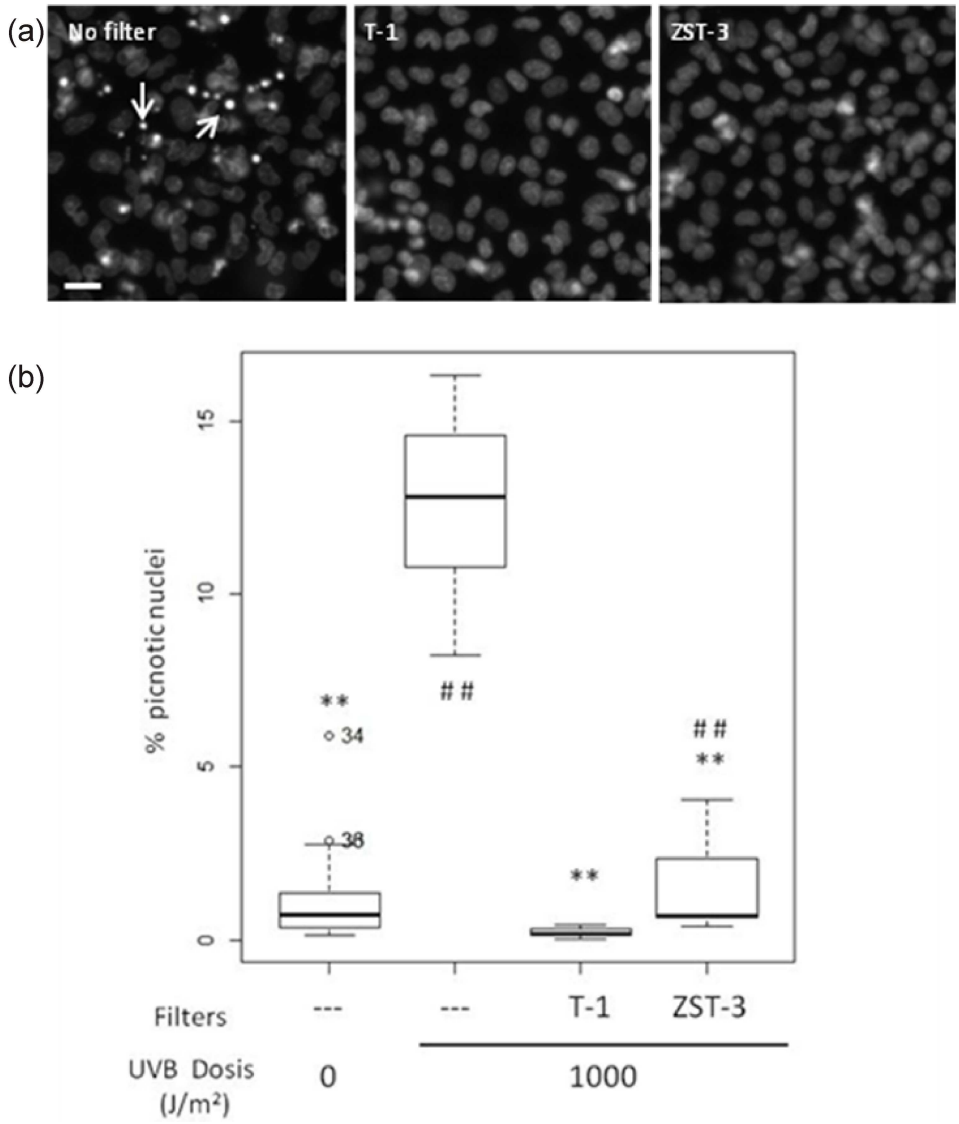

Figure 7: UV induced cell death (apoptosis) in SB2 cell line. (a) Cellular UV induced cell death was analyzed by picnotic nuclei quantification. Picnotic nuclei (white arrows) were identified among the total cell nuclei stained with Hoechst 3342. (b) Box-plot showing quantification of picnotic nuclei after irradiation. T-1 and ZST-3 filters protected from cell death caused by 1000 J/m^2 of UVB. Values show statistical significance (** = p< 0,01, when compared to no filter-1000 J/m^2 and ## = p< 0,01 when compared to T-1 filter).

Conclusions

The results herein presented demonstrate that it is possible to design and realize flexible films capable of efficiently protecting epithelial cells from the UV insult that produces DNA lesions and activates programmed cell death. It was demonstrated that efficient protection is achievable without the need to use photodegradable dyes or absorbing inorganic particles that can degrade the polymer guest matrix. This is, in my opinion, the most important conclusion of our investigations, as it opens the route to new ways of skin shielding against UV based on physical mechanisms previously unexplored for that purpose.

References

[1] Ayala, F.; Palla, M.; Di Trolio, R.; Mozzillo, N.; Ascierto, P.A. *ISRN Dermatology*, **2013**, Volume 2013, Article ID 842359.

[2] Pfeifer, G.P. *Photochemistry and Photobiology*, **1997**,Vol: 65(2):270-283.

[3] Ikehata, H.; Ono, T. *Journal of Radiation Research*, **2011**, Vol: 52(2):115-25.

[4] Wikonkal, N.M.; Brash, D.E. *Journal of Investigative Dermatology Symposium Proceedings*, **1999**, Vol: 4(1):6-10.

[5] Ikehata, H.; Higashi, S.; Nakamura, S.; Daigaku, Y.; Furusawa, Y.; Kamei, Y.; Watanabe, M.; Yamamoto, K.; Hieda, K.; Munakata, N.; Ono, T. *J Invest Dermatol.*, **2013,** 133,7,1850.

[6] Verschraegen, C.E.; Giovanella, B.C.; Mendoza, J.T.; Kozielsky, A.I.; Stehlin, J.S. *Anticancer Res.*, **1991** 529-536.

[7] Singh, R.K.; Gutman, M.; Reich, R.; Bar-Eli, M. *Cancer Res.* **1995**, 55: 3669-74.

[8] Calvo, M.E.; Miguez, H. *Chem. Mater.***2010**, 22, 3909–3915.

[9] Kerr, J.F.; Wyllie, A.H.; Currie, A.R. *Br. J. Cancer* **1972,** *26*, 239.

[10] Mouret, S.; Baudouin, C.; Charveron, M.; Favier, A.; Cadet. J., et al. *Proc Natl Acad Sci U S A.* **2006,** *103*, 13765.

[11] Mouret, S.; Philippe, C.; Gracia-Chantegrel, J.; Banyasz, A.; Karpati, S., et al. *Org Biomol Chem* **2010,** *8*, 1706.

[12] Kraemer, A.; Chen, I.P.; Henning, S.; Faust, A.; Volkmer, B., Atkinson, M.J.; Moertl, S.; Greinert, R. *PLoS One*. **2013**, 8(12), e83392.

[13] Schwarz, T.A.; Gschnait, V.F.; Lugar, T.A. *J. Invest. Dermatol* **1986,** *87*, 289.

[14] Huynh, T.T.; Chan, K.S.; Piva, T.J. *Photodermatol. Photoimmunol. Photomed.* **2009**, 25, 20–2.

[15] Kumar, V.; Abbas, A.; Nelson, F.; Mitchell, R.; Robbins, R. *Basic Pathology (8th ed.):* **2007,** 6, 9. (table 1–1).

Chapter 5

Effect of the spatial modulation of UV induced photochemical effects in the formation of periodic multilayers by collective osmotic shock of block copolymer films

Introduction

In previous chapters, I presented different nanoparticle based photonic crystals that display Bragg peaks in different ranges of the ultraviolet spectrum, acting as selective filters for UV radiation. In this chapter I will analyze the microstructural and optical features of a porous all organic 1DPC with strong reflections in the UV, formed after a series of complex physico-chemical processes in *di*block copolymer film. The resulting polymeric photonic crystal is transparent and presents no absorption in the UVA, UVB and UVC regions of the electromagnetic spectrum. Contrarily to other polymer photonic crystals, where numerous layers had to be deposited to attain the desired optical response,[1-3] only one deposition by spin coating, followed by a simple and fast low temperature procedure are enough to achieve an intense Bragg peak in the UV range. Furthermore, the processing of the system I will present herein is compatible to flexible substrates.

Block copolymers

The case of our study is limited to block copolymers (BCP) and more particularly, *di*block copolymers. A BCP is a type of polymer that combines several types of monomers in the same macromolecule. The association of two covalently bonded copolymers, each one describing

different chemical nature, depending on their position in the polymer chain, gives rise to three configurations of copolymers, as illustrated in Figure 1a: either, alternating, block or statistical copolymers. In a solution or spread in as a thin film, the BCPs are naturally self-organizing networks creating dense nano-objects by a process of micro-phase separation to separate the "blocks".

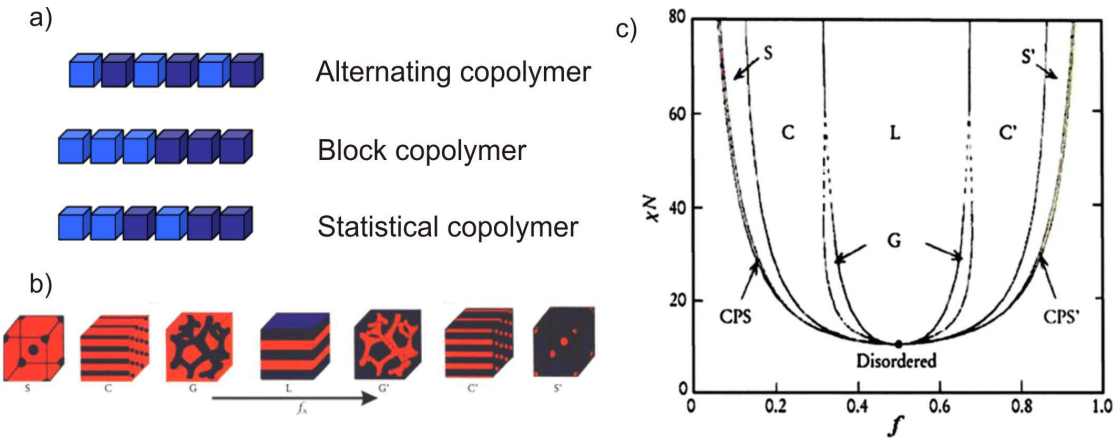

Figure 1: a) Schematic representation of the different configurations of copolymers. b) Diagram of the microdomain morphologies of diblock copolymers. As the volume fraction of components in the diblock copolymer is varied, the diblock copolymer self-assembles into morphologies ranging from spherical (S) to cylindrical (C) to gyroid (G) to lamellar (L). Note that G', C', and S' have the same morphologies but reversed polymer components of the G, C, and S systems. The molecular weight of the block copolymer dictates the size of the microdomains, typically _10 nm. c) Theoretical phase diagram of diblock copolymers in bulk predicted by the self-consistent mean-field theory and the equilibrium morphologies depending on volume fraction (f) of one block to the other and the segregation parameter, χN, where χ represents the Flory–Huggins segment–segment interaction energy and N is the degree of polymerization.

The length of string evolves depending on the polymer concentration and the amount of initiator introduced; the choice of these parameters determines the size of each block. The system characteristics of the diblock copolymer substantially depend on the nature of the constituent chemical monomers. As a result of the low entropy of combination, polymer blends are, in most cases, immiscible and macroscopically phase-separate. When annealing is performed, amorphous block copolymers tend to self-assemble into groups of nanoscopic domains, traditionally called microdomains. The better-known and simplest form of block copolymers is linear diblock copolymers (AB). When the structure presents as constituents two immiscible blocks, A and B, they can assume the following equilibrium micro-phase morphologies ranging from spherical to cylindrical to bicontinuous gyroid to lamellar, as shown in Figure 1b, that can be obtained by varying these parameters.

The self-assembly of BCPs is driven by an unfavorable mixing enthalpy coupled with a small mixing entropy, with the covalent bond connecting the blocks preventing macroscopic phase separation. The microphase separation of diblock copolymers depends on three parameters: (1) the volume fractions of the A and B blocks (f_A and f_B, with $f_A + f_B = 1$), (2) the total degree of polymerization ($N = N_A + N_B$), and (3) the Flory–Huggins interaction parameter (χ_{AB}). The χ_{AB} parameter varies inversely with temperature and specifies the degree of incompatibility between the A and B blocks, which drives the phase separation. The degree of microphase separation of diblocks is determined by the segregation product, $\chi_{AB}N$. The predicted morphologies as a function of volume fraction (f) of one block with respect to the other have been summarized in a theoretical phase diagram shown in Figure 1c.

The complex supramolecular structure of block copolymer (BCP) films and their ease of processing have made these materials interesting candidates to explore new forms of nanolithography.[4-7] Generically, selective dissolution or etching of one of the phases,[8-10] into which a BCP is segregated to form a particular arrangement, is used to attain a nanostructured surface that may be, in turn, employed to pattern other nanomaterials.[11-14]These approaches can be combined with techniques that mold the block copolymer film itself, such as electrically induced patterning,[15] substrate directed self-assembly[16] or nanoimprint lithography. The development of three dimensional porous structures based on BCP has also been investigated.[17,18] In those cases, phase segregation gives rise to two bicontinuous lattices so that one of them can be selectively dissolved to yield a three dimensional open pore network.

Very recently, it was proved that a porous stratified structure can be attained from a block copolymer (BCP) film.[19] It was shown that, in an ordered nanoscale assembly of solute-containing spheres surrounded in a porous matrix, that prevents the diffusion of solute into a surrounding bath of solvent, a large solvent-induced osmotic stresses within the spheres causes a regular series of small explosions within the matrix. The consequential rupture between the spheres would generate a route for the complete release of solute. The process was called collective osmotic shock (COS). A FESEM cross section image of a PS-b-PMMA film with the porous periodical structure is shown in Figure 2.

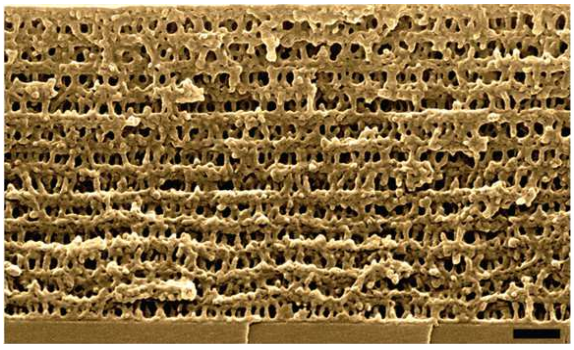

Figure 2: FESEM cross section image of a 82.5 KDa PS-b-PMMA film. Scale bar is 200nm.

In particular, it was demonstrated that a film made of a BCP containing polystyrene (PS) and polymethyl methacrylate (PMMA),in brief (PS-b-PMMA), can be used as starting material to attain ordered porous multilayers. The final structure shows alternate dense and porous layers which endows it with photonic crystal properties, with Bragg reflections in the UV range. However, one striking feature of the periodic layered structures attained by COS is that the number of periods in the stack was half of the number of sphere lattice planes present in the starting materials.

In this chapter, I explain the formation of a one dimensional photonic crystal, completely based in a polymeric material that presents strong reflectance peaks in the UV region. This phenomenon is related to the UV light field intensity patterns created during the processing of block copolymer films in the formation of periodic structures of alternating porosity. In this direction, I present optical and structural evidence that demonstrate that the resulting periodic structure is a consequence of the formation of a standing electromagnetic wave generated by thin film interference during the UV irradiation stage. I analyze also if the ordered initial phase in the block copolymer is required to obtain a multilayer of periodic porosity, taking into account that this has a clearly observable effect on the Bragg reflector properties of the final multilayer.

Experimental processing of the samples

A series of films deposited on 2.5x2.5 cm^2 silicon substrates were prepared by spin-coating PS-*b*-PMMA of different total molecular weight ($M_w=M_{wPMMA}+M_{wPS}$) but with approximately the same ratio $\Phi=M_{wPMMA}/M_{wPS}$ ($0.13<\Phi<0.17$). This volume fraction results in a configuration consisting in films of several layers of close-packed PMMA spherical cores, discretely spaced and surrounded by a PS matrix. Appropriate amounts of each polymer were dissolved in toluene to reach a 6% (wt./vol.) concentration and deposited by spin coating onto silicon or quartz substrates. Spin coating final rotation speed and acceleration were adjusted in each BCP solution to attain the same thickness in all PS-b-PMMA films. Films were annealed during 6 hours at 180 ºC under N_2 atmosphere.

The thermal treatment is intended to stabilize a three dimensional lattice of *non-connected* PMMA spheres in a matrix of PS. Using a similar Φ ratio ensures that all samples will have a similar periodic arrangement at the nanoscale, which is expected to be face centered cubic (fcc),[20] while the different M_W will give rise to very different sphere size and hence interplanar distance. PS-b-PMMA slabs were prepared using with M_{wPS}=71 kDa (Φ=0.16), 81 kDa (Φ=0.15), 126 kDa (Φ=0.16) and ,135kDa (Φ=0.14), 295 kDa (Φ=0.15) and 1000 kDa

(Φ=0.14). All poly(styrene-b-methyl methacrylate) [PS-b-PMMA] were purchased from Polymer Source Inc. (Dorval, Canada).

After annealing, all these samples were exposed to the dose (8 J/cm^2) of UV light in a Crosslinker (UVP, Cambridge Instruments) during 20 minutes, a necessary step to attain a periodic porous multilayer, as reported in reference 20. Four 8W light bulbs emitted 254nm light at normal incidence. The irradiation source employed is a 2 mm diameter fluorescent tube located at 20 cm from the sample, which permits to approximate UV light reaching the samples surface as plane waves. The effect of this treatment is to both trigger the crosslinking of PS and degrade the PMMA to low molecular weight oligomers. Finally, films were immersed in acetic acid, a solvent of PMMA that at the same time is capable of diffusing through cross-linked PS without dissolving it.

Study of the annealing effects in the formation mechanism of the multilayer

With the purpose of analyzing morphological changes in the samples after annealing and its effects in the formation mechanism, AFM images of the surface of PS-b-PMMA slabs prepared using M_{wPS} 81 kDa, 135 kDa, 295 kDa and 1000 kDa were taken. A comparison revealed that the arrangement of segregated spheres gradually shift from an ordered (Figures 3a and 3b) to a disordered array (Figures 3c and 3d).

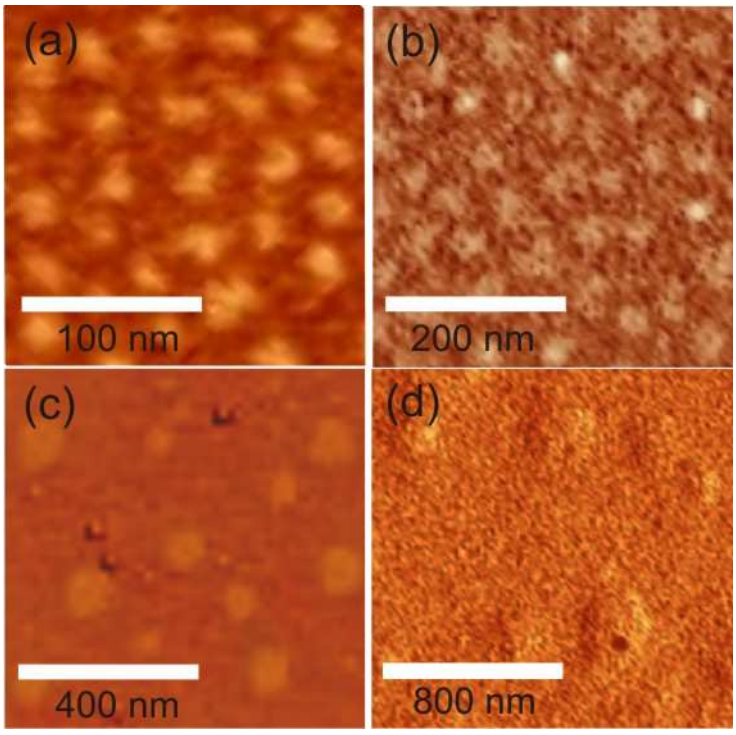

Figure 3: AFM phase images of compositionally asymmetric PS-b-PMMA diblock copolymers with a molecular weight of polystyrene fraction of (a) 82 kDa, (b) 135 k Da, (c) 295 kDa, and (d) 1000 kDa

AFM images were acquired with an AFM Park Systems XE-100. In these images we can roughly estimate the separation between neighboring PMMA spheres *d* is which is related to their size (for the filling fractions around 0.15 like the ones herein considered, sphere diameter can be estimated to be approximately 0.6 times the measured center to center separation *d*). As one of the components is much stiffer than the other at room temperature, atomic force microscopy (AFM) is a useful technique to reveal topological and compositional information of these films.[21] The estimated mean distances are *d*=30 nm, *d*=40 nm, *d*=65 nm and *d*=90 nm for samples of M_{wPS}=71.5 kDa (Φ=0.16), M_{wPS}=81 kDa (Φ=0.15), M_{wPS}=126kDa (Φ=0.16) and M_{wPS}=135 kDa (Φ=0.14), respectively. On the other hand, samples attained from PS-b-PMMA of M_{wPS}=295 KDa (Φ=0.15) or M_{wPS}=1000 kDa (Φ=0.14) present weak first neighboring correlations and less long range order, with estimated mean distances of 280 nm and 500nm respectively. AFM profiles are displayed in Figure 4.

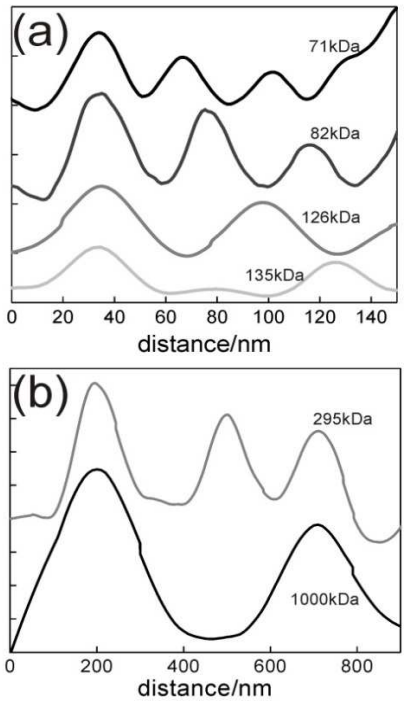

Figure 4: Profile extracted from the AFM image analysis of the surface of the block copolymer films under investigation. Result for (a) small and (b) large PMMA spheres are separated to allow the use of different scales, for the sake of clarity.

It shows the profile of the phase surface obtained by tracing a straight line and analyzing the intensity variation in z axis of AFM images for the different films under analysis after thermal treatment. The molecular weight of the polystyrene fraction is indicated in each case. These

results are in good agreement with those previously attained by high resolution transmission electron microscopy.[19]

Electric Field Distribution of UV radiation

An explanation for the formation of a periodical porous structure out of a PS-b-PMMA layer can be found in the particular field distribution of UV radiation that takes place within the film during processing. All samples employed for this study have the exact same thickness (420 ± 10 nm), as confirmed by the analysis of the interference fringes observed in their total reflectance spectra, shown in Figure 5a. So, a similar spatial pattern of UV light field intensity is expected in all of them upon irradiation. Figure 5b displays the spatial distribution of the square of the electric field, $|E|^2$, for light of wavelength λ=254 nm impinging normally to the film deposited on silicon.

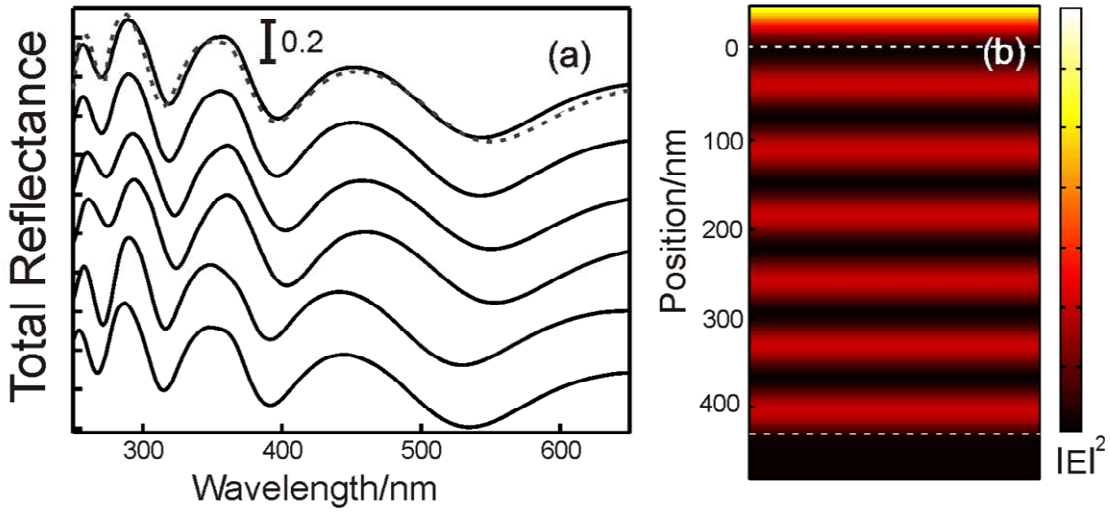

Figure 5: (a) Total reflectance spectra for samples prepared with PS-b-PMMA with M_{wPS} of 71, 81, 126, 135, 296 and 1000 kDa (spectra from above to below, black lines).A theoretical spectrum calculated for a PS-b-PMMA film is included (grey dashed line) (b) Spatial distribution along the cross section (Y axis) of the square of the UV (λ=254 nm) field represented for a PS-PMMA film with a thickness of 420nm deposited on silicon substrate. White dashed lines represent film interfaces. Position at 0 nm represents the interface between air and PS-PMMA film.

Calculations were carried out using a code based on a vector wave transfer matrix method written in MatLab[22] using as input real and imaginary parts of the dielectric constant (see Figures 6a and 6b) attained by fitting the measured total reflectance and total transmittance of the film supported onto a quartz substrate, following a procedure described elsewhere.[23] The extinction coefficient of the BCP film is 0.0056 at λ=254 nm, as can be seen in Figure 6b. The spatial profile of $|E|^2$ is a consequence of the formation of a standing wave in the PS-*b*-PMMA

film as a result of the interference between beams partially transmitted and reflected at the air-polymer and polymer-silicon interfaces. This gives rise to regions of low and high UV intensity illumination periodically distributed along the film cross section. This pattern is translated into an uneven degradation of PMMA and consolidation of PS along the bulk of the film, which should in turn modulate spatially the collective osmotic shock process. So, as $|E|^2$ describes a complete period in approximately 75 nm, each one comprising a pair of low and high intensity fringes, and the film thickness is 420 nm, around eleven layers (five and a half periods) of different microstructure should in principle be expected as a result of such modulation. Changes induced by photochemical effects provoked by UV light should be minimal in those regions in which the $|E|^2$ profile present minima and fully develop around its maxima.

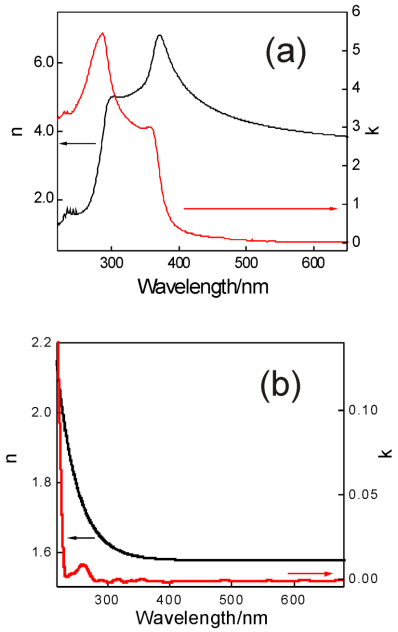

Figure 6: Real (n, black line) and imaginary (k, red line) parts of the refractive index of the silicon (a) and BCP copolymer (b) involved in the theoretical calculations and simulations .

PS based porous one dimensional photonic crystal

When the acetic acid reaches the PMMA through the PS matrix, which acts as a semi-permeable barrier for solvent transfer, osmotic pressure builds up due to swelling of the spherical domains, which deform anisotropically. Thinning of the PS walls in between spheres eventually leads to their rupture and the formation of layers with large pores supported by PS columns, separated from perforated layers of higher density. As it can be seen in Figure 7(a), the final structures attained from PS-*b*-PMMA of M_{wPS} 71, 82, 126 and 135 kDa present strong (up to 80%) reflectance peaks in the UV region that can be unambiguously attributed to Bragg diffraction effects arising from a relatively strong periodic modulation of refractive index (n_L=1.23 and

n_H=1.52, for each pair of consecutive layers) along one spatial dimension that takes place in distances of the order of a hundred nanometers. Samples were immersed in liquid nitrogen before they were cut to analyze the cross section in FESEM. A thin layer consisting in 5 nm of gold was sputtered on samples to avoid charging effects in the FESEM observation. The cross section of these structures displays a periodic alternation of low and high porosity layers, as it can be seen in field emission scanning electron microscopy (FESEM) images displayed in Figures 7(b)-7(e). Please notice that the final thickness of the porous multilayer is larger than the initial 420 nm of the untreated film due to the expansion of the layers upon acid etching and the subsequent swelling and osmotic shock. Interestingly, these four samples present reflection peaks at the exact same spectral position (λ~320nm) regardless of the PMMA sphere size achieved in the segregated phase, in good agreement with the observation of an identical value of the periodicity in the FESEM images.

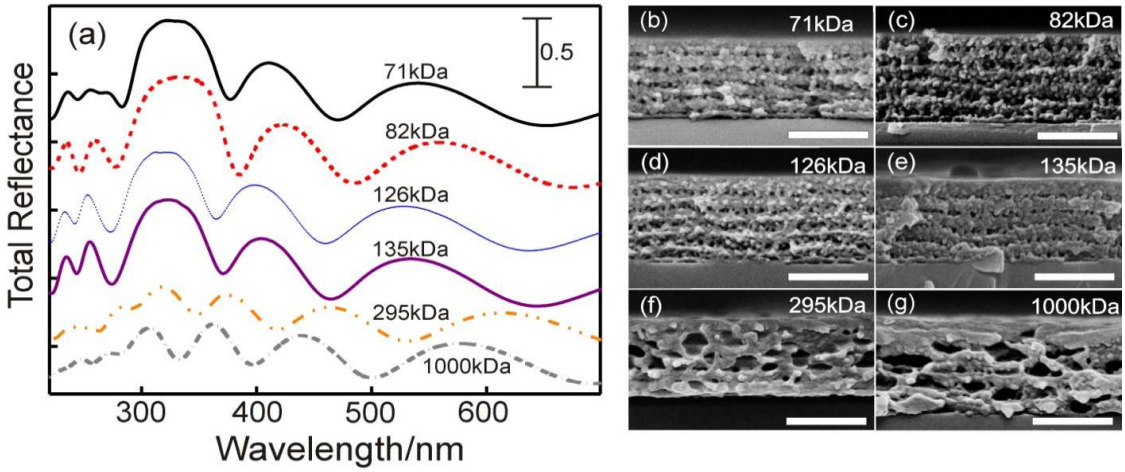

Figure 7: (a) Total reflectance spectra obtained for PS-PMMA of different Mw after irradiation and acetic acid treatment. Molecular weight of polystyrene fraction is indicated next to its corresponding spectrum. (b) to (g), cross section FESEM images obtained from PS-PMMA after UV irradiation and acetic acid treatment. The scale bar is 500nm in all images. Molecular weight is indicated in each FESEM image.

This contradicts our initial hypothesis, in which the alternation between layers of different porosity was proposed to arise *solely* from the particular dynamics of the collective osmotic shock process. If that was the case, the period should gradually increase with the M_W of the PS-*b*-PMMA diblock copolymer, since larger M_W implies longer polymer chains and hence larger separation between sphere planes in the segregated phase. Results presented in Figure 7(a) clearly show that does not occur. On the other hand, no periodic distribution of pores is found in those films made with PS-*b*-PMMA of the largest M_W employed, 295 and 1000 kDa (Figures 7f and 7g), although phase separation occurs like in those of smaller M_W as AFM images reveal. Interestingly, a certain underlying layering is also observed in these cases, but the rupture of

large PMMA spheres by COS gives rise to an optically disordered system that displays no Bragg peak. Two possible reasons might be preventing the formation of a regular multilayer of modulated pore size. Either the thermal annealing is not capable of ordering the spheres in the first place due to its large size, or the disorder is introduced by the acetic acid etching process when dissolving the PMMA, as now the same sphere should present regions with different degrees of depolymerization as a consequence of the spatial modulation of the UV induced photochemical effects introduced by the electromagnetic field distribution. Hence the model herein proposed based on the distribution of the UV light field within the PS-*b*-PMMA films accounts both qualitatively and quantitatively for the formation of a periodic stratified structure of pores, as long as the PMMA spheres present in the slab are not too large compared to the period of the $|E|^2$ profile. In our case, this period is 75 nm while sphere diameters estimated from our AFM image analysis are around 20 nm (M_{wPS}=71.5 kDa), 25 nm (M_{wPS}=81 kDa), 40 nm (126 kDa), 55 nm (135 kDa), 170 nm (295 kDa) and 300 nm (1000 kDa). Our new hypothesis also explains other previous observation, like the absence of any periodicity when BCP films are exposed to a very high UV dose, since the regions of minimum $|E|^2$ would then present enough PMMA depolymerization and PS stabilization as to behave just like the more intensely illuminated ones.[24] Also, it explains why the exposure time required is longer for those systems in which a less reflective substrate is employed, as the intensity of the high $|E|^2$ fringes depends on that parameter.

Full vector wave theoretical calculations of the electromagnetic field intensity distribution across the diblock copolymer film.

In order to further test the validity of our assumption, we realized a series of experiments to confirm other predictions that can be made on such basis. First, we deposit a film of PS-*b*-PMMA onto an unpolished silicon substrate. Deposition by spin-coating creates a polymer coating that presents a flat outer surface to incident light and a corrugated inner one against the substrate. Unpolished wafers present flat regions tilted with respect to each other, and the field distributes in high and low intensity fringes parallel to each one of such regions and therefore oblique with respect to the BCP film surface, as shown in the $|E|^2$ profiles displayed in Figures 8a and 8b. In this case, field intensity patterns have been estimated using a commercial code (Lumerical) based on finite-difference-time-domain (FDTD) by Dr. Juan Galisteo. The simulated structure was designed using the cross section obtained from the SEM images shown in figures 8c and 8d. In the simulation the polymer thickness was assumed to be that of the un-swelled system (approximately 80% of the final thickness) and the irradiation beam was a plane wave with wavelength 254 nm incident normally on the polymer/air interface. A sufficiently fine grid (≥20 points per wavelength) and long simulation times (≥1 ps) were used in order to correctly simulate the structures.

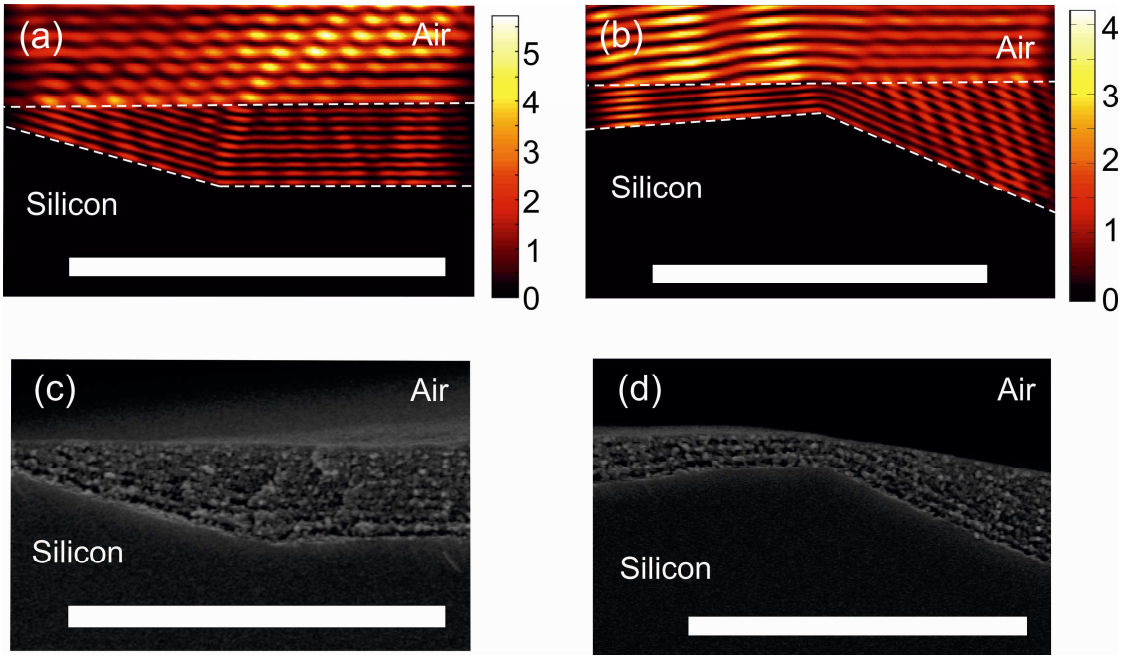

Figure 8: (a, b) Total field intensity calculated for systems having the shape extracted from SEM images of samples depicted in (c, d) respectively. Air/polymer and polymer/silicon interfaces are indicated by dashed white lines in the simulations. Scale bars correspond to 3 μm in all cases.

Interestingly, after thermal and UV processing and acetic acid etching, periodic alternation between porous and dense layers occur parallel to the flat silicon surfaces, as shown in Figures 8(c) and 8(d), rather than to the flat top surface. These pictures allow us to confirm that the observed layering replicates the calculated spatial profile of $|E|^2$ in the precursor PS-*b*-PMMA film. Further evidence of the replication of the field intensity distribution attained at dynamically variable angle of incidence of UV light is provided what follows. As will be explained in details, disorder is induced in part of the film as a result of the spreading of the high intensity field fringes due to the continuous rotation of the film.

Effect of a dynamically variable UV irradiation angle.

The effect of changing dynamically the direction of the incident UV light on a film deposited on a flat substrate was also studied. As the formation of a regular pattern of high and low light intensity fringes within the film depends on the angle of illumination, we decided to expose our films to a similar overall dose of UV light but using as a holder a rotating plate that described an arc of 60º with an angular speed of 2/3π rad/s. For a given wavelength, the spatial position of high light intensity regions varies, as shown in the angle dependent $|E|^2$ profiles plotted in Figure 9a, particularly in the region closer to the BCP-air interface.

This angular shift gives rise to a smoothing of the modulation of the photochemical effects, leading eventually to the absence of a periodic pattern of pores, as it can be confirmed in both

the FESEM image of its cross section, Figure 9b, and the optical reflectance spectra, Figure 9c. Please notice that the $|E|^2$ profile is less sensitive to the angle of incidence in the lower part of the film, close to the BCP-silicon interface, in which the alternate porous-dense layered structure is preserved.

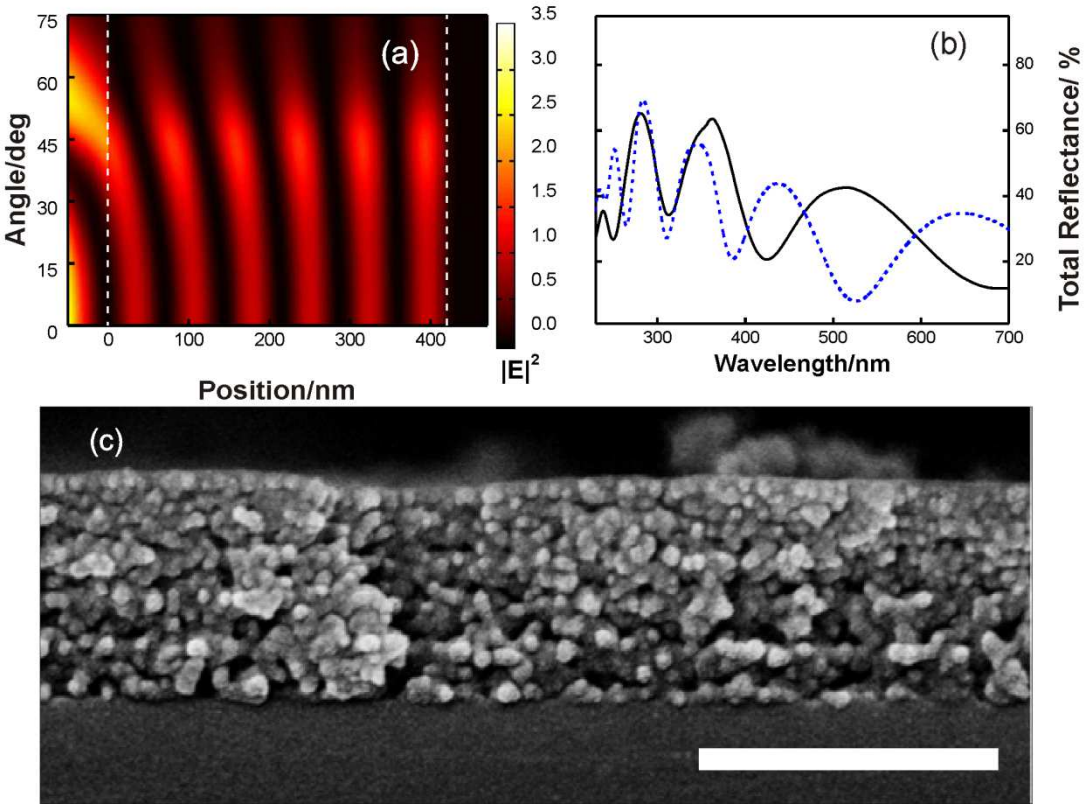

Figure 9: (a) Spatial distribution along the cross section (X axis) of the squared UV electric field calculated for a PS-PMMA film with a thickness of 420 nm deposited on silicon substrate as a function of the angle of incidence (Y axis). White dashed lines represent film interfaces. The vertical white dashed lines indicate the interfaces between air and PS-PMMA (x=0 nm) and PMMA-silicon (x=420 nm). (b) Total reflectance spectra obtained for a PS-PMMA of Mw_{PS}=82.5 kDabefore (blue short dashed line) and after irradiation with UV light (λ=254 nm) at variable direction of incidence $0^o<\alpha<60^o$ and treatment with acetic acid (black solid line). (c) FESEM image of the cross section of the film under angle variation incidence. Scale bar is 500 nm.

Finally, I analyzed the interplay between the ordering of PMMA spheres achieved during the thermally triggered phase segregation and that imposed by the spatial modulation of the UV induced photochemical effects. In order to do so, we prepared two series of films of similar thickness. One of them was annealed, in order to yield a 3D periodic arrangement of PMMA spheres in the PS matrix, and the other one was not, so that PMMA would be randomly distributed in the film.

For these experiments we employed flat quartz substrates, since they would allow analyzing the potential differences between Bragg peak shapes with more precision than silicon substrates. The reason is that Bragg reflection maxima would be less distorted by the secondary Fabry-Perot reflectance lobes caused by the finite size of the film, since quartz has a lower refractive index. Using quartz means that the UV dose to attain a periodic structure has to be increased to 15 J/cm^2, due to its lower reflectivity compared to that of silicon as it has been previously reported.[19] In Figure 10 I plot the spectra of these differently processed films, prepared using PS-*b*-PMMA of M_W=135 kDa, after acetic acid etching. It can be seen that, although in both cases a clear Bragg reflectance peak arise, the one that was not thermally annealed (i.e., the one with disordered PMMA spheres) and a less intense (R=21% versus R=27%) maximum.

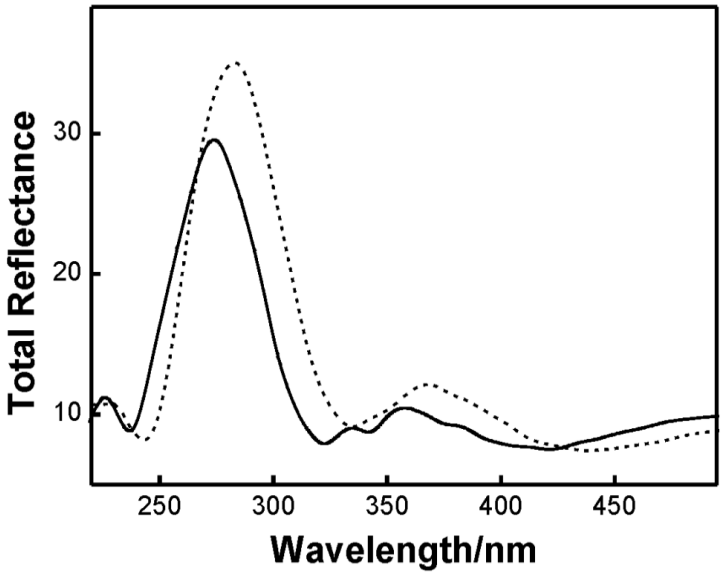

Figure 10: Reflectance spectra obtained after the irradiation at normal incidence and acetic acid treatment for PS-PMMA block copolymer films deposited onto quartz with (dashed lines) and without (solid lines) annealing. Molecular weight of polystyrene used is 135 kDa.

These latter features are characteristic of a multilayer mirror in which the interface between two consecutive layers is not well defined, which yields a middle region of effective intermediate refractive index that gives rise to a strong decrease of the reflectance. Hence, the observed effects, which were systematically detected in all pair of films analyzed, indicate that those films in which the field intensity pattern is superimposed to the an ordered structure of PMMA spheres present a better defined interface between neighboring layers than those in which no ordering was prompted by temperature. Our analysis therefore shows that, although ordering in the starting film is not mandatory to achieve a periodic multilayer, as the presence of alternate porous and dense layers is determined by the spatial modulation of the photochemical processes induced by UV light, it is indeed necessary to attain a well-defined interface between such

regions. This is of particular relevance for potential applications of these coatings as UVB reflectors.

Conclusions

I have presented experimental evidence of the key role that UV light field intensity patterns play in the formation of periodic structures of alternated porous and dense layers after undergoing a collective osmotic shock. Such periodicity had been originally attributed to dynamic effects during the collective osmotic shock process occurring over ordered arrangements of isolated PMMA spheres embedded in a cross-linked polystyrene matrix in the starting slab, which had previously been subjected to thermal and UV annealing processes. However, a number of key features remained unexplained by this postulate. By comparing the experimental results of structural and optical characterization of different films and the UV field patterns simulated using different computational tools, we were able to confirm that the observed periodicity arises as a result of the combination of the spatial modulation of UV induced photochemical effects and the osmotic shock process. Several predictions based on this new hypothesis have been experimentally confirmed and the origin of previous intriguing observations clarified under this assumption. These results may serve as starting point to design more complex patterns within block copolymers by three dimensional laser interference in a similar way to what is done with homopolymers.

References

[1] Bailey, J.; Sharp, J. S. J. Polym. Sci., Part B: Polym. Phys.
2011, 49, 732–739.

[2] Urbas, A.; Sharp, R.; Fink, Y.; Thomas, E. L.; Xenidou, M.;
Fetters, L.J. Adv. Mater. 2000, 12, 812–814.

[3] Yokoyama, Y.; Nakayama, K.; Otani, T.; Kido, J. *Adv. Mater.*, **2012**, 24, 6368.

[4] Park, C.M.; Yoon, J.S.; Thomas, E.L. *Polymer***2003**, *44*, 6725.

[5] Nie,Z.; Kumacheva,E. *Nat. Mater*, **2008**, *7*, 277-290.

[6] Stoykovich, M.P.; Nealey, P.F., *Mater. Today*, **2006**, *9*, 20.

[7] Jeong, S.J.; Kim, J.Y.; Kim, B.H.; Moon H.S.; SO Kim, S.O., *Mater. Today*, **2013**, *16*, 468.

[8] Walheim, S.; Schaffer, E.; Mlynek, J.; Steiner, U., *Science*, **1999**, *283*, 520-522.

[9] Hillmyer, M.A.; *Adv. Polym. Sci*., **2005**, *190*, 137–181.

[10] Olson, D. A.; Chen, L.; Hillmyer ,M. A. *Chem. Mater.* **2008**, *20*, 869–890.

[11] Hamley, I.W., *Nanotechnology*, **2003**, *14*, R39-R54.

[12] Thébault, P.; Niedermayer, S.; Landis, S.; Chaix, N.; Guenoun, P.; Daillant, J.; Man, XK; Andelman, D.; Orland, H., *Adv. Mater.*, **2012**, *24*, 1952.

[13] Niedermeier, M.A.; Tainter, G.; Weiler, B.; Lugli, P.; Müller-Buschbaum, P., *J. Mater. Chem. A*, **2013**, *1*, 7870.

[14] Tang, C.; Sivanandan, K.; Stahl, B.C.; Fredrickson,G.H.; Kramer, E.J.; Hawker, C.J., *ACS Nano*, **2010**, *4*, 285-291.

[15] Schaeffer, E.; Thurn-Albrecht, T.; Russell, T.P.; Steiner, U., *Nature*, **2000**, *403*, 874.

[16] Stoykovich, M.P.; Müller, M.; Kim, S.O.; Solak, H.H.; Edwards, E.,W.; de Pablo, J.J.; Nealey, P.F., *Science*, **2005**, 308, 1442.

[17] Urbas, A.M.; Maldovan, M.; DeRege, P.; Thomas, E.L., *Adv. Mater.*, **2002**, *14*, 1850-1853.

[18] Scherer, M.R.J.; Steiner. U., *Nano Lett.*, **2013**, *13*, 3005−3010.

[19] Zavala-Rivera, P.; Channon, K.; Nguyen, V.; Sivaniah, E.; Kabra, D.; Friend, R.H.; Nataraj, S.K.; Al-Muhtaseb, S.A; Hexemer, A.; Calvo, M.E.; Miguez, H., *Nat. Mater*, **2012**, *11*, 53-57.

[20] M. Lazzari, G. Liu, S. Lecommandoux, *Block Copolymers in Nanoscience*, 2006 WILEY-VCH VerlagGmbH&Co. Germany, Weinheim. ISBN: 978-3-527-31309-9.

[21]G.H. Michler, *Electron Microscopy of Polymers*, 2008, Springer-Verlag Berlin Heidelberg. ISBN: 978-3-540-36350-7.

[22] Luque-Raigon, J.M.; Halme, J.; Miguez, H., *J Quant. Spectrosc.Radiat. Trans.*, **2014**, *134*, 9-20.

[23] Nichelatti, E., *J. Opt. A: Pure Appl. Opt.*, **2002**,*4*, 400–403.

[24] Joo, W.; Park, M.S.; Kim, J.K., *Langmuir*, **2006,** *22*, 7960-7963.

General Conclusions

First of all, TiO_2, ZrO_2, Nb_2O_5 nanoparticles were successfully synthesized as suitable building blocks for one dimensional photonic crystals. The metal oxide nanoparticles used, with nanometric sizes that are required to obtain high optical quality and to avoid diffuse scattering in the photonic structures, present no absorption in different UV ranges.

Rigid coatings and flexible self-standing films were designed to be capable of efficiently protecting against UV radiation in selected wavelength ranges entirely through optical reflection phenomena. It was demonstrated that these films may equal or outperform layers of similar thickness made of purely absorbing materials in terms of the degree of radiation protection achieved.

Flexible photonic filters and tandems of them were made to shield the action spectrum of UV light on the skin. It was demonstrated that it is possible to build flexible films capable of efficiently protecting epithelial cells from UVB radiation that produces DNA lesions.

Experimental evidence of the key role that UV light field intensity patterns play in the formation of periodic structures of alternated porous and dense layers with photonic crystal properties, after undergoing a collective osmotic shock process, was presented. It was confirmed that the observed periodicity arises as a result of the combination of the spatial modulation of UV induced photochemical effects and the osmotic shock process.

Resumen en Español

Nanoestructuras híbridas flexibles para aplicaciones como filtros ópticos para la protección contra la radiación ultravioleta

Introducción

La gran cantidad de aplicaciones que encontramos para la luz ultravioleta (UV) en la medicina,[1] la cosmética,[2] o en la industria en general,[3,4]exigen estudios más detallados y profundos de los riesgos que entraña el uso de este tipo de radiación electromagnética, así como una mayor investigación en el desarrollo de nuevos materiales para proteger selectivamente contra ella. Existe un amplio conocimiento del daño que la radiación UV causa a materiales orgánicos como plásticos, maderas, o polímeros, entre otros.[5,6]Las reacciones químicas inducidas por la absorción de luz UV, dan lugar a la formación de radicales libres que traen como resultado la fotodegradación posterior del polímero.[7,8]Además, son bien conocidos los efectos nocivos que provoca este tipo de radiación sobre la salud humana, específicamente sobre la piel, donde encontramos una variedad de dermatosis fotosensibles,[9] cáncer de piel,[10] o ejemplos como la formación de cataratas[11] y la degeneración macular[12] en el sistema ocular.

En este contexto, la creación de películas de polímeros que actúan como escudos contra la radiación UV constituye en la actualidad un campo activo e interesante de la investigación,[13-18] ya que logran adaptarse a amplia variedad de entornos sensibles a la radiación UV. En particular, el desarrollo de este tipo de estructuras tiene un gran potencial en aplicaciones referentes al campo de la biomedicina debido a la posibilidad de bloquear selectivamente la

radiación UV en diferentes tejidos humanos tales como piel y retina, Por ejemplo, en un futuro próximo, los pacientes se beneficiarían en gran medida de la existencia de láminas flexibles que podrían adaptarse a su piel dañada, las cuales bloquean la radiación UV perjudicial, y al mismo tiempo, permiten ventanas de transmisión en rangos terapéuticos, teniendo en cuenta que muchos de los compuestos protectores o filtros solares, son incompatibles con las heridas o quemaduras abiertas. Del mismo modo, estas estructuras podrían ser utilizadas en dispositivos ópticos plegables, garantizando una protección eficiente contra la luz UV, al tiempo que se preserva una alta transparencia en el visible.

Las películas usadas para el bloqueo de radiación UV pueden ser clasificadas de acuerdo con el mecanismo físico responsable del efecto de protección, a saber, la absorción óptica o la reflexión. En general, el enfoque más ampliamente extendido a la protección UV, ya sea en lociones de protección solar o en cualquier material cuya degradación se deba prevenir, se basa en el uso de absorbentes UV orgánicos,[19-21] que transforman la radiación entrante en disipación térmica de baja energía mediante reacciones fotofísicas. Por otro lado, cuando se usan nanopartículas de óxidos metálicos, que protegen contra la luz UV por dispersión y/o absorción óptica, estas son embebidas en una matriz polimérica dando lugar a nanoestructuras orgánicas-inorgánicas híbridas. En todos estos enfoques, la función de los polímeros es la de proporcionar flexibilidad, tenacidad y resistencia a la fractura,[22] así como otros valores agregados significativos tales como la bio-compatibilidad o la funcionalidad química o biológica. Además, la absorción ultravioleta del polímero se debe evitar para impedir reacciones fotoquímicas que podrían conducir a una pérdida de elasticidad o de una coloración amarillenta de la película. Estos requisitos reducen la gama de polímeros utilizables a los que pertenecen a las familias de poli(alquil)siloxano, poli(alquil)acrilato o de poliestireno. Desde una perspectiva diferente, cuando se busca la reflexión en lugar de la absorción de longitudes de onda UV, arquitecturas complejas de multicapas deben ser empleadas, de modo que los efectos de interferencia pueden dar lugar al efecto de bloqueo deseado.

Es bien sabido que la radiación de longitud de onda arbitraria puede ser bloqueada por medio de la utilización de los llamados filtros de interferencia o espejos de Bragg. Estos tipos de espejos se preparan por capas de diferente índice de refracción.[23] Ellos son conocidos como cristales fotónicos unidimensionales (1DPC, por sus siglas en inglés), siguiendo una clasificación más estricta de las redes ópticas periódicas. Los cristales fotónicos son estructuras en los cuales el índice de refracción varía periódicamente en una o más direcciones espaciales. Los 1DPCs son la estructura de cristal fotónico más simple, en el que la constante dieléctrica es periódica en una dimensión del espacio. Convencionalmente, la banda fotónica prohibida y, por lo tanto, la reflexión total para un rango de frecuencias que se distingue como pico de Bragg, se explican por la interferencia entre las ondas reflejadas por las capas sucesivas. La respuesta óptica de los 1DPCs puede ajustarse variando la cantidad de capas, la celda unidad, y el índice de refracción.

Hace unos años, un nuevo tipo de 1DPC poroso hecho de nanopartículas de óxidos metálicos como bloques constituyentes fue desarrollado por nuestro grupo.[24] La porosidad ofrece una nueva dimensión multifuncional a los cristales fotónicos, que se capitalizó en nuevas aplicaciones de diversos campos tales como el sensado, aplicaciones con láseres y la energía fotovoltaica.[25-28] Como condición necesaria, es importante mantener un estricto control sobre el tamaño de las partículas en el rango de las decenas de nanómetros para evitar la aparición de luz difusa en el visible. Además, la porosidad en las capas debe ser interconectada, ya que se demostró que estas estructuras ópticas pueden ser infiltradas con polímeros para obtener un 1DPC híbrido que puede ser levantado del sustrato.

Esto es fundamental en aras de alcanzar continuidad en la masa del polímero infiltrado para asegurar la estabilidad mecánica del conjunto final. Este nuevo material híbrido tiene las propiedades ópticas de la estructura inorgánica y las propiedades mecánicas del polímero infiltrado. El esquema de este proceso se muestra en la Figura 1.

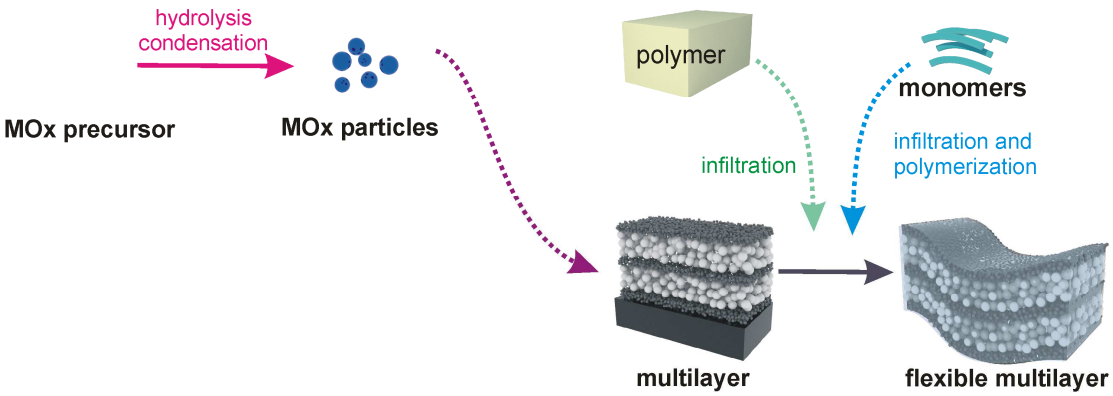

Figura 1: Vías sintética de la síntesis de películas de polímeros flexibles basados en multicapas de nanopartículas hechas a partir de una capa porosa.

Otro material que presenta altas reflectancias en el UV, que será ampliamente estudiado en esta tesis, se basa en un cristal fotónico totalmente polimérico. Un estudio acerca de un fenómeno físico-químico observado en los polímeros que conduce a la creación de capas poliméricas bi-continuas fue reportado recientemente. En el mismo se realizó un intento exitoso para estructurar un polímero como un 1DPC que opera en el UV, el cual se realizó mediante el uso de un tratamiento de choque osmótico de un copolímero de bloques depositado por spin coating, aunque no se ha obtenido una estructura flexible todavía.[29]

Motivación y los objetivos de esta tesis

Como se ha explicado, la inmensa mayoría de los materiales que protegen contra la luz UV, presentan limitaciones que afectan sus propiedades ópticas y mecánicas, y por tanto, su durabilidad, ligadas al mecanismo de protección que presentan. Muchos de estos inconvenientes pueden superarse con el uso de estructuras fotónicas flexibles que bloqueen la luz ultravioleta por reflexión, y que se pueden adaptar a superficies con diferentes geometrías.

En esta tesis se ha planteado utilizar estas estructuras para bloquear específicamente un determinado rango espectral de frecuencias en la región UV del espectro. Para llevar adelante esta tarea, se plantearon los siguientes objetivos:

- Sintetizar nanopartículas de óxidos metálicos para ser utilizadas como bloques constituyentes de los espejos reflectores UV.

- Diseño y creación de cristales fotónicos nanoparticulados flexibles que protejen selectivamente frente a la radiación UV.

- Creación de filtros flexibles que bloquean específicamente el UVB para proteger diferentes tipos de células epitaliales que presentan una fuerte genotoxicidad en el rango mencionado. Analizar la eficacia de la protección UV, midiendo el grado de daño causado en el ADN de las diferentes células epiteliales expuestas a una fuente de UV.

- Análisis del mecanismo detrás de la formación de un cristal fotónico unidimensional totalmente polimérico, después de tratar con radiación UV y químicamente una capa de PS-b-PMMA, y los cambios microestructurales y de las propiedades ópticas que se producen.

Síntesis de nanopartículas y los métodos de preparación de multicapas

En primer lugar, se describe la síntesis y la caracterización de diferentes tipos de nanopartículas que permiten construir estructuras multicapas flexibles con propiedades reflectantes en la región UV. Además, se detallan los métodos de deposición empleados para hacer estas películas con una alta calidad óptica. Para para la síntesis de las nanopartículas de óxidos metálicos de esta tesis, se utiliza el método sol-gel,[30-32] ya que éste da la posibilidad de modificar el tamaño de las nanopartículas y de alterar la porosidad de las estructuras construidas.

Como ya veremos más adelante es importante que las partículas que se sinteticen presenten muy baja absorción en el rango espectral de UV. Los coloides esféricos de SiO_2 no presentan absorción en el UVA, UVB y el UVC, por lo que cumplen este requisito a la perfección. Por otra parte, y no por ello menos importante, las láminas de SiO_2 presentan un bajo índice de refracción en comparación con otras nanopartículas. Además, la suspensión de SiO_2, adquirida en Dupont (Ludox TMA, Aldrich), es muy estable, monodispersa y con un diámetro de partícula de alrededor de 30 nm. Esto hace que las estructuras desarrolladas en esta tesis incluyan preferentemente partículas de SiO_2.

Los nanocristales de TiO_2 se sintetizan a partir de la hidrólisis de isopropóxido de titanio (TTIP 97%, Aldrich), seguida con el crecimiento bajo condiciones hidrotermales.[33] El tamaño determinado de las nanopartículas de TiO_2 es de aproximadamente 10 nm. Las nanopartículas de TiO_2 presentan el borde de banda prohibida electrónica en λ = 340 nm (Egap = 3, 64 eV). Un material que presenta un band-gap más ancho que las nanopartículas mencionadas, lo encontramos en Nb_2O_5, que presenta un frente de absorción en aproximadamente 310 nm. Una suspensión de nanopartículas de Nb_2O_5 se preparó siguiendo el método sol-gel a partir de pentacloruro de niobio (99%, Alfa Aesar) como precursor en la ruta de síntesis.[34] Se obtuvieron nanopartículas de 18-20 nm de diámetro.

Óxido de zirconio también fue sintetizado en forma de nanopartículas. Las mismas se sintetizaron usando un procedimiento basado en la hidrólisis del n-propóxido de zirconio (70%, Alfa Aesar).[35] Se obtuvo una suspensión coloidal estable de nanopartículas de ZrO_2 con un diámetro aproximado de 6 nm, las más pequeñas sintetizadas en esta tesis. El borde de absorción se sitúa en λ = 220 nm (Egap = 5,63 eV).

Una vez obtenidas las nanopartículas con las propiedades deseadas, procedemos a depositar las capas por spin coating o dip coating. El proceso se repite de forma contuinuada, alternando los dos tipos de capas de nanopartículas hasta completar la estructura entera. Una de las características más importantes que aportan estas técnicas de deposición es la capacidad de adaptar con precisión las propiedades microestructurales y ópticas de la película depositada. Por ejemplo, la posición del pico de Bragg puede ser controlada, modificando la velocidad de rotación para el caso del spin coating o la velocidad de retirada en el caso del dip coating.

Cristales fotónicos unidimensionales nanoparticulados flexibles para protección contra la radiación UV

En este capítulo, se explica un procedimiento sobre cómo construir y diseñar cristales fotónicos unidimensionales con nanopartículas de Nb_2O_5 y ZrO_2 y SiO_2 en aras de crear películas flexibles individuales para proteger contra la radiación ultravioleta por reflexión óptica. Para una protección en el UVA, se propone un cristal fotónico unidimensional nanoparticulado SiO_2/Nb_2O_5 a través de un proceso de spin coating[36], mientras que para bloquear eficientemente diferentes rangos de longitud de onda UV comprendidas entre λ = 200 nm y λ = 400 nm, se presenta una serie de cristales fotónicos SiO_2/ZrO_2. Las características microestructurales de estos 1DPCs porosos pueden ser exploradas a través de las imágenes de FESEM, en las cuales se puede ver la sección transversal de los sistemas multicapas SiO_2/ZrO_2 (a y b) y SiO_2/Nb_2O_5 (c y d). En esta figura se aprecian láminas homogéneas con interfaces planas flanqueadas por ellos (Figuras 2a y 2c) para las imágenes de electrones secundarios. En las figuras 2b y 2d podemos ver imágenes de electrones retrodispersados de la misma región espacial, revelando visiblemente las interfaces ininterrumpidas y planas conectando capas sucesivas. En estas imágenes las líneas más intensas pertenecen a las capas de ZrO_2 y Nb_2O_5.

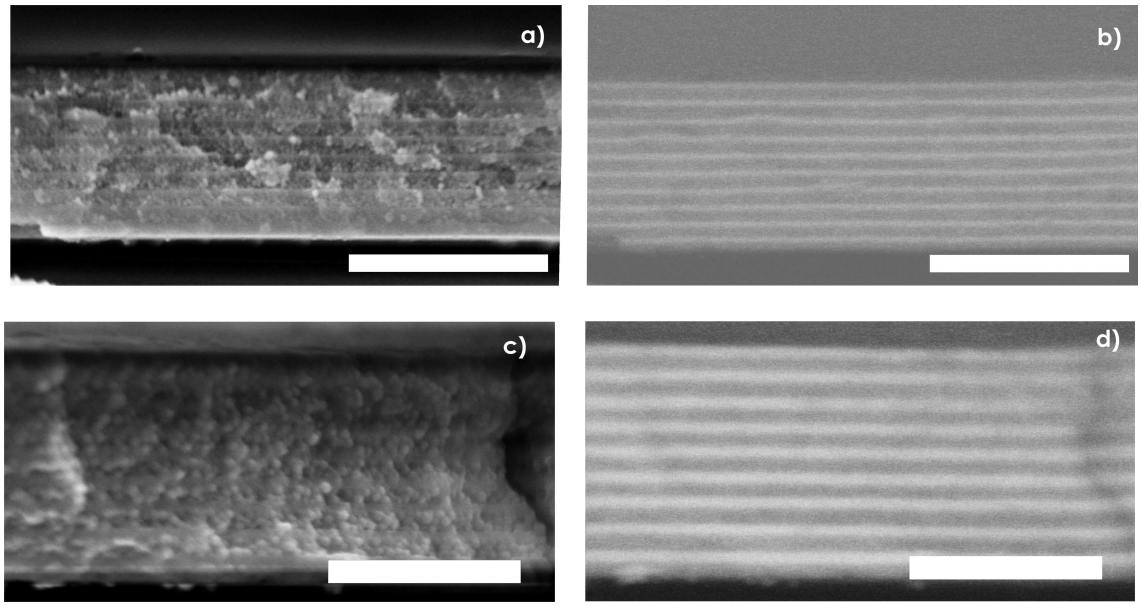

Figura 2: Imágenes FESEM de las secciones transversales de dos cristales fotónicos 1D hechos a partir de SiO2 (coloides esféricos), con nanopartículas de ZrO_2 (a y b) y Nb_2O_5 (c y d) respectivamente, obtenidos detectando (a y c) electrones secundarios y (b y d) electrones retro-dispersados. La barra de escala es de 1 µm en todas las figuras.

Como se puede observar, no existe una interpenetración considerable entre las capas, lo que afectaría el contraste en el índice de refracción, y por lo tanto la intensidad de picos de Bragg.

Este sistema permite depositar hasta 26 capas que permiten alcanzar una intensidad máxima de 100%.

El ajuste teórico de estos espectros de reflectancia permite calcular los valores de los índices de refracción y los grosores de las capas que forman por medio de un código basado en un formalismo de matriz de transferencia.[37] El espesor de las capas se acota a partir de las imágenes de FESEM. A partir de este análisis, extraemos los valores de índice de refracción para las capas de n_{ZrO2}=1.70, n_{Nb2O5}=1.76 y n_{SiO2}=1.31, teniendo en cuenta que los índices de refracción para sistemas densos de estos materiales tienen los valores 2.25, 2.26 y 1.43 respectivamente. El esquema sugerido permite que los picos de Bragg tengan una ubicación precisa en diferentes posiciones espectrales, sólo variando la concentración de la suspensión precursora o variando los parámetros de spin coating. Se estimó la absortancia como $A=1-R_T-T_T$ (ver figura 4c) para establecer el umbral en el que las pérdidas ópticas por absorción en la multicapa son significativas. En las Figuras 3a, 3b y 3c se presentan gráficas de reflectancia total, transmitancia total y absortancias calculadas, obtenidas a partir de cristales fotónicos de SiO_2/Nb_2O_5 depositados a diferentes velocidades de rotación.

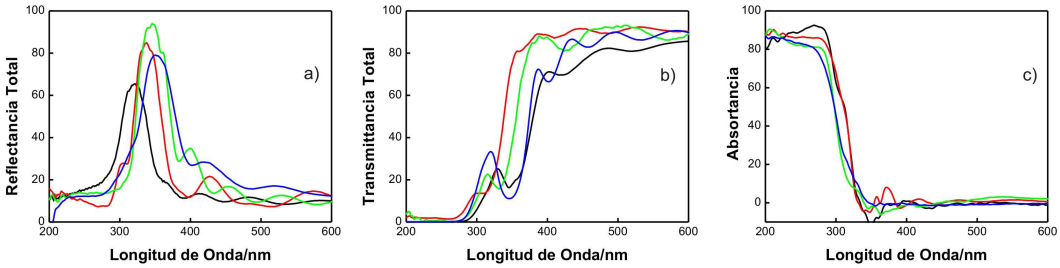

Figura 3: Reflectancia total, b) transmitancia total, y c) absortancia de cristales fotónicos basados en SiO_2/Nb_2O_5. Las velocidades de rotación finales fueron 3.000 rpm (línea azul), 4000 rpm (línea verde), 5000 rpm (línea roja) y 7000 rpm (línea negra). Las concentraciones de nanopartículas SiO_2 y Nb_2O_5 en metanol se mantuvieron en 2,5% en ambos casos. Los espesores de celda unidad son 98 nm, 108 nm, 115 nm y 120 nm respectivamente. El número total de celdas unidad es 10 en todos los casos.

Como puede verse, se obtuvieron picos de reflectancias de alrededor del 90%, que protegen contra la radiación UV de 300 a 400 nm a través de la reflexión, evitando la absorción como se puede apreciar en la figura 3c, con un 50% de absorción en 300nm y cercano al 0% en 350nm. Además, la transparencia de las muestras en la región visible (390-750 nm), que se calcula de acuerdo a métodos estándar empleados comúnmente para determinar la transmitancia de luz de la radiación solar para el acristalamiento en los edificios (ISO 9050: 2003), en donde se tiene en cuenta la respuesta fotópica del ojo, es de alrededor de 90% en todos los casos.

En el sistema SiO_2/ZrO_2 podemos observar resultados similares para el mismo número de celdas unidad, con la diferencia de que la absorción en las capas de ZrO_2 nos permiten la construcción de 1DPCs sin absorción en un rango espectral más amplio, con un 5 % de absorción en 250nm y

cercano al 0% en 300nm. En la figura 4a, 4b y 4c, se muestran los espectros de reflectancia, transmitancia y absortancia respectivamente.

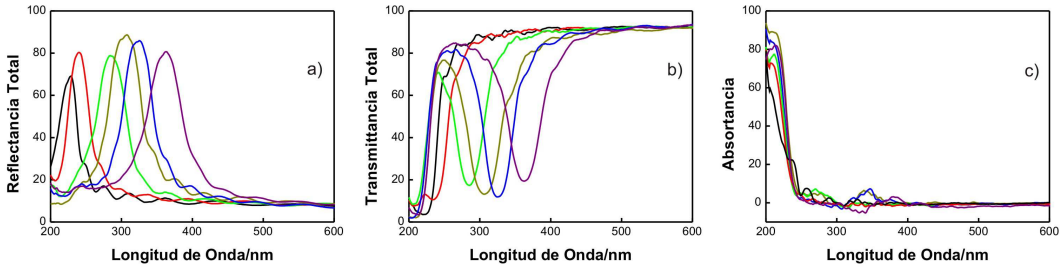

Figura 4: (a) Espectros de reflectancia total, (b) transmitancia total y (c) absortancia de películas de interferencia ZrO_2/SiO_2. Todas las capas se depositaron mediante spin coating (ω = 6000 rpm y γ = 11500 rpm / s) con diferentes concentraciones de nanopartículas pero expresadas como [SiO_2 % en peso, ZrO_2 % en peso.]): [1.0, 2.5] (sólido negro); [1.5, 2.5] (rojo sólido); [2.0, 2.5] (sólido verde); [2.25, 2.5] (sólido amarillo oscuro); [2.25, 3.0] (sólido azul), [2.5, 3.0] (sólido púrpura). Los espesores de celda unidad son 75 nm, 80 nm, 95 nm, 105 nm, 110 nm y 125 nm, respectivamente. El número total de celdas unidad es 10 en todos los casos.

Sistemas flexibles

La porosidad de estas estructuras ofrece la posibilidad de construir espejos versátiles autosoportados, las cuales se obtienen después de infiltrarlas con PDMSy enfriar la estructura híbrida por debajo de la temperatura de transición vítrea del polímero.(en nuestro caso 77K). Posteriormente la película completa se despega del sustrato cuando se alcanza temperatura ambiente. En la figura 5a se muestran los espectros de reflectancia de siete cristales fotónicos flexibles SiO_2/ZrO_2 de diferentes grosores.

Estas películas se realizaron con sistemas de hasta 13 celdas unidad. Esto se debe a que el máximo de intensidad en su posición espectral disminuye después de la infiltración PDMS. Esto es producto de la disminución del contraste de índice de refracción entre las capas de SiO_2 y ZrO_2 cuando el polímero llena los poros de la estructura. Las muestras obtenidas son mecánicamente estables y de gran flexibilidad, tal como se muestra en las imágenes de la figura 5b.

La estabilidad mecánica y la flexibilidad de las películas de diferente parámetro de red que protegen contra las regiones de longitud de onda bien definidas a lo largo del rango 200nm-400nm, abre el camino para bloquear selectivamente regiones espectrales anchas ya que estas películas se pueden unir para crear tándems constituidos por diferentes combinaciones de películas protectoras UV.

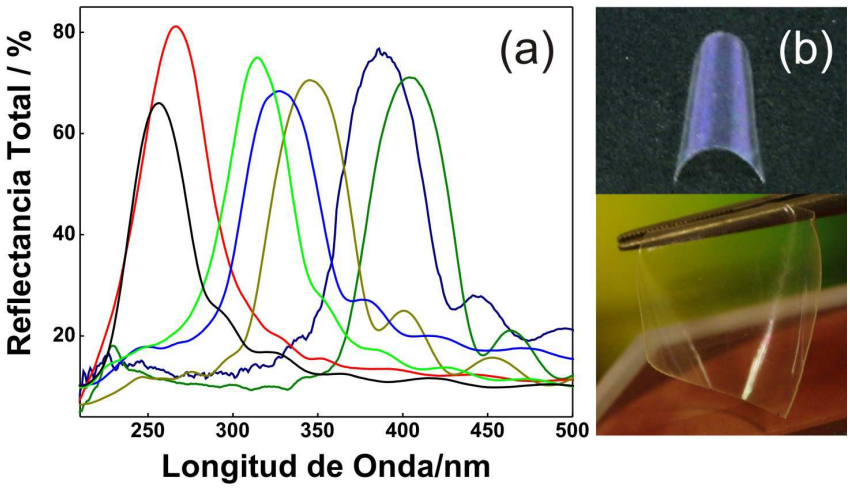

Figura 5: (a) Espectros de reflectancia total de cristales fotónicos flexibles SiO_2/ZrO_2 individuales. (b) Fotografías de films flexibles de SiO_2/ZrO_2.

En la Figura 6 se muestra la reflectancia total, transmitancia total y absortancia para tándems que contienen 1, 2, 3, 5 y 7 películas, cada una de estas estructuras mostrando su característico pico de Bragg en diferentes posiciones espectrales en el UV. Estos tándems están formados por películas que se unen secuencialmente, empezando por el que refleja las longitudes de onda más cortas hasta el que refleja más cerca de la región azul. A medida que el número de films individuales aumenta, el rango espectral se amplía a toda la gama UVC-UVB-UVA, protegiendo todo este rango para el caso de 7 películas apiladas, mientras se mantiene una transparencia de 60% en la región visible. La reducción observada de la transparencia con respecto a una única multicapa flexible es debido a la dispersión de luz por irregularidades en las interfaces entre las capas de PDMS puestas en contacto. Desde el punto de vista de la protección contra la radiación UV, este simple método puede ser utilizado para proteger selectivamente contra una región espectral de interés, así como para imitar o superar el efecto de un material absorbente de radiación UV convencional, como se muestra en lo que sigue.

La capacidad de los 1DPCs de SiO_2/ZrO_2 flexibles y tándems de estos para proteger de la luz UV se puso a prueba mediante la exposición de tiras comerciales sensibles a la radiación UV (Control Cure, UV FastCheck Strips, UV process supply Inc.), empleando diferentes tipos de películas de protección UV o combinaciones de estas, al haz de radiación colimado y uniforme que viene a partir de un simulador solar.

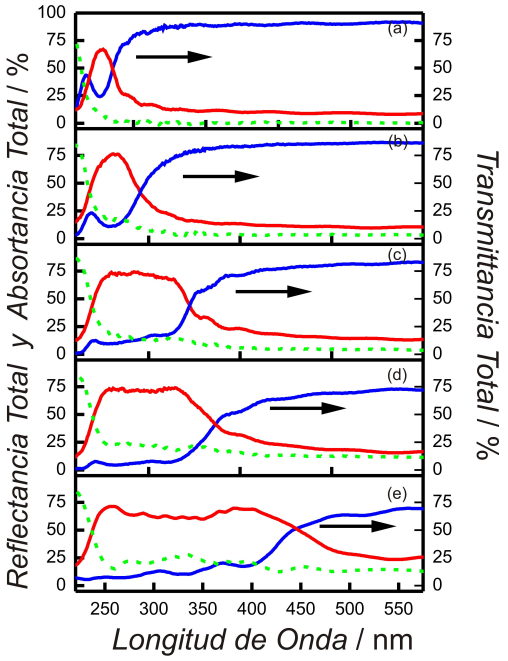

Figura 6: Espectros de reflectancia total (línea roja), transmitancia total (línea azul) y absortancia (línea de puntos verdes) de diferentes tándems de multicapas flexibles que contienen las películas que se muestran en la figura 6a. El número de muestras apiladas es: (a) 1, (b) 2, (c) 3, (d) 5, y (e) 7.

El análisis detallado de los cambios de color inducidos en las tiras por el efecto de la exposición a la luz UV nos permite cuantificar la cantidad de energía que han recibido del simulador solar. Estas tiras sensibles se iluminaron con 1 sol de intensidad de luz (AM1.5, 1000W/m^2) durante el mismo tiempo para cada opción protectora empleada. Las láminas ensayadas fueron: 1) Un tándem de multicapas que bloquea toda la región UV (muestra ML_A); 2) otro tándem de espejos de Bragg flexibles que imita el perfil de absorción del TiO_2 (muestra ML_B); 3) Una película de PDMS que contiene una capa de nanopartículas de TiO_2 con el mismo espesor que los cristales fotónicos utilizados (aproximadamente 1 µm); 4) Una película de PDMS sobre el que se depositó una fina capa de benzofenona-3, una molécula orgánica que se incluye como agente de protección UV en lociones de protección solar; 5) una película de PDMS, para cuantificar el efecto de recibir esta cantidad de radiación sin protección. En la Figura 7a se muestra la energía por unidad de área recibida por las tiras en cada caso. Los espectros de transmitancia correspondientes a las diferentes muestras se representan en la figura 7b. Cabe destacar que la capacidad de proteger por interferencia del tándem de los espejos flexibles ML_B para proteger contra los rayos UV es tan buena como la de una película que protege por la absorción de nanopartículas de TiO_2, mientras que el rendimiento de la muestra ML_A supera la de la película sobre la que se depositó la benzofenona-3. Esto demuestra que los materiales fotónicos flexibles son sustitutos adecuados de absorbentes inorgánicos u orgánicos de radiación UV, tradicionalmente empleados para polímeros dopados con el mismo fin.

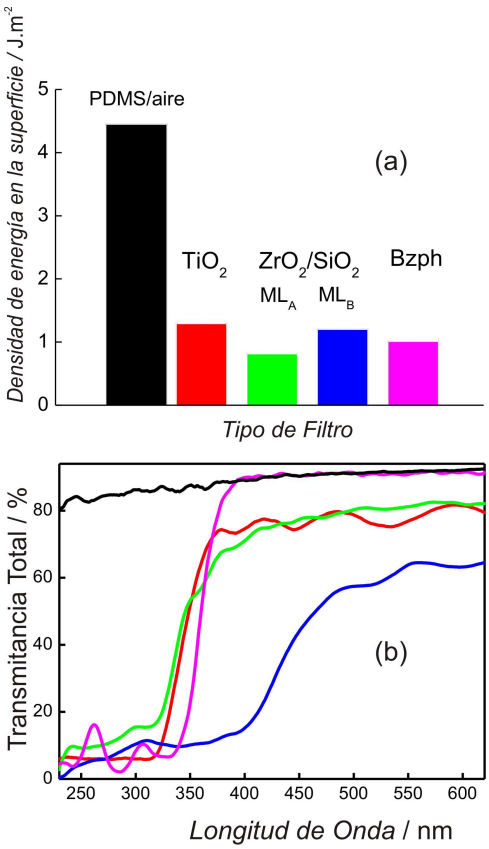

Figura 7: (a) Densidad de energía recibida por unidad de área en la superficie de las tiras sensibles UV cubiertas con diferentes películas flexibles protectoras contra la luz UV, expuestos a un simulador solar (espectro AM 1,5, 100 mW /cm^2). La altura de la barra representa el valor medio y la línea de negro representa la desviación estándar. Las muestras ML_A y ML_B están compuestas de diferentes combinaciones de cristales fotónicos flexibles SiO_2/ZrO_2. (b) los espectros de transmitancia total de los films protectores usados en la Figura 6a: PDMS puro (línea negra), película de nanopartículas de TiO_2 incrustadas en PDMS (línea roja), benzofenona-3 depositada en PDMS (línea violeta), ML_A (línea verde), y ML_B (línea azul).

Filtros UVB flexibles biocompatibles para la protección celular epitelial

La radiación UV solar es una de las principales causas de eritema, una enfermedad que se ha utilizado como un índice estandarizado para estimar el riesgo que esta produce para la piel humana. La genotoxicidad de la radiación UV se basa en el suministro de energía fotoquímica al genoma de la piel, suficiente para producir daño, específicamente en el ADN,[38] que conduce a anomalías genómicas, por ejemplo, las mutaciones[39] que son capaces de inducir cáncer de piel.[40]En un trabajo desarrollado por Ikehata,[41]se caracterizó la dependencia espectral de la

radiación incidente con los efectos genotóxicos en la piel mediante el análisis de la cinética de inducción de mutación e inflamación en la piel de ratones,.

En este trabajo, la cinética de dosis-respuesta de la inducción de mutaciones en la epidermis y la dermis de la piel del ratón se examinó en el intervalo de longitudes de onda que comprende el rango 260-364 nm por irradiación UV monocromática con alta intensidad, siendo lo más significativo el hecho de que la respuesta fue dependiente de la longitud de onda, que muestra un pico a alrededor de 310-320 nm. La dependencia de la longitud de onda se puede ver en la Figura 8. En este segmento se presentarán los resultados del objetivo propuesto de construir filtros transparentes, de alta calidad óptica, que protegen selectivamente la región UVB, siempre que sean capaces de adaptarse a diferentes tipos de superficies.

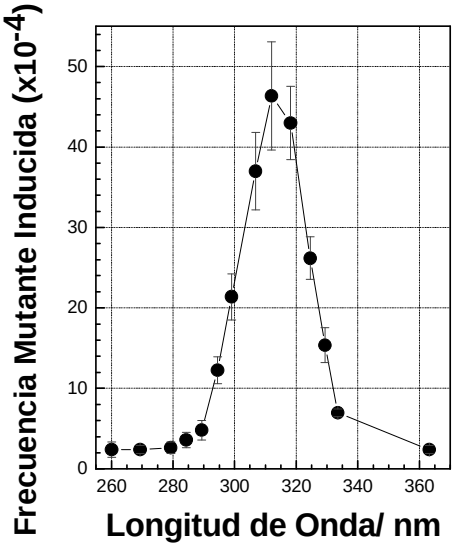

Figura 8: Dependencia de la longitud de onda de la genotoxicidad de la radiación UV en la piel para valores planos de frecuencia mutante.

En este capítulo, un análisis del grado de daño causado en el ADN de diferentes células epiteliales expuestas a una fuente de UV cuando están protegidas por los filtros flexibles, se realizó, con el propósito de demuestrar que estas películas son capaces de bloquear tan eficazmente como compuestos absorbentes de UV embebidos en matrices poliméricass similares. Esto significaría, por lo conocido hasta ahora, la primera evidencia experimental de la protección de las células epiteliales por una película flexible biocompatible, en la que no se produce absorción, juiciosamente diseñada para proteger específicamente contra una gama UV altamente genotóxica.

Para llevar a cabo el mencionado análisis, se prepararon 1DPCs flexibles diseñados específicamente para bloquear la regíon espectral de interés para prevenir el daño al ADN. Se desarrolló un filtro que consiste en el tándem de dos películas de 1DPCs SiO_2/ZrO_2 en la parte

superior de una película de 1dPC de SiO_2/TiO_2 (etiquetado como ZST-3), cuya caracterización óptica se muestra en la figura 9.

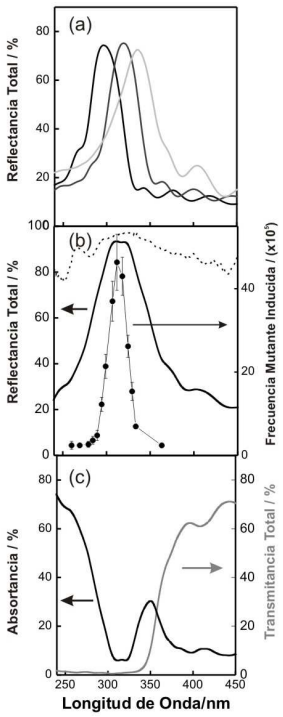

Figura 9: a) Espectros de reflectancia total de cada una de las tres películas que constituyen el filtro ZST-3. (b) Espectro de reflectancia total del filtro ZST-3 (eje Y izquierdo). El espectro de acción de la frecuencia mutante inducida también se representa (a la derecha del eje Y) (adaptado de la referencia 41). Superpuesta a ambos espectros, graficamos la irradiancia espectral de la lámpara en unidades arbitrarias (línea discontinua) (c) Espectros de absortancia total y transmitancia total del filtro ZST-3.

Se observa incluso que aún incluyendo nanopartículas TiO_2, que absorben la radiación UVB, los efectos de interferencia prevalecen sobre la absorción de luz en el UVB como mecanismo de bloqueo, presentando un pico de reflectancia de cerca del 95% de intensidad.En aras de la comparación, hemos preparado películas flexibles de PDMS que contienen exclusivamente nanopartículas de TiO_2, etiquetados como T-1, como se puede ver en la Figura 10.

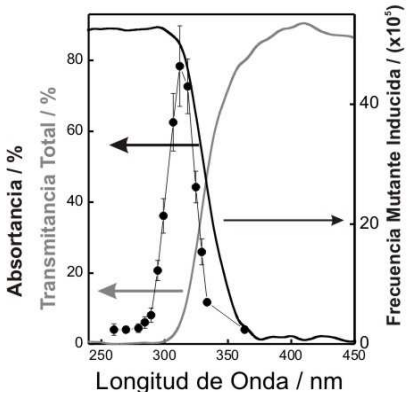

Figure 10: Espectros de absortancia (línea continua negra) y transmitancia total (línea sólida de color gris) del filtro T-1. La frecuencia mutante inducida también se traza (eje Y derecho) (adaptado de referencia 41).

En este film, el bloqueo de UVB sólo tiene lugar debido a la absorción. Esto se puede ver fácilmente a partir del análisis de la determinación experimental de la transmitancia total y reflectancia total, de donde calculamos la absortancia.

Daño en el ADN en diferentes tipos de células epiteliales cubiertas con filtros de protección UV

La capacidad para proteger contra los efectos genotóxicos de la radiación UV de estos filtros fue probada en el grupo de Guillermo de la Cueva en BIONAND, Málaga, mediante la exposición de una serie de cultivos de células de la piel humana a una fuente de luz UV. Más específicamente, se analizó el daño celular inducido por la radiación UV en la línea celular de melanoma SB2 humano a nivel molecular por la detección de dímeros de pirimidina ciclobutano (CPD, por sus siglas en inglés) en el ADN de la célula y en el nivel fenotípico mediante la cuantificación de la tasa de muerte celular después de la exposición a la radiación UV (mediante la medición de la llamada tasa de apoptosis). Los CPDs son las lesiones pre-mutagénicas más predominantes en el ADN producidas por la radiación UV en las células de la piel humana. Por lo tanto, se ha utilizado esta alteración para determinar el daño en el ADN en una primera etapa.

Un procedimiento bien establecido, tal como se describe por Schwarz et al.[42] y Huynh et al.[43], se utiliza para irradiar las células SB2. Las células se expusieron a 200 J/m^2 colocándolas a una distancia de 23 cm desde la fuente de radiación UV. Las células no irradiadas fueron manejadas de la misma manera, excepto por el hecho de que no se expusieron a la luz UV.

En la Figura 11, se muestran las imágenes de los núcleos de las células irradiadas. Se observó CPD con inmunotinción positiva (señal verde) en los núcleos (señal azul) de células irradiadas cuando se utilizaron sin filtro (Figura 11a) o sin el filtro de control (Figura 11b, etiquetado

como Ctrl). Una película hecha de PDMS sin presencia alguna de nanopartículas fue utilizada como filtro de control. Por otro lado, no se detectó señal CPD en células irradiadas protegidas por las películas altamente absorbente T-1, que contienen nanopartículas de TiO_2 (Figura 11c), que utilizamos como referencia, o por la película altamente reflectante ZST-3 que contiene multicapas de nanopartículas.

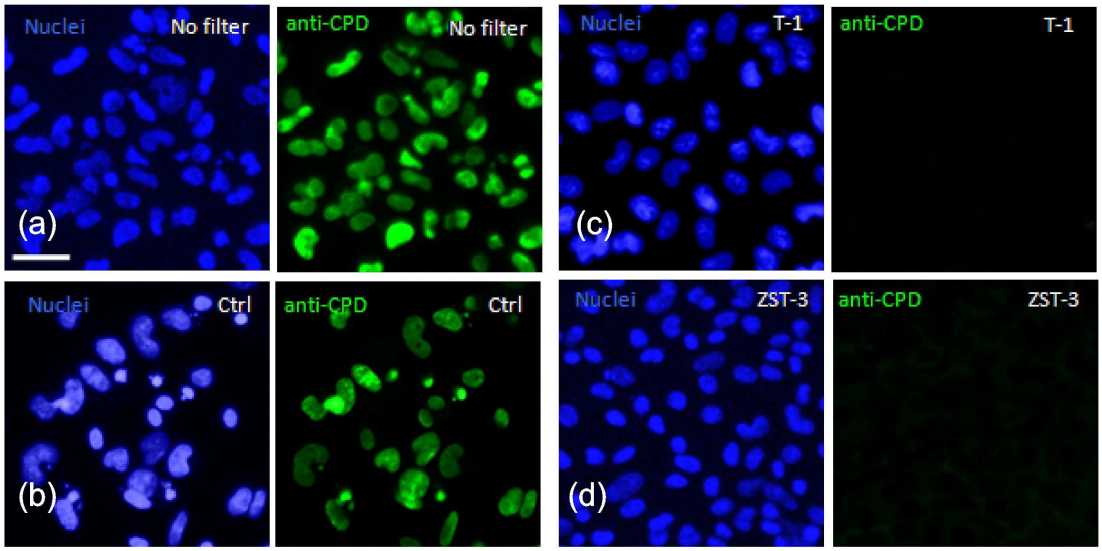

Figure 11: Daño inducido por la radiación UV en el ADN de la línea celular SB2. Se observó CPD con inmunotinción positiva (señal verde) en los núcleos (señal azul) en las células irradiadas cuando (a) no se utilizó ningún filtro ó (b) se utilizó el filtro de control (Ctrl). No se detectó ninguna señal de CPD en células irradiadas protegidas por (C) películas altamente absorbentes que contienen nanopartículas de TiO_2 (T-1) o (d) películas altamente reflectantes que contienen cristal fotónicos (ZST-3).

El análisis de CPD con inmunotinción demostró que el mecanismo de reflexión UV de las filtros flexibles impidió eficazmente la aparición de estas lesiones en el ADN. Cuando aparecen estas lesiones, las células detienen la proliferación y activan el mecanismo de reparación. Si tienen éxito, el ciclo celular se restaurará y la proliferación se reanuda. Por el contrario, si no lo logran, la muerte celular programada se activará.

Efecto de la modulación espacial de efectos fotoquímicos inducidos por la radiación UV en la formación de multicapas periódicas mediante el proceso de choque osmótico colectivo en las películas de copolímeros de bloque

Muy recientemente, se demostró que una estructura estratificada porosa se puede lograr a partir de una película de copolímero de bloque (BCP).[44]En particular, se demostró que una película

que contiene poliestireno (PS) y polimetil-metacrilato (PMMA), en su fórmula reducida PS-b-PMMA, se puede utilizar como material de partida para alcanzar multicapas porosas ordenadas a través de un proceso que implica el choque osmótico colectivo (COS por sus siglas en inglés). La estructura final muestra capas densas y porosas alternadas que se comportan como un cristal fotónico unidimensional con picos de Bragg en el rango UV. En este capítulo, presento evidencia óptica y estructural que demuestran que la estructura periódica resultante es una consecuencia directa de la formación de una onda electromagnética estacionaria generada por interferencia de película delgada durante la etapa de irradiación UV. Esta onda estacionaria impone un patrón periódico de la degradación de PMMA y y en el entrecruzamiento del PS, por lo tanto, la determinación de la periodicidad de la estructura porosa que surge después del tratamiento con ácido acético, independientemente del período y el número de redes de planos esféricos en la película de partida.

Con el fin de analizar más a fondo el mecanismo de formación de capas porosas y densas alternos en películas BCP, hemos preparado una serie de películas de PS-b-PMMA de diferente peso molecular total (Mw = MwPMMA + M_WPS) sobre obleas de silicio con 2.5x2.5 cm_2 por spin-coating, pero con aproximadamente la misma relación Φ = MwPMMA /M_WPS (0,13 <Φ <0,17). Las películas se tratan posteriormente térmicamente para estabilizar una red tridimensional de esferas de PMMA no conectados en una matriz de PS. Las láminas de PS-b-PMMA se prepararon utilizando los siguientes pesos moleculares: 71, 81, 126, 135, 295 y 1.000 kDa.

Una explicación para estos efectos se puede encontrar en la distribución espacial del campo de la radiación UV que tiene lugar dentro de la película durante el procesamiento. Todas las muestras empleadas para este estudio tienen el mismo espesor exacto (420 ± 10 nm), según lo confirmado por el análisis de las franjas de interferencia observados en sus espectros de reflectancia total, que se muestra en la Figura 12a. Así, se espera un patrón espacial similar de intensidad de campo de luz UV en todos ellos tras la irradiación. La figura 12b muestra la distribución espacial del campo eléctrico, $|E|^2$, para la luz de longitud de onda λ = 254 nm que incide normalmente sobre la película depositada previamente en un substrato de silicio.

El perfil espacial de $|E|^2$ es una consecuencia de la formación de una onda estacionaria en la película PS-b-PMMA como resultado de la interferencia entre los haces de transmisión y los reflejados parcialmente en las interfases aire-polímero y polímero-silicio. Esto da lugar a regiones de alta y de baja intensidad UV de la iluminación, distribuidos periódicamente a lo largo de la sección transversal de la película. Este patrón se traduce en una degradación desigual de PMMA y consolidación del PS a lo largo de la mayor parte de la película, que a su vez debería modular espacialmente el proceso de choque osmótico colectivo.

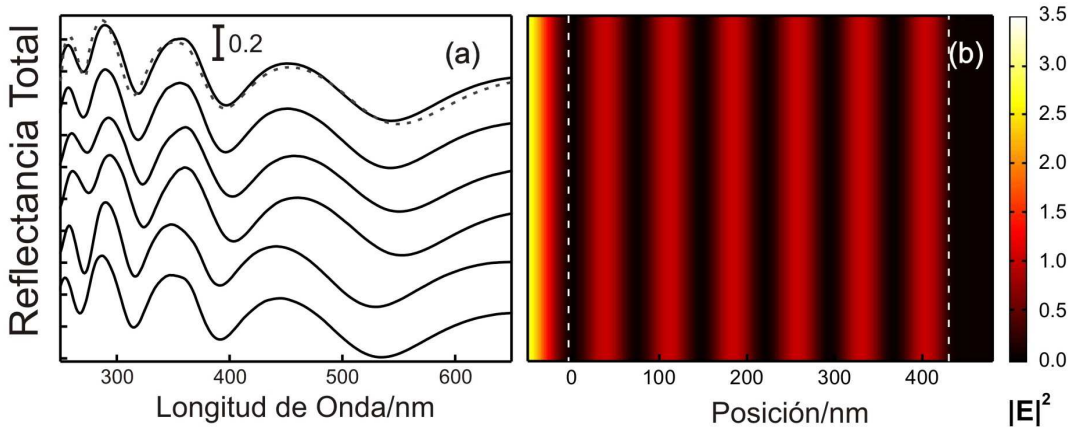

Figure 12: (a) Los espectros de reflectancia total para las muestras preparadas con PS-b-PMMA con pesos moleculares de 71, 81, 126, 135, 296 y 1.000 kDa respectivamente (espectros de arriba hacia abajo, líneas negras). El espectro teórico calculado para una película de PS-b-PMMA se incluye (gris línea discontinua). (b) Distribución espacial a lo largo de la sección transversal (eje Y) del cuadrado del campo UV (λ = 254 nm) representado para una película de PS-PMMA con un espesor de 420 nm depositada sobre un sustrato de silicio. Las líneas punteadas blancas representan las interfaces de película. Posición a 0 nm representa la interfaz entre el aire y la película PS-PMMA.

Así que, como $|E|^2$ describe un período completo en aproximadamente 75 nm, cada una que comprende un par de franjas de baja y alta intensidad, y el espesor de la película es de 420 nm, alrededor de once capas (cinco períodos y medio) de diferente microestructura se esperan en principio como resultado de dicha modulación. Los cambios inducidos por efectos fotoquímicos provocados por la luz UV deben ser mínimos en aquellas regiones en las que el perfil $|E|^2$ presente mínimos, desarrollándose fundamentalmente en torno a su máximo.

Todas estas muestras se expusieron a la dosis ($8J/cm^2$) de luz UV (λ = 254 nm) necesaria para alcanzar una multicapa porosa periódica. El efecto de este tratamiento es se basa en el entrecruzamiento del PS y en la degradación del PMMA a oligómeros de bajo peso molecular. Finalmente, las películas se sumergieron en ácido acético, un disolvente de PMMA que al mismo tiempo es capaz de difundir a través de PS entrecruzado sin disolverlo. Como el ácido acético alcanza al PMMA a través de la matriz de PS, que actúa como una barrera semi-permeable para la transferencia de disolvente, la presión osmótica se acumula debido a la hinchazón de los dominios esféricos, que se deforman anisotrópicamente. El adelgazamiento de las paredes de PS entre las esferas eventualmente conduce a su rotura y la formación de capas con poros grandes soportados por columnas de PS, separados de capas perforadas de densidades más altas.

Como se puede ver en la Figura 13a, las estructuras finales alcanzadas de PS-b-PMMA de peso molecular 71, 82, 126 y 135 kDa presentan picos de reflectancia intensos(hasta 80%) en la región UV que pueden ser inequívocamente atribuibles a los efectos de difracción de Bragg

derivadas de una relativamente fuerte modulación periódica del índice de refracción (n_L = 1,23 y n_H = 1,52, para cada par de capas consecutivas) a lo largo de una dimensión espacial que tiene lugar en distancias del orden de unos cientos de nanómetros.

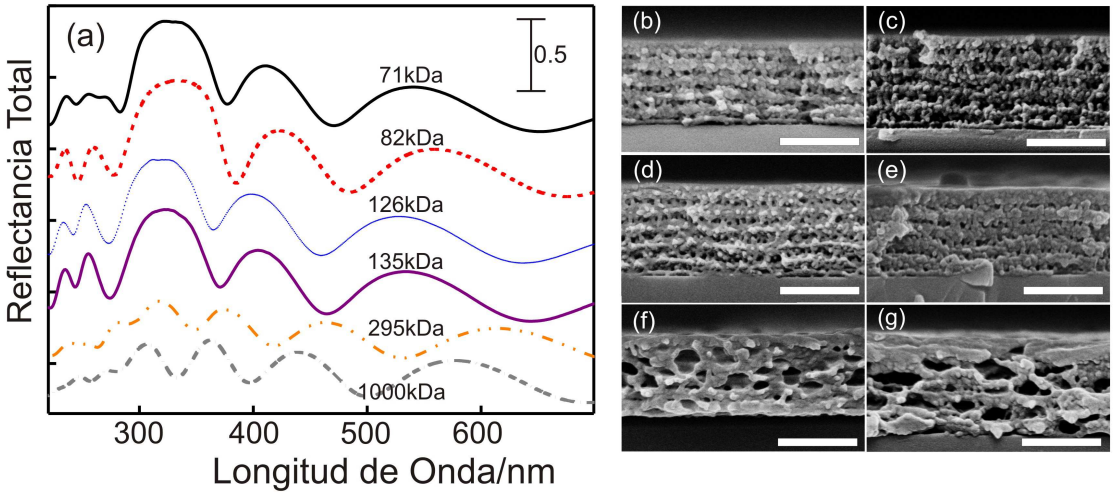

Figura 13: (a) Espectros de reflectancia total obtenidos para películas de PS-PMMA de diferente peso molecular después de la irradiación y el tratamiento con ácido acético. El peso molecular se indica junto a su correspondiente espectro. Imágenes de sección transversal, de (b) a (g), obtenidas a partir de películas PS-PMMA después de la irradiación UV y tratamiento con ácido acético. La barra de escala es de 500 nm en todas las imágenes. El peso molecular se indica en cada imagen FESEM.

La sección transversal de estas estructuras muestra una alternancia periódica de capas de alta y baja porosidad, como se puede ver en las imágenes FESEM que se muestran en las Figuras 13b-13e. Curiosamente, estas cuatro muestras presentan picos de reflectancia en la misma posición espectral ($\lambda \sim 320$ nm), independientemente del tamaño de la esfera de PMMA alcanzado en la fase segregada, en buen acuerdo con la observación de un valor idéntico de la periodicidad en las imágenes FESEM.

Otra prueba de la replicación de la distribución de intensidad de campo se alcanza al variar dinámicamente el ángulo de incidencia de la luz UV. Como se explicará en detalles, el desorden es inducido en parte de la película como resultado de la propagación de las franjas de alta intensidad de campo debido a la rotación continúa de la película. Como la formación de un patrón regular de franjas de alta y baja intensidad de luz dentro de la película depende del ángulo de iluminación, decidimos exponer nuestras películas a una dosis total similar de la luz UV pero utilizando como soporte una placa giratoria que describe un arco de 60° con una velocidad angular de $2/3\pi$ rad/s. Para una longitud de onda dada, la posición espacial de las regiones de alta intensidad de la luz varía, como se muestra en el perfiles trazados $|E|^2$ dependientes del ángulo en la figura 14a, particularmente en la región más cerca de la interfaz BCP-aire. Este cambio angular da lugar a una atenuación en la modulación de los efectos fotoquímicos, conduciendo eventualmente a la ausencia de un patrón periódico de los poros,

como se puede confirmar tanto la imagen FESEM de su sección transversal, en la figura 14b, y los espectros de reflectancia óptica, en la Figura 14c. Por favor, observe que el perfil $|E|^2$ es menos sensible al ángulo de incidencia en la parte inferior de la película, cerca de la interfaz de BCP-silicio, en donde se conserva la estructura alternada porosa-densa de las capas.

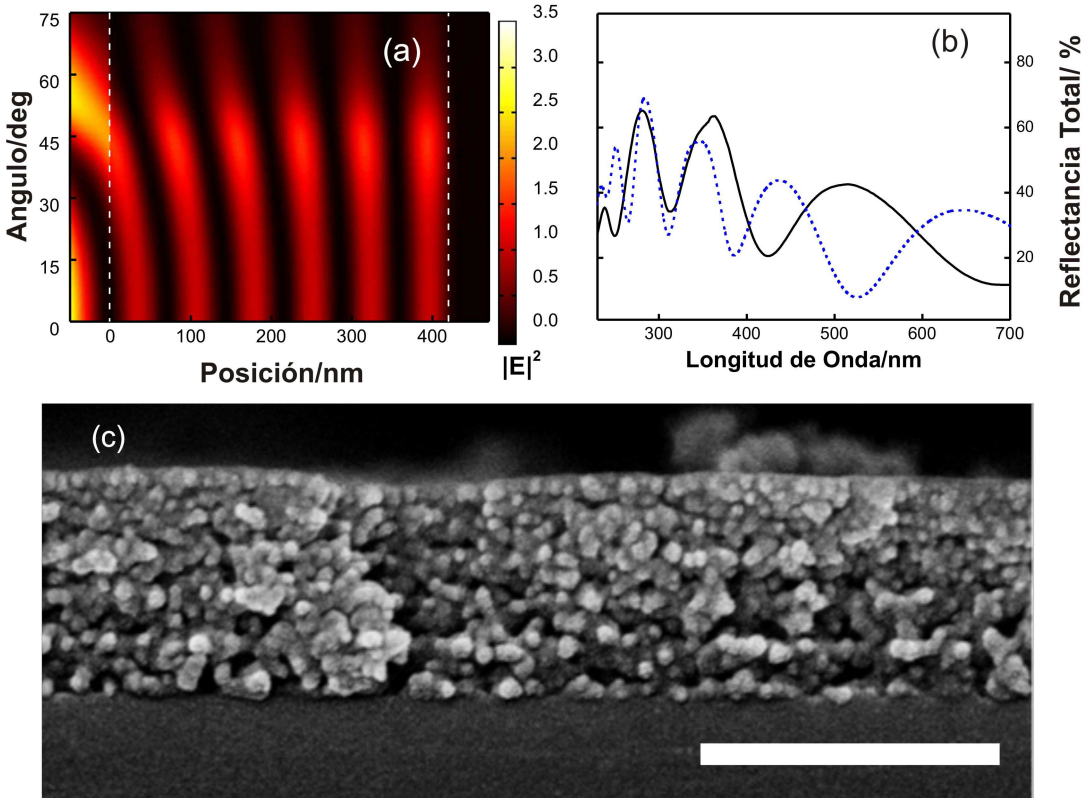

Figura 14: (a) Distribución espacial a lo largo de la sección transversal (eje X) del campo eléctrico al cuadrado $E|^2$ de la luz UV calculada para una película de PS-PMMA con un espesor de 420 nm depositada sobre el sustrato de silicio como función del ángulo de incidencia (eje Y). Las líneas blanco punteadas representan las interfaces de la película. Las líneas discontinuas verticales indican las interfaces entre el aire y PS-PMMA (x = 0 nm) y PMMA-silicio (x = 420 nm). (b) Los espectros de reflectancia total obtenidos para una película de PS-PMMA con peso molecular 82,5 kDa, antes (línea azul discontinua corta) y después de la irradiación con luz UV (λ = 254 nm) en dirección variable de incidencia 0 º < θ < 60 º y el tratamiento con ácido acético ácido (línea continua negra). (c) Imagen FESEM de la sección transversal de la película bajo la incidencia de UV con variación dinámica de ángulo. La barra de escala es de 500 nm.

Conclusiones

En primer lugar, nanopartículas de TiO_2, ZrO_2, Nb_2O_5 se sintetizaron con éxito con el objetivo de utilizarlas como bloques constituyentes para cristales fotónicos unidimensionales. Las nanopartículas presentan tamaños de unos pocos nanométros, condición necesaria para obtener una alta calidad óptica y para evitar luz difusa en las estructuras fotónicas, además de que no presentan absorción en diferentes rangos del UV.

Multicapas rígidas y flexibles fueron diseñadas para ser capaces de proteger eficazmente contra la radiación UV a través del fenómeno de reflexión óptica en rangos de longitud de onda seleccionados. Se demostró que estas películas presentan un nivel de protección contra la radiación UV igual o superior a capas de espesor similar hechas de materiales puramente absorbentes en términos del nivel de protección contra la radiación UV logrado.

Se hicieron filtros flexibles para proteger específicamente la región UVB. Se demostró, en un sistema real que comprende células epiteliales humanas sensibles al rango mencionado, que estas películas son capaces de bloquear tan eficazmente como compuestos absorbentes de UV embebidos en matrices poliméricass similares.

Se mostró evidencia experimental y teórica de la función clave que los patrones de intensidad de campo de luz UV desempeñan en la formación de estructuras periódicas de capas porosas y densas alternadas, formando un sistema con propiedades de cristal fotónico. Se confirmó que la periodicidad observada surge como resultado de la combinación de la modulación espacial inducida por efectos fotoquímicos y el proceso de choque osmótico.

Referencias

[1]. Ren, Q.; Gailitis, R.P.; Thompson, K.P.; Lin, J.T.; *Journal of Quantum Electronics*, **1990**, *26*, 2284-2288.

[2]. Serpone, N.; Dondi, D.; Albini, A. Inorganica Chimica Acta 360 (2007) 794–802.

[3]. Bintsis, T.; Litopoulou-Tzanetaki, E.; Robinson, R.K.; *J. Sci. Food. Agric*.. **2000**, 22, 5142.

[4]. Lopez Cisneros ,R.; Gutarra Espinoza, A.; Litter, M.I; *Chemosphere* 48 (2002) 393–399.

[5] Andrady, A.L.; Harnid, S.H.; Hu, X.; Torikai, A. *Journal of Photochemistry and Photobiology B: Biology*, **1998**, 46, 96103.

[6] B. Neppolian, H.C.; Choi, S.; Arabindoo, S.B; Murugesan, V. *Journal of Hazardous Materials B*, **2002**, 89, 303–317.

[7]. Nowick, M.; Richter, A.; Wolf, B.; Kaczmarek, H. *Polymer* **2003**, *44* 6599–6606.

[8]. Rui Yang, P.A.; Christensen, T.A.; Egerton, J.R.; White. *Polymer Degradation and Stability* **2010**, 95.

[9]. Ting, W.W. *International Journal of Dermatology* **2003**, *42*, 505-513.

[10]. Brash, D. *Trends in genetics* **1997**, *13*, 410-414.

[11] McCarty, C.A.; Taylor, H.R. *Progress in Lens and Cataract Research.Dev Ophthalmol.*, **2002**, vol 35, 21-31.

[12] Chalam, K.V., Vijay, K.; Raluca, R.; Sankarathi, B. *Eye and Contact Lens: Science and Clinical Practice*, **2011**, 37, 4, 225-232.

[13]. Demir, M.M.; Koynov, K.; Akbey, U.; Bubeck, C.; Park, I. Lieberwirth, I.; Wegner G. *Macromolecules.* **2007,** *40*, 1089-1100.

[14].Liou, G.S.; Lin, P.H.; Yen, H.J.; Yu, Y.Y.; Tsai, T.W.; Chen, W.C. *J. Mater. Chem.* **2010**, *20*, 531-536.

[15]. Tu, Y.; Zhou, L.; Jin, Y.Z.; Gao, C.; Ye, Z.Z.; Yang, Y.F.; Wang, Q.L. *J. Mater. Chem.* **2010**, *20*, 1594-1599.

[16]. Mazzocchetti, L.; Cortecchia, E.; Scandola M.; *ACS Appl Mater Interfaces* **2009**, *1*, 726-734.

[17]. Koziej, D.; Fischer, F.; Kränzlin, N.; Caseri, W.R.; Niederberger, M. *ACS Appl. Mater. Interfaces* **2009**, *1*, 1097-1104.

[18]. Druffel, T.; Mandzy, N.; Sunkara, M.; Grulke, E. *Small* **2008**, *4*, 459-461.

[19]. Keck, J.; Roessler, M.; Scroeder, C.; Stueber, G.J.; Waiblinger, F.; Stein, M.; Legourrierec, D.; Kramer, H.E.A.; Hoier, H.; Henkel, S.; Fischer, P.; Port, H.; Hirsxh, T.; Rytz, G. Hayoz, P. *J. Phys. Chem. B* **1998**, *102*, 6975-6985.

[20]. Mahltig,B.; Bottcher,H.; Rauch, K.; Dieckmann, U.; Nitsche, R.; Fritz, T. *Thin Solid Films* **2005**, *485*, 108 –114.

[21]. Zayat, M.; Garcia-Parejo, P.; Levy, D. *Chem. Soc. Rev.* **2007**, *36*, 1270–1281.

[22]. DeCorby,R.G.; Ponnampalam,N.; Nguyen,H.T.; Clement,T.J. *Adv. Mater.* **2007**, *19*, 193–196.

[23]. Macleod, A. in *Thin film optical filters*, Institute of Physics Publishing, London, 3rd ed., **2001**.

[24]. Colodrero,S.; Ocaña, M.;Míguez,H. *Langmuir*, **2008**, *24*, 4430-4435.

[25]. Calvo, M.E.; Colodrero,S.; Hidalgo,N.; Lozano, G.; López López, C.; Sánchez-Sobrado, O.; Míguez, H. *Energy & Envirom. Sci*. **2011**, *4*, 4800-4812.

[26]. Bonifacio, L. D.; Lotsch, B. V.; Puzzo, D.P.; Scotognella, F.; Ozin, G.A. *Adv. Mater.*, **2009**, *21*, 1641.

[27]. Colodrero, S.; Mihi, A.; Häggman, L.; Ocaña, M.; Boschloo, G.; Hagfeldt, A.; Míguez, H. *Adv. Mater.*, **2009**, *21*, 764-770.

[28]. Bonifacio, L.D.; Puzzo, D.P.; Breslav, S.; Willey, B.M.; McGeer, A.; Ozin, G.A. *Adv. Mater.*, **2010**, *22*, 1351-1354.

[29]. Zavala-Rivera, P.; Channon, K.; Nguyen, V.; Sivaniah, E.; Kabra, D.; Friend, R.H.; Nataraj, S.K.; Al-Muhtaseb, S.A.; Hexemer, A.; Calvo, M.E.; Miguez, H. *Nat. Mater*, **2012**, *11*, 53-57.

[30] Lu, Y.; Ganguli, R.; Drewien, C.A.; Anderson, M.T.; Brinker, C.J.; Gong, W.; Guo, Y.; Soyez, H.; Dunn, B.; Huang, M.H.; Zink, J.I. *Nature*, **1997**, 389, 364-368.

[31] Chang, Y.S.; Chang, Y.H.; Chen, I.G.; Chen, G.J; Chai, Y.L. *Journal of Crystal Growth*, **2002**,243 319–326.

[32] Lu, Y.; Yin, Y.; Mayers, B.T.; Xia, Y. *Nano Lett.*, **2002**, Vol. 2, No. 3.

[33] Burnside, S.D.; Shklover, V.; Barbe, C.; Comte, P.; Arendse, F.; Brooks, K.; Gratzel M., *Chem. Mater.*, **1998**, 10, 2419.

[34] Guo, Y.; PhD Thesis, "Nanocrystalline sol-gel Nb2O5 coatings Preparation, characterisation and application to photovoltaic cell, lithium battery and electrochromic device", 2002, Saarbrucken.

[35] Xu, Q.; Anderson, M.A. *J. Mater. Res.*, **1991**, *6*, 1073.

[36] Colodrero, S.; Ocana, M.; Míguez, H. *Langmuir*, **2008**, 24, 4430-4434.

[37] Lozano, G.; Colodrero, S.; Caulier, O.; Calvo, M.E.; Míguez, H. *J. Phys. Chem. C*, **2010** , *114* , 3681 .

[38] Pfeifer, G.P. *Photochemistry and Photobiology*, **1997**, Vol: 65(2):270-283.

[39] Ikehata, H.; ONO, T. *Journal of Radiation Research*, **2011**, Vol: 52(2):115-25.

[40] Wikonkal, N.M.; Brash, D.E. *Journal of Investigative Dermatology Symposium Proceedings*, **1999**, Vol: 4(1):6-10.

[41] Ikehata, H.; Higashi, S.; Nakamura, S.; Daigaku, Y.; Furusawa, Y.; Kamei, Y.; Watanabe, M.; Yamamoto, K.; Hieda, K.; Munakata, N.; Ono, T. *J Invest Dermatol.*, **2013,** Jul;133(7):1850-6.

[42] Schwarz, T.A.; Gschnait, V.F.; Lugar, T.A. *J. Invest. Dermatol* **1986,** *87,* 289.

[43] Huynh, T.T.; Chan, K.S.; Piva, T.J. *Photodermatol. Photoimmunol. Photomed.* **2009**, 25, 20–2.

[44] Zavala-Rivera, P.; Channon, K.; Nguyen, V.; Sivaniah, E.; Kabra, D.; Friend, R.H.; Nataraj, S.K.; Al-Muhtaseb, S.A; Hexemer, A.; Calvo, M.E.; Miguez, H., *Nat. Mater,* **2012**, *11*, 53-57.